Computer Methods in Applied Mechanics and Engineering 457 (2026) 118613

Contents lists available at ScienceDirect

Computer Methods in Applied Mechanics and Engineering

journal homepage: www.elsevier.com/locate/cma

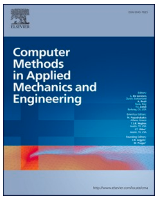

An effective overlapping finite element for three-dimensional incompressible linear elasticity

Williams L. Nicomedes [*,a], Klaus-Jürgen Bathe [b]

[a] Department of Engineering and Computing, Minas Gerais Federal Institute of Education, Science and Technology, Bambui, MG 38900-000, Brazil
[b] Department of Mechanical Engineering, Massachusetts Institute of Technology, Cambridge, MA 02139, United States

HIGHLIGHTS

- The analysis of three-dimensional incompressible media is considered.
- Overlapping finite elements are formulated, analyzed and applied.
- The proposed element for three-dimensional solutions is very effective.
- The inf-sup test is passed, the element provides stable solutions.
- The accuracy of solutions is maintained as the meshes become distorted.

ARTICLE INFO

Keywords:
Elasticity
Finite element method
Incompressibility
Inf-sup condition
Mixed formulations
Overlapping finite elements

ABSTRACT

In this paper, we continue our exploration of overlapping finite elements for the analyses of incompressible media. We examined earlier the solutions of the two-dimensional Navier-Stokes equation discretized by overlapping elements on quadrilateral cells [36]. Building on the results of that paper, we now move to three-dimensional analyses and direct our attention to linear elasticity problems discretized by overlapping elements on tetrahedral cells. These elements are again shown to be stable (i.e., they satisfy the inf-sup condition), which rules out the possibility of spurious pressure solutions. But what really contributes to the effectiveness of the overlapping elements is that they require less degrees of freedom (DoF's), leading to smaller matrices with tighter bandwidths and less total solution times than other classical finite elements routinely used in analyses of incompressible media. As we show in the paper, the proposed overlapping element is in particular more effective than the widely used Taylor-Hood element. This increase in effectiveness is important because in three-dimensional analyses the number of DoF's and solution times required to obtain accurate results are usually very high.

1. Introduction

1.1. The OFE program

The finite element method has been successfully applied for many years to obtain solutions of solid mechanics problems (linear and nonlinear). While many excellent developments have taken place [1,2,6,21] we focus in this introduction on those works that gravitate around and were crucial to the invention of the specific methodology which is the topic of this paper, namely, the overlapping finite

---

[*] Corresponding author.
E-mail addresses: williams.nicomedes@ifmg.edu.br (W.L. Nicomedes), kjb@mit.edu (K.-J. Bathe).

https://doi.org/10.1016/j.cma.2025.118613
Received 5 September 2025; Received in revised form 2 November 2025; Accepted 25 November 2025

elements (acronym is "OFE").

Recently, several other novel formulations have been proposed, largely considering the solution of two-dimensional problems, see for example [38,39], and [27], but in this paper we build on our previously published results [36] and focus on the solution of three-dimensional problems. To establish an effective procedure for such solutions generally represents a significantly larger challenge.

The impetus for the creation of the OFE method came from the realization that, despite the ability of meshfree methods, in particular the method of finite spheres (MFS), to provide accurate solutions [4,13-15,17,25,34,35], the cost of these solutions is usually too high, which precludes altogether their application to the analyses of problems arising in engineering practice. The culprit behind the high cost of many meshfree methods that are reliable such as the MFS is the non-polynomial nature of their basis functions, which leads to a very expensive process of numerical integration, especially in three dimensions [6,29,33].

After the initial guidelines presented in [4], the groundwork for the OFE method was laid down in [7]. The idea of the "OFE program" was to develop a finite element with a high degree of insensitivity to mesh distortions, i.e., the method should be able to perform well irrespective of the quality of the underlying mesh. Up to this point, there was a dichotomy: traditional finite elements use polynomial basis functions – thus leading to a straightforward numerical integration – but require meshes that must satisfy certain geometrical constraints (of a "high quality mesh") [1], usually difficult to achieve by automatic mesh generation algorithms, particularly in three dimensions and in regions of the computational domain described by complicated geometries. Meshfree methods, on the other hand, do not require a mesh, but generally rely on non-polynomial basis functions, which leads to an expensive process of numerical integration.

So the "perfect" OFE method should in principle be able to solve the aforementioned dichotomy, by combining the most desirable features of meshfree methods and traditional finite elements: the new method must use polynomial basis functions (leading to a reasonably simple process of numerical integration), and must keep its performance irrespective of the mesh quality (i.e., it must be able to perform well in distorted, or "low quality" meshes).

However, the aforementioned paper [7] was still too focused on the "meshfree" aspect of the program, since it relied on the non-polynomial basis functions of the MFS method (defined as the product between Shepard functions and the local enrichment functions, the latter usually given by monomials). Progress there was made in developing a way to divide the computational domain Ω into two parts: a large one, corresponding to the central portions of Ω, to be discretized using standard finite elements on a uniform mesh (which are less expensive), and the remaining portions of Ω, close to the boundary $\partial\Omega$ (and possibly having a complicated geometry), to be discretized using the MFS basis functions – which do not require a mesh but on the other hand are more expensive. In this way, the overall cost of the procedure is expected to decrease (in comparison with a procedure entirely based on the MFS method). A special artifice for coupling the finite element and MFS solutions was successfully incorporated into the method.

The next paper in the development of the OFE program is [40]. The novelty is that instead of using the "pure" MFS basis functions as in [7], the regions of the domain close to the boundary $\partial\Omega$ are discretized into triangular cells. The nodes in these regions are still assigned the same MFS basis functions, but they are now "modulated" by first-order Lagrange basis functions when approximating the fields within the triangular cells. The hybrid character of the procedure becomes evident: both the meshfree aspect (Shepard/MFS basis functions) and the mesh-based aspect (Lagrange elements) are at play here. This new way of approximating functions within the cells received a name: whereas the field in the central regions of Ω is approximated by traditional elements defined on uniform meshes of quadrilateral cells, the field in the regions close to $\partial\Omega$ is said to be approximated by "overlapping elements" defined on (possibly distorted) triangular cells. Surprisingly, it was discovered that the procedure keeps its good performance even when the cells close to the boundaries have a "bad" or distorted shape.

In [41], we see a radical change: when approximating the field within a given cell e close to $\partial\Omega$, instead of using Shepard functions (to build the MFS basis functions) as in [40], they are replaced by their interpolation in terms of the second-order Lagrange basis functions defined within cell e. The overall basis functions used in the approximation of the field are now entirely polynomial, which leads to an efficient process of numerical integration (i.e., few points are required).

The methodology from [41] was extended to the solution of time-domain wave problems in [26]. In this paper, the "overlapping elements" are used throughout the domain Ω, i.e., the field within the cells located in the central portions of Ω and within those located near the boundary $\partial\Omega$ are approximated in the same way, with the OFE basis functions. The central idea is to include trigonometric functions in the local enrichment spaces associated with the nodes. The results are positive: the method shows good dispersion properties, and more importantly, keeps its precision when very distorted meshes are used.

Considering all the developments for the OFE method and proposing the AMORE (acronym for automatic meshing with overlapping and regular elements) procedure in [5], the work [18] successfully extends the OFE methodology to quadrilateral elements, i.e., the interior of the domain Ω is discretized by regular quadrilateral cells, whereas the portions near the boundary $\partial\Omega$ are discretized by (possibly very irregular) quadrilateral cells. Within a given cell e close to $\partial\Omega$, the Shepard functions (used in the construction of the MFS basis functions) are replaced by their interpolations in terms of the quadrilateral 8-node (or serendipity) functions defined there.

The approach used in [26] to solve time-domain wave propagation problems (which uses trigonometric functions in the local enrichment spaces associated with the nodes) was extended to inhomogeneous media (i.e., media with different material properties) in [9]. The major difficulty lies in imposing the interface conditions, characterized by a discontinuity in the gradient of the pressure field [35]. This problem is solved with Lagrange multipliers defined along the interface separating the media with different properties. The results are promising, and the procedure once more works well when distorted meshes are used.

An offshoot of the OFE program is the concept of *overlapping meshes* [19]. The idea is to employ different meshes at different portions of the domain Ω, i.e., Ω is subdivided into the subdomains $\Omega_1, \cdots, \Omega_n$, and different meshes are set up on the different Ω_i's, for $i = 1, \cdots, n$. The strength of the procedure lies in the fact that the domain Ω need not be partitioned into non-overlapping portions, i.e., the Ω_i's need not be pairwise disjoint (the Ω_i's can freely overlap with each other). The degree of sophistication employed here is high, and despite the apparent difficulty, the procedure is mathematically sound [20].

The papers [30-32] mark a significant evolution in the development of the overlapping finite elements: instead of using the interpolation of Shepard functions, they use the interpolation of certain mesh-dependent functions, constructed from first-order Lagrange basis functions. In this way, all functions involved in the problem (with the exception of those included in the local enrichment spaces) are mesh-dependent, and hence, polynomial. The numerical integration is improved even more, leading to very few points required by the process, thus paving the way for an efficient application of the method to three-dimensional problems. The results are very satisfactory, and show the insensitivity of the procedure to mesh distortions. From this point on, the OFE program does not make any reference to Shepard functions anymore.

1.2. Incompressible media

All applications within the OFE program referenced thus far are concerned with the analysis of compressible media. The extension of these ideas to incompressible media in fluid dynamics is presented in [36]. This preliminary work concentrated on two-dimensional problems, and uses the quadrilateral elements developed in [30] in the discretization of the weak forms arising in the mixed formulation of the Navier-Stokes equations. The focus was on establishing which pairs of overlapping finite element spaces – one space for approximating the velocity field and the other for approximating the pressure – satisfy the Babuska-Brezzi, or inf-sup condition [1, 2]. The results are once more surprisingly good, with the procedure keeping its predictive accuracy when distorted meshes are employed.

In this paper, we return to linear elasticity, but now we are in three dimensions, and the media are again assumed to be incompressible. The goal is to show that the tetrahedral overlapping elements originally introduced in [30] can be used to approximate the displacement and the pressure fields – albeit not in the same way – in order to build a discretization that is stable and free of spurious solutions. The stability of the pairs is examined with the same inf-sup test employed in [36].

In the course of the work, we uncovered a very formidable property of the overlapping elements in three dimensions: their ability to provide accurate results while at the same time requiring much less computational resources than the traditional finite elements. We show that the overlapping elements require just a fraction of the number of degrees of freedom (or DoF's) required by the traditional elements, which leads to smaller systems of linear algebraic equations to be solved. Moreover, when the overlapping elements are used, the (sparse) matrices in these systems have a smaller bandwidth (i.e., the nonzero elements are more tightly packed around the main diagonal), again in comparison with other traditional elements. This feature is linked to a smaller number of operations necessary to solve the corresponding linear system [1,2]. Our overlapping elements are thus shown to have good scalability properties, since they require less storage and less processing capability. This is a positive trait, as three-dimensional analyses grow large in required computational resources.

All these results are carefully demonstrated in the sections to follow. In Section 2, we provide a brief overview about the mathematical model of linear elasticity we are going to use, together with the corresponding weak formulation. Section 3 is dedicated to the

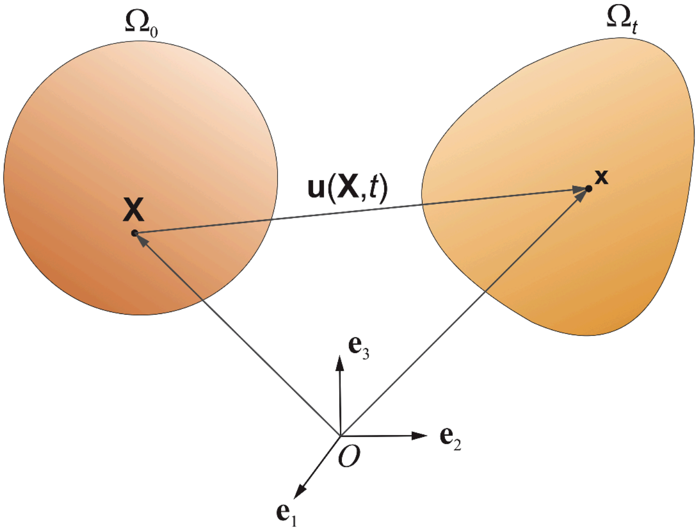

Fig. 1. The geometry of deformation. A body originally occupying the region Ω_0 at time $t = 0$ deforms (under the action of forces and tractions) into the body occupying the region Ω_t at some later time t. Each material point (particle) $\mathbf{X} \in \Omega_0$ is mapped to the spatial point $\mathbf{x} \in \Omega_t$. The relation between $\mathbf{X}$ and $\mathbf{x}$ is given by $\mathbf{x} = \mathbf{X} + \mathbf{u}(\mathbf{X}, t)$, where $\mathbf{u}(\mathbf{X}, t)$ is the displacement vector associated with the material particle $\mathbf{X}$ at time t. The points $\mathbf{X}$ and $\mathbf{x}$ are given with reference to a Cartesian coordinate system (where $\mathbf{e}_1$, $\mathbf{e}_2$, and $\mathbf{e}_3$ are unit vectors along the coordinate directions).

presentation of the overlapping finite element spaces to be used in the discretization of the displacement and pressure fields. Section 4 is crucial: we demonstrate there the good numerical properties enjoyed by the OFE method mentioned above, such as the tighter bandwidth and the smaller number of DoF's. Section 5 investigates the inf-sup stability of the pairs of OFE spaces introduced in Section 3. The relative insensitivity to mesh distortions is discussed through a problem solution in Section 6, and Section 7 presents another analysis which once more corroborates the effectiveness of our method, when compared with traditional finite elements. Finally, the concluding remarks are presented in Section 8.

2. THE EQUATIONS OF ELASTICITY

2.1. *The infinitesimal theory*

Let Ω_0 denote the region in $\mathbb{R}^3$ occupied by the body before the deformation, i.e., the *reference configuration* at time $t = 0$. At a time t after the deformation, each material point $\mathbf{X}$ in Ω_0 is mapped to the spatial point $\mathbf{x} = \mathbf{X} + \mathbf{u}(\mathbf{X}, t)$ in Ω_t, where $\mathbf{u}$ is the displacement vector, see Fig. 1. The equation of motion in the *deformed configuration* is given by [28]:

$$\nabla \cdot \widetilde{\mathbf{T}}(\mathbf{x}, t) + \rho(\mathbf{x}, t)\mathbf{b}(\mathbf{x}, t) = \rho(\mathbf{x}, t)\mathbf{a}(\mathbf{x}, t), \text{ for any } \mathbf{x} \in \Omega_t, \tag{2.1}$$

where $\widetilde{\mathbf{T}}$, ρ, $\mathbf{b}$, and $\mathbf{a}$ are the Cauchy stress tensor, density, body forces (given), and acceleration, respectively. In the infinitesimal theory of linear elasticity, we assume that the displacement vector $\mathbf{u}$ and its derivatives are very small, and it is not necessary to distinguish between the material coordinates $\mathbf{X}$ and the spatial coordinates $\mathbf{x}$ [22,28]. We will then write all equations in terms of $\mathbf{x}$. Moreover, in this work, we are interested in *static analyses*, i.e., the forces $\mathbf{b}$ do not depend on the time t, and the system has reached the equilibrium (stationary state), so that (2.1) becomes:

$$\nabla \cdot \widetilde{\mathbf{T}}(\mathbf{x}) + \rho(\mathbf{x})\mathbf{b}(\mathbf{x}) = 0, \text{ for any } \mathbf{x} \in \Omega, \tag{2.2}$$

where $\Omega := \Omega_0$. Equation (2.2) must be complemented by boundary conditions, which are given by:

$$\begin{aligned} &\mathbf{u}(\mathbf{x}) = 0, \text{ for any } \mathbf{x} \in \Gamma_D, \\ &\widetilde{\mathbf{T}}(\mathbf{x})\mathbf{n}(\mathbf{x}) = \mathbf{g}(\mathbf{x}), \text{ for any } \mathbf{x} \in \Gamma_N. \end{aligned} \tag{2.3}$$

We assume that the boundary $\partial\Omega$ can be decomposed as $\partial\Omega = \overline{\Gamma}_D \cup \overline{\Gamma}_N$, where Γ_D and Γ_N are two open subsets of $\partial\Omega$ (the Dirichlet and Neumann boundaries, respectively), with $\Gamma_D \cap \Gamma_N = \varnothing$. We also assume that Γ_D has nonzero measure. In (2.3) above, $\mathbf{n}(\mathbf{x})$ is the outward-pointing unit normal vector, and $\mathbf{g}(\mathbf{x})$ is the prescribed traction, both evaluated at $\mathbf{x} \in \Gamma_N$.

2.2. *Weak formulation*

For Lipschitz domains $\Omega \subset \mathbb{R}^3$, we assume that the displacement field $\mathbf{u}$ is such that $\mathbf{u} \in \mathbf{H}^1_{0,\Gamma_D}(\Omega)$, which is an abbreviation for $H^1_{0,\Gamma_D}(\Omega) \times H^1_{0,\Gamma_D}(\Omega) \times H^1_{0,\Gamma_D}(\Omega)$. Of course, $H^1(\Omega)$ is the Sobolev space of all scalar functions which are square-integrable in Ω, and whose (weak) first derivatives are also square-integrable in Ω. Finally, $H^1_{0,\Gamma_D}(\Omega)$ is the subspace formed by all functions in $H^1(\Omega)$ which have zero trace along the Dirichlet boundary Γ_D [11]. In order to derive a weak form, it is better to express (2.2) and (2.3) in component form as:

$$\begin{aligned} &T_{ij,j} + \rho b_i = 0, \text{ in } \Omega, \\ &u_i = 0, \text{ on } \Gamma_D, \\ &T_{ij}n_j = g_i, \text{ on } \Gamma_N, \end{aligned} \tag{2.4}$$

where we omitted the dependence on $\mathbf{x}$. The T_{ij} are the components of the tensor $\widetilde{\mathbf{T}}$, and b_i, u_i, n_j, and g_i are the components of the vectors $\mathbf{b}$, $\mathbf{u}$, $\mathbf{n}$, and $\mathbf{g}$, respectively, where $i,j = 1,2,3$. Moreover, the comma denotes a partial derivative with respect to x_j, i.e., $T_{ij,j} = \partial T_{ij}/\partial x_j$. The summation convention is assumed, i.e., repeated indices in the same term indicate summation [28].

From continuum mechanics, we know that under suitable conditions, the Cauchy stress tensor $\widetilde{\mathbf{T}}$ is symmetric, i.e., $T_{ji} = T_{ij}$ [28]. The method of weighted residuals applied to (2.4) yields, for any $v_i \in H^1_{0,\Gamma_D}(\Omega)$ [1,2,21]:

$$0 = \int\limits_{\Omega} v_i\left(T_{ij,j} + \rho b_i\right) d\Omega = -\int\limits_{\Omega} v_{i,j}T_{ij} d\Omega + \int\limits_{\partial\Omega} v_i T_{ij} n_j d\Gamma + \int\limits_{\Omega} \rho v_i b_i d\Omega, \tag{2.5}$$

where we used the integration by parts formula. It is known that, since $\widetilde{\mathbf{T}}$ is a symmetric tensor, then $v_{i,j}T_{ij} = v_{(ij)}T_{ij}$, where $v_{(ij)} := \left(v_{i,j} + v_{j,i}\right)/2$ are the components of the symmetric part of the tensor $\nabla\mathbf{v}$ (whose component at row i and column j is given by $v_{i,j}$, see [21]). Substituting the Neumann condition from (2.4) into the expression above, we arrive at the weak form of the problem:

$$\begin{aligned}&\text{Find } u_i \in H^1_{0,\Gamma_D}(\Omega) \text{ such that}\\ &\int_\Omega v_{(ij)} T_{ij} d\Omega = \int_{\Gamma_N} v_i g_i d\Gamma + \int_\Omega \rho v_i b_i d\Omega, \text{ for any } v_i \in H^1_{0,\Gamma_D}(\Omega),\end{aligned} \tag{2.6}$$

since $v_i = 0$ along Γ_D.

2.3. Constitutive equations

The components of the displacement vector $\mathbf{u}$ enter Eq. (2.6) above via Hooke's law as $T_{ij} = C_{ijkl} u_{(kl)}$, where C_{ijkl} are the components of the fourth-order elastic tensor, and $u_{(kl)} := \left(u_{k,l} + u_{l,k}\right)/2$ are the components of the symmetric part of the tensor $\nabla \mathbf{u}$, known as the *infinitesimal strain tensor* $\overset{=}{\epsilon}(\mathbf{u})$ [28]. Of course, $i,j,k,l = 1,2,3$, and we can rewrite problem (2.6) as:

$$\begin{aligned}&\text{Find } u_i \in H^1_{0,\Gamma_D}(\Omega) \text{ such that}\\ &\int_\Omega v_{(ij)} C_{ijkl} u_{(kl)} d\Omega = \int_{\Gamma_N} v_i g_i d\Gamma + \int_\Omega \rho v_i b_i d\Omega, \text{ for any } v_i \in H^1_{0,\Gamma_D}(\Omega).\end{aligned} \tag{2.7}$$

For *isotropic* materials, the components C_{ijkl} are given by $C_{ijkl} = \mu\left(\delta_{ik}\delta_{jl} + \delta_{il}\delta_{jk}\right) + \lambda \delta_{ij}\delta_{kl}$, where δ is the Kronecker delta [28]. If the material is *homogeneous*, the Lamé coefficients μ and λ, in addition to the density ρ, are all constant. Substituting this expression into (2.7), we obtain:

$$\begin{aligned}&\text{Find } u_i \in H^1_{0,\Gamma_D}(\Omega) \text{ such that}\\ &\int_\Omega \left(2\mu v_{(ij)} u_{(ij)} + \lambda v_{i,i} u_{k,k}\right) d\Omega = \int_{\Gamma_N} v_i g_i d\Gamma + \int_\Omega \rho v_i b_i d\Omega, \text{ for any } v_i \in H^1_{0,\Gamma_D}(\Omega).\end{aligned} \tag{2.8}$$

In the *incompressible* limit, $u_{k,k} = \nabla \cdot \mathbf{u}$ approaches zero, whereas λ becomes arbitrarily large, i.e., $\lambda \to \infty$. We therefore introduce an indeterminate pressure $p := -\lambda u_{k,k}$, which becomes a new unknown in the problem [22]. Since we assumed that $u_i \in H^1_{0,\Gamma_D}(\Omega)$, then all derivatives $u_{i,j}$ are square-integrable, i.e., $u_{i,j} \in L^2(\Omega)$. Consequently, the sum $u_{k,k}$ also belongs to $L^2(\Omega)$. We therefore arrive at the problem:

$$\begin{aligned}&\text{Find } u_i \in H^1_{0,\Gamma_D}(\Omega) \text{ and } p \in L^2(\Omega) \text{ such that}\\ &2\mu \int_\Omega v_{(ij)} u_{(ij)} d\Omega - \int_\Omega p v_{i,i} d\Omega = \int_{\Gamma_N} v_i g_i d\Gamma + \int_\Omega \rho v_i b_i d\Omega, \text{ for any } v_i \in H^1_{0,\Gamma_D}(\Omega),\\ &\int_\Omega q u_{k,k} d\Omega = 0, \text{ for any } q \in L^2(\Omega),\end{aligned} \tag{2.9}$$

where the incompressibility constraint $u_{k,k} = 0$ has been imposed weakly. The weak problem above can be rewritten in index-free notation as:

$$\begin{aligned}&\text{Find } (\mathbf{u}, p) \in \mathbf{H}^1_{0,\Gamma_D}(\Omega) \times L^2(\Omega) \text{ such that}\\ &2\mu \int_\Omega \overset{=}{\epsilon}(\mathbf{v}) : \overset{=}{\epsilon}(\mathbf{u}) d\Omega - \int_\Omega p \nabla \cdot \mathbf{v} d\Omega = \int_{\Gamma_N} \mathbf{v} \cdot \mathbf{g} d\Gamma + \int_\Omega \rho \mathbf{v} \cdot \mathbf{b} d\Omega, \text{ for any } \mathbf{v} \in \mathbf{H}^1_{0,\Gamma_D}(\Omega),\\ &\int_\Omega q \nabla \cdot \mathbf{u} d\Omega = 0, \text{ for any } q \in L^2(\Omega).\end{aligned} \tag{2.10}$$

Of course, the components of the tensor $\overset{=}{\epsilon}(\mathbf{v})$ are given by $v_{(ij)} = \left(v_{i,j} + v_{j,i}\right)/2$, from which it follows that $v_{(ii)} = v_{i,i} = \nabla \cdot \mathbf{v}$. We introduce the bilinear forms a and b defined as:

$$\begin{aligned}a(\mathbf{w}, \mathbf{v}) &:= 2\mu \int_\Omega \overset{=}{\epsilon}(\mathbf{v}) : \overset{=}{\epsilon}(\mathbf{w}) d\Omega,\\ b(\mathbf{v}, q) &:= -\int_\Omega q \nabla \cdot \mathbf{v} d\Omega,\end{aligned} \tag{2.11}$$

for any $(\mathbf{v}, \mathbf{w}) \in \mathbf{H}^1(\Omega) \times \mathbf{H}^1(\Omega)$ and any $(\mathbf{v}, q) \in \mathbf{H}^1(\Omega) \times L^2(\Omega)$, respectively, and introduce also the linear form F given by:

$$F(\mathbf{v}) := \int_{\Gamma_N} \mathbf{v} \cdot \mathbf{g} d\Gamma + \int_\Omega \rho \mathbf{v} \cdot \mathbf{b} d\Omega, \tag{2.12}$$

for any $\mathbf{v} \in \mathbf{H}^1(\Omega)$, where we assume that $\mathbf{b} \in \mathbf{L}^2(\Omega)$ and $\mathbf{g} \in \mathbf{L}^2(\Gamma_N)$. Using (2.11) and (2.12), we can rewrite (2.10) as:

$$\begin{aligned} &\text{Find } (\mathbf{u}, p) \in \mathbf{H}^1_{0,\Gamma_D}(\Omega) \times L^2(\Omega) \text{ such that} \\ &a(\mathbf{u}, \mathbf{v}) + b(\mathbf{v}, p) = F(\mathbf{v}), \text{ for any } \mathbf{v} \in \mathbf{H}^1_{0,\Gamma_D}(\Omega), \\ &b(\mathbf{u}, q) = 0, \text{ for any } q \in L^2(\Omega). \end{aligned} \tag{2.13}$$

The system (2.13) above describes the weak problem of incompressible linear elasticity cast in mixed formulation.

Observation 1: In going from (2.7) to (2.8), we used the following reasoning:

$$\begin{aligned} v_{(ij)} C_{ijkl} u_{(k,l)} &= v_{(ij)} \left[\mu \left(\delta_{ik}\delta_{jl} + \delta_{il}\delta_{jk} \right) + \lambda \delta_{ij}\delta_{kl} \right] u_{(kl)} \\ &= \mu v_{(ij)} \left[\delta_{ik}\delta_{jl} \right] u_{(kl)} + \mu v_{(ij)} \left[\delta_{il}\delta_{jk} \right] u_{(kl)} + \lambda v_{(ij)} \left[\delta_{ij}\delta_{kl} \right] u_{(kl)} \\ &= \mu v_{(ij)} u_{(ij)} + \mu v_{(ij)} u_{(ji)} + \lambda v_{(ii)} u_{(kk)} \\ &= 2\mu v_{(ij)} u_{(ij)} + \lambda v_{(ii)} u_{(kk)} \\ &= 2\mu v_{(ij)} u_{(ij)} + \lambda v_{i,i} u_{k,k}. \end{aligned}$$

Observation 2: The Lamé coefficients μ and λ can be expressed in terms of the Young's modulus E_Y and of Poisson's ratio ν as:

$$\mu = \frac{E_Y}{2(1+\nu)} \text{ and } \lambda = \frac{\nu E_Y}{(1+\nu)(1-2\nu)}.$$

In the incompressible limit, it is the case that ν approaches 1/2, so that $\lambda \to \infty$, as stated above [28]. In the fully incompressible case ($\nu = 1/2$), it follows that $\mu = E_Y/3$. This value for μ must be used in (2.9) – (2.11).

3. OVERLAPPING FINITE ELEMENTS

3.1. Polyhedral elements

The first step is to partition the closure of the computational domain $\overline{\Omega}$ (i.e., Ω together with its boundary $\partial\Omega$) into a collection of tetrahedral cells, as it is routinely done in the standard finite element analysis of three-dimensional problems. Let this partition be

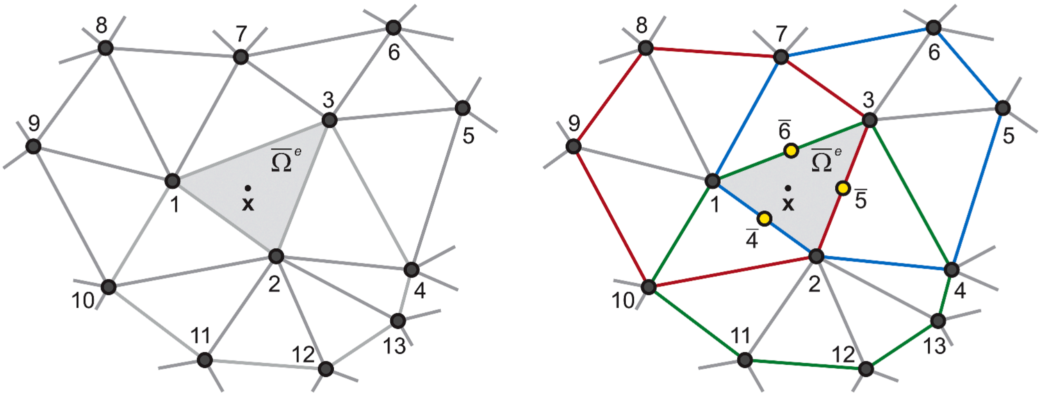

(a) *(b)*

Fig. 2. Two-dimensional illustration of the concepts introduced in this section. *(a)* A partition $\mathscr{T}_h$ of the domain $\overline{\Omega}$ into triangular cells. Each node is identified by a global index, which ranges from 1 to N. Later on, the DoF's will be assigned to these nodes only. *(b)* The polygonal element $\mathscr{P}_1$ centered at node 1 is formed by all cells attached to node 1. Its contour is shown in red. The corresponding support set $\mathscr{N}_1$ lists all nodes in the cells forming $\mathscr{P}_1$, and so $\mathscr{N}_1 = \{1, 2, 3, 7, 8, 9, 10\}$. In the same way, the polygonal elements $\mathscr{P}_2$ and $\mathscr{P}_3$ have their contours shown in green and blue, respectively. Their corresponding support sets are $\mathscr{N}_2 = \{2, 1, 3, 4, 13, 12, 11, 10\}$ and $\mathscr{N}_3 = \{3, 1, 2, 4, 5, 6, 7\}$.
The point $\mathbf{x}$ falls within the cell e, identified by its three nodes 1, 2, and 3. It is clear that its closure $\overline{\Omega}^e$ is the intersection of the polygonal elements $\mathscr{P}_1$, $\mathscr{P}_2$, and $\mathscr{P}_3$ (a region marked in gray). If we are to construct quadratic basis functions within this cell, six nodes are necessary; their positions $\mathbf{x}_i$ are the three vertices 1,2,3 and the edge midpoints $\overline{4}$, $\overline{5}$, and $\overline{6}$. When we consider the polygonal element $\mathscr{P}_1$, it is clear that, at all nodes $\mathbf{x}_i$, the hat functions are such that $h_7(\mathbf{x}_i) = h_8(\mathbf{x}_i) = h_9(\mathbf{x}_i) = h_{10}(\mathbf{x}_i) = 0$, in other words, $h_K(\mathbf{x}_i) = 0$ for each K in $\mathscr{N}_1$ which is not a vertex of cell e, i.e., for $K \neq 1, 2, 3$. The same happens for the polygonal elements $\mathscr{P}_2$ and $\mathscr{P}_3$: $h_K(\mathbf{x}_i) = 0$ for all K in $\mathscr{N}_2$ and all K in $\mathscr{N}_3$ different from $1, 2, 3$.
In the generalization to three dimensions (not shown), the point $\mathbf{x}$ falls within a tetrahedral cell e identified by its four vertices $1, \cdots, 4$, and whose closure $\overline{\Omega}^e$ is the intersection of the polyhedral elements $\mathscr{P}_1, \cdots, \mathscr{P}_4$. The quadratic basis functions within $\overline{\Omega}^e$ require ten nodes: they are located at the four vertices $1, \cdots, 4$ and at the edge midpoints $\overline{5}$, $\overline{6}, \cdots, \overline{10}$ (see Fig. 3). For each polygonal element $\mathscr{P}_I$ (where $I = 1, \cdots, 4$), it is the case that, for each K in $\mathscr{N}_I$ which is not a vertex of cell e, i.e., for $K \neq 1, \cdots, 4$, we have $h_K(\mathbf{x}_i) = 0$, i.e., $h_K = 0$ at all nodes $\mathbf{x}_i$.

denoted by $\mathscr{T}_h$, where the subscript h here refers to the *discretization length*, generally defined as the length of the largest edge in the partition $\mathscr{T}_h$. The nodes in $\mathscr{T}_h$ are numbered from 1 to N (global indices), and the cells in $\mathscr{T}_h$ are numbered from 1 to E. Each tetrahedral cell $e = 1, \cdots, E$ can be identified by a set of four numbers between 1 and N (the global indices of the four nodes in the cell). Cell e occupies the region Ω^e in $\mathbb{R}^3$, and its closure (the interior of the cell together with its boundary $\partial\Omega^e$, corresponding to its faces, edges, and vertices) is denoted by $\overline{\Omega}^e$.

For each node $I = 1, \cdots, N$, we consider the set of all cells in the partition $\mathscr{T}_h$ which have this node I at one of its vertices (i.e., the set of all cells that are attached to node I). The closure of this set is called the *polyhedral element centered at node I* (the three-dimensional counterpart of the two-dimensional *polygonal elements* defined in [30], indicated by $\mathscr{P}_I$, see Fig. 2. The *support set* $\mathscr{N}_I$ lists the indices of all nodes in the cells forming $\mathscr{P}_I$. Of course, node I belongs to $\mathscr{N}_I$. We define a collection of (two-index) weight functions $W_{I,K}$ as:

$$W_{I,K} := \begin{cases} \gamma h_K^2, & \text{if } K = I, \\ h_K, & \text{if } K \neq I, \end{cases} \tag{3.1}$$

where $I = 1, \cdots, N$ and $K \in \mathscr{N}_I$. In (3.1), γ is a free parameter and h_K is the first-order Lagrange basis function (i.e., the "hat" function, used in the construction of the 4-node element [1,2]) associated with node K. Next, we define the collection of functions $\Phi_{I,K}$ as:

$$\Phi_{I,K} := \frac{W_{I,K}}{\sum_{J \in \mathscr{N}_I} W_{I,J}}, \tag{3.2}$$

again for all $I = 1, \cdots, N$ and for all $K \in \mathscr{N}_I$.

3.2. Local basis functions

In order to approximate a scalar quantity s within the computational domain $\overline{\Omega}$, we first associate a set of local basis functions $\{l_{I,1}, l_{I,2}, \cdots\}$ (or local enrichment functions) and a set of coefficients $\{\widetilde{s}_{I,1}, \widetilde{s}_{I,2}, \cdots\}$ with each node $I = 1, \cdots, N$ in the domain. The local basis functions $\{l_{I,1}, l_{I,2}, \cdots\}$ are functions of the position $\mathbf{x} = (x, y, z)$ within $\overline{\Omega}$. When they are multiplied by the corresponding coefficients, each node I carries a function S_I given by:

$$S_I = l_{I,1}\widetilde{s}_{I,1} + l_{I,2}\widetilde{s}_{I,2} + \cdots, \tag{3.3}$$

i.e., S_I is an element of *span* $\{l_{I,1}, l_{I,2}, \cdots\}$. Usually, the local basis functions are monomials, so that S_I is a polynomial in x, y, and z. The coefficients $\{\widetilde{s}_{I,1}, \widetilde{s}_{I,2}, \cdots\}$ are the degrees of freedom (DoF's), or unknowns in the problem, which will ultimately be solved for in the resulting system of linear algebraic equations. In this paper, we choose the local basis functions as follows: for any point $\mathbf{x} = (x, y, z)$ within the computational domain $\overline{\Omega}$,

$$\begin{aligned} l_{I,1}(\mathbf{x}) &:= 1, \\ l_{I,2}(\mathbf{x}) &:= (x - x_I)/\delta_I, \\ l_{I,3}(\mathbf{x}) &:= (y - y_I)/\delta_I, \\ l_{I,4}(\mathbf{x}) &:= (z - z_I)/\delta_I, \end{aligned} \tag{3.4}$$

i.e., in principle we will choose sets with four local basis functions each, which results in a full degree 1 polynomial in x, y, and z assigned to each node $I = 1, \cdots, N$. The position of node I in $\mathbb{R}^3$ is given by $\mathbf{x}_I = (x_I, y_I, z_I)$, and $\delta_I = r_I/2$, where r_I is the maximum distance between node I and all the other nodes in the polyhedral element $\mathscr{P}_I$ (whose nodes are listed in the support set $\mathscr{N}_I$), i.e.,

$$r_I := \max_{J \in \mathscr{N}_I} \|\mathbf{x}_I - \mathbf{x}_J\|, \tag{3.5}$$

where of course $\|\cdot\|$ denotes the Euclidean norm of vectors in $\mathbb{R}^3$.

3.3. Interpolations

Suppose we want to approximate our scalar quantity s at an arbitrary point $\mathbf{x}$ within the computational domain $\overline{\Omega}$. This point $\mathbf{x}$ will fall within the closure of one of the cells in the partition $\mathscr{T}_h$, for example, the cell indexed by e (say), so that $\mathbf{x} \in \overline{\Omega}^e$. This tetrahedral cell e can be identified by the global indices of its four nodes (located at the vertices). For the sake of clarity, let us use a local indexing scheme and assume that these four nodes have indices given by 1, 2, 3, and 4. Clearly, this point $\mathbf{x}$ will be located within the intersection of the polyhedral elements centered at nodes 1, 2, 3, and 4, i.e., within the intersection of $\mathscr{P}_1$, $\mathscr{P}_2$, $\mathscr{P}_3$, and $\mathscr{P}_4$. The intersection, or *overlapping* of these four polyhedral elements is just $\overline{\Omega}^e$, see Fig. 2. (Due to the impossibility of providing a clear and understandable drawing in three dimensions, Fig. 2 shows a two-dimensional counterpart to these concepts. The generalization to three dimensions is immediate.)

Let us recall that within this tetrahedral cell e, we can construct a set of 10 quadratic basis functions corresponding to 10 nodes used: four nodes at the four vertices of the cell and six nodes at the midpoints of the six edges connecting these vertices. In a local indexing scheme, the indices of the nodes at the vertices of the cell are 1, 2, 3, and 4 (as we pointed out above), whereas the indices of the other nodes at the edge midpoints are $\overline{5},\ \overline{6},\cdots,\overline{10}$, see Fig. 3. The indices of these "virtual nodes" at the edge midpoints are written with an overbar, in order to distinguish them from the nodes located at the vertices. The positions of the nodes in $\mathbb{R}^3$ are given by the vectors $\mathbf{x}_i$, $i = 1,\cdots,\overline{10}$, and they all lie along the boundary of cell e. The quadratic basis functions defined within the cell e are denoted by $\widehat{h}_i$, for $i = 1,\cdots,\overline{10}$, and they are used in the construction of the 10-node elements [1,2]. Let I^e be the interpolation operator which takes any function f and returns its interpolation in terms of the quadratic basis functions within cell e, i.e., I^e takes any function f and returns the element $I^e f$ in *span* $\{\widehat{h}_1,\cdots,\widehat{h}_{\overline{10}}\}$ given by:

$$(I^e f)(\mathbf{x}) := \sum_{i=1}^{\overline{10}} \widehat{h}_i(\mathbf{x}) f_i, \tag{3.6}$$

where the coefficients f_i in the linear combination (3.6) are given by f evaluated at the nodes $\mathbf{x}_i$, i.e., $f_i = f(\mathbf{x}_i)$, for $i = 1,\cdots,\overline{10}$. Since point $\mathbf{x}$ belongs to $\overline{\Omega}^e$, which in turn is the intersection of the polyhedral elements $\mathscr{P}_1$, $\mathscr{P}_2$, $\mathscr{P}_3$, and $\mathscr{P}_4$ (see Fig. 2), we define the contributions of these polyhedral elements within $\overline{\Omega}^e$ as the functions ψ_1^e, ψ_2^e, ψ_3^e, and ψ_4^e, evaluated at $\mathbf{x}$:

$$\psi_I^e(\mathbf{x}) := \sum_{K\in\mathscr{N}_I} \left(I^e \Phi_{I,K}\right)(\mathbf{x}) S_K(\mathbf{x}), \tag{3.7}$$

for $I = 1,\cdots,4$. Of course, S_K is the polynomial associated with node K, see (3.3) and (3.4). According to (3.6), the interpolation of $\Phi_{I,K}$ evaluated at point $\mathbf{x}$ is given by:

$$\left(I^e \Phi_{I,K}\right)(\mathbf{x}) := \sum_{i=1}^{\overline{10}} \widehat{h}_i(\mathbf{x}) \Phi_{I,K}(\mathbf{x}_i), \tag{3.8}$$

where the $\Phi_{I,K}$ is given in (3.2). Next, the approximation s^h of the quantity s within cell e is defined by:

$$s^h\big|_{\Omega^e}(\mathbf{x}) := \sum_{I=1}^{4} h_I(\mathbf{x}) \psi_I^e(\mathbf{x}), \tag{3.9}$$

where h_I is the "hat" function associated with node I.

Observation: Given a cell as in Fig. 3, the DoF's in (3.3) are ascribed to the nodes 1, 2, 3, and 4 only; there are no DoF's ascribed to the "virtual nodes" $\overline{5},\ \overline{6},\cdots,\overline{10}$ at the edge midpoints. These nodes are just an aid to construct the quadratic basis functions used in the interpolations (3.6).

3.4. *The modulating functions*

We omit the dependence on $\mathbf{x}$, and use (3.7) and (3.8) in (3.9), arriving at:

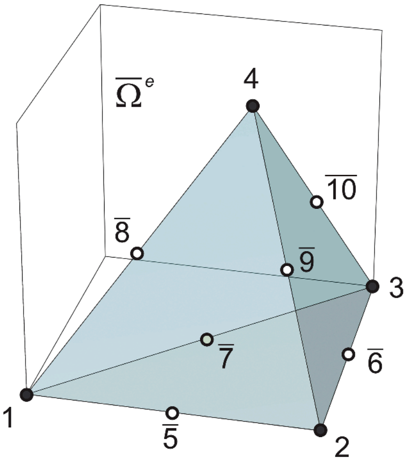

Fig. 3. The nodes used in the construction of the quadratic basis functions $\widehat{h}_i$ within an arbitrary tetrahedral cell e: they are located at the vertices $1,\cdots,4$ (assuming a local indexing scheme) and at the edge midpoints (indices $\overline{5},\ \overline{6},\cdots,\overline{10}$).

$$s^h\big|_{\Omega^e} = \sum_{I=1}^{4} \sum_{K\in\mathscr{N}_I} \sum_{i=1}^{\overline{10}} h_I \widehat{h}_i \Phi_{I,K}(\mathbf{x}_i) S_K. \tag{3.10}$$

The coefficients $\Phi_{I,K}(\mathbf{x}_i)$ for $I = 1,\cdots,4$, $K \in \mathscr{N}_I$, and $i = 1,\cdots,\overline{10}$ can be easily calculated. For example, to determine the coefficients $\Phi_{1,K}(\mathbf{x}_i)$, we first make $I = 1$ in (3.1) and discover that, for each node $\mathbf{x}_i$,

$$W_{1,K}(\mathbf{x}_i) = \begin{cases} \gamma h_K(\mathbf{x}_i)^2, \ \textit{for } K = 1, \\ h_K(\mathbf{x}_i), \ \textit{for } K = 2,3,4, \\ \quad 0, \ \textit{otherwise}, \end{cases} \tag{3.11}$$

because $h_K(\mathbf{x}_i) = 0$ for the other K in $\mathscr{N}_1$ which are not vertices of cell e (i.e., for $K \neq 1,\cdots,4$), see Fig. 2. It follows from (3.2) and (3.11) that:

$$\Phi_{1,K}(\mathbf{x}_i) := \frac{W_{1,K}(\mathbf{x}_i)}{\sum_{J\in\mathscr{N}_1} W_{1,J}(\mathbf{x}_i)} = \frac{W_{1,K}(\mathbf{x}_i)}{\sum_{J=1}^{4} W_{1,J}(\mathbf{x}_i)}$$

$$= \begin{cases} \dfrac{\gamma h_1(\mathbf{x}_i)^2}{\gamma h_1(\mathbf{x}_i)^2 + h_2(\mathbf{x}_i) + h_3(\mathbf{x}_i) + h_4(\mathbf{x}_i)}, \ \textit{for } K = 1, \\ \dfrac{h_K(\mathbf{x}_i)}{\gamma h_1(\mathbf{x}_i)^2 + h_2(\mathbf{x}_i) + h_3(\mathbf{x}_i) + h_4(\mathbf{x}_i)}, \ \textit{for } K = 2,3,4, \\ \qquad 0, \ \textit{otherwise}, \end{cases} \tag{3.12}$$

i.e., $\Phi_{1,K}(\mathbf{x}_i) = 0$ for all K in $\mathscr{N}_1$ such that $K \neq 1,\cdots,4$. The same result is reached when we make $I = 2,3,4$ in (3.1). The conclusion is that for all $I = 1,\cdots,4$, for all K in $\mathscr{N}_I$ such that $K \neq 1,\cdots,4$, and for all $i = 1,\cdots,\overline{10}$, it is the case that $\Phi_{I,K}(\mathbf{x}_i) = 0$. The consequence is that (3.10) can be rewritten as:

$$s^h\big|_{\Omega^e} = \sum_{I=1}^{4} \sum_{K=1}^{4} \sum_{i=1}^{\overline{10}} h_I \widehat{h}_i \Phi_{I,K}(\mathbf{x}_i) S_K = \sum_{K=1}^{4} \underbrace{\left(\sum_{I=1}^{4} \sum_{i=1}^{\overline{10}} h_I \widehat{h}_i \Phi_{I,K}(\mathbf{x}_i) \right)}_{\rho_K} S_K = \sum_{K=1}^{4} \rho_K S_K. \tag{3.13}$$

We see from (3.13) that each vertex K of cell e will now carry a function ρ_K, in addition to the polynomial S_K. The functions ρ_K will ‘modulate’ the polynomials S_K within the cell, an action that will ultimately return the approximation s^h. The remaining coefficients $\Phi_{I,K}(\mathbf{x}_i)$ for $I = 1,\cdots,4$, $K = 1,\cdots,4$ and $i = 1,\cdots,\overline{10}$ can be retrieved from expressions like (3.12). The majority of these values $\Phi_{I,K}(\mathbf{x}_i)$ are again zero, and they have been tabulated (see Table A3 in [30]). After the calculations, we finally obtain all modulating functions in terms of the “hat” and quadratic basis functions:

$$\begin{aligned} \rho_1 &= h_1 + \beta(h_2 - h_1)\widehat{h}_{\overline{5}} + \beta(h_3 - h_1)\widehat{h}_{\overline{7}} + \beta(h_4 - h_1)\widehat{h}_{\overline{8}}, \\ \rho_2 &= h_2 + \beta(h_1 - h_2)\widehat{h}_{\overline{5}} + \beta(h_3 - h_2)\widehat{h}_{\overline{6}} + \beta(h_4 - h_2)\widehat{h}_{\overline{9}}, \\ \rho_3 &= h_3 + \beta(h_2 - h_3)\widehat{h}_{\overline{6}} + \beta(h_1 - h_3)\widehat{h}_{\overline{7}} + \beta(h_4 - h_3)\widehat{h}_{\overline{10}}, \\ \rho_4 &= h_4 + \beta(h_1 - h_4)\widehat{h}_{\overline{8}} + \beta(h_2 - h_4)\widehat{h}_{\overline{9}} + \beta(h_3 - h_4)\widehat{h}_{\overline{10}}. \end{aligned} \tag{3.14}$$

It is clear from above that $\rho_1 + \cdots + \rho_4 = 1$. The parameter β is given in terms of the parameter γ in (3.1). The exact relationship is $\beta = (2-\gamma)/(4+2\gamma)$, see [30]. Throughout this paper, we choose $\beta = 0.01$. This value was studied in [30] and found to be appropriate for general analyses. The Eqs. (3.14) can be expressed in compact form as:

$$\rho_K = h_K + \beta \sum_J (h_J - h_K)\widehat{h}_{JK}, \tag{3.15}$$

for $K = 1,\cdots,4$, where J runs over the three vertices connected to vertex K along some edge, and $\widehat{h}_{JK}$ is the quadratic basis function associated with the “virtual” node located at the midpoint of the edge connecting vertices J and K (see Fig. 3). The h_K are polynomials of degree 1, whereas the $\widehat{h}_{JK}$ are polynomials of degree 2. Since the value of β is very small ($\beta = 0.01$), each ρ_K is not seen as a “full” polynomial of degree 3, but rather as a polynomial of degree 1 with a small perturbation of degree 3.

3.5. Discretizing the displacement and pressure fields

In the discretization of our problem (2.10), the displacement field $\mathbf{u} = (u_1, u_2, u_3)$ and the pressure field p are approximated by their finite-dimensional counterparts $\mathbf{u}^h = \left(u_1^h, u_2^h, u_3^h\right)$ and p^h, respectively. According to Section 2.2, the components of the displacement field are such that $u_1, u_2, u_3 \in H^1_{0,\Gamma_D}(\Omega)$. Therefore, we must construct a finite-dimensional subspace $U^h \subset H^1_{0,\Gamma_D}(\Omega)$ and take $u_1^h, u_2^h, u_3^h \in U^h$. Analogously, according to Section 2.3, the pressure field is such that $p \in L^2(\Omega)$; we must construct a finite-dimensional subspace $Q^h \subset L^2(\Omega)$ and take $p^h \in Q^h$.

Having introduced suitable finite-dimensional subspaces U^h for the components of the displacement and Q^h for the pressure, we are led to the finite-dimensional version of problem (2.13):

$$\begin{aligned} &\text{Find } \left(\mathbf{u}^h, p^h\right) \in \mathbf{U}^h \times Q^h \text{ such that} \\ &a\left(\mathbf{u}^h, \mathbf{v}^h\right) + b\left(\mathbf{v}^h, p^h\right) = F\left(\mathbf{v}^h\right), \text{ for any } \mathbf{v}^h \in \mathbf{U}^h, \\ &b\left(\mathbf{u}^h, q^h\right) = 0, \text{ for any } q^h \in Q^h, \end{aligned} \tag{3.16}$$

where $\mathbf{U}^h$ is an abbreviation for $U^h \times U^h \times U^h$. In this paper we intend to use the *overlapping finite element approximations* defined in Sections 3.1-3.4 in the construction of our subspaces U^h and Q^h. This will lead to solution pairs of the form $\left(\mathbf{u}^h, p^h\right) \in \mathbf{OFE}_1 \times \mathrm{OFE}_0$ (see sections below). Of course, $\mathbf{OFE}_1$ is an abbreviation for $\mathrm{OFE}_1 \times \mathrm{OFE}_1 \times \mathrm{OFE}_1$, and "OFE" means "*overlapping finite element*". However, when establishing comparisons with other elements, we will consider different choices for U^h and Q^h, e.g., when we make $U^h = P_2$ (the space of piecewise quadratic or "10-node elements") and $Q^h = P_1$ (the space of piecewise linear or "4-node elements"), which leads to a solution pair $\left(\mathbf{u}^h, p^h\right)$ in the $\mathbf{P}_2 \times P_1$ (or Taylor-Hood) space, where $\mathbf{P}_2 = P_2 \times P_2 \times P_2$ [1,2].

3.5.1. *Treating the displacement field*

When approximating the components of the displacement field, we make $U^h = \mathrm{OFE}_1$, i.e., we use, for $i = 1, 2, 3$:

$$u_i^h \in \mathrm{OFE}_1 \;\Leftrightarrow\; u_i^h\big|_{\Omega^e} = \sum_{K=1}^{4} \rho_K U_{K,(i)}, \text{ for } e = 1, \cdots, E, \tag{3.17}$$

where each cell e is identified by the four nodes $K = 1, \cdots, 4$, assuming a local indexing. In the manner of (3.13), the ρ_K are the modulating functions from (3.14), and $U_{K,(i)}$ is the full degree 1 polynomial assigned to node K used in the calculation of the component u_i^h, i.e.,

$$U_{K,(i)} = l_{K,1}\widetilde{u}_{K,1,(i)} + l_{K,2}\widetilde{u}_{K,2,(i)} + l_{K,3}\widetilde{u}_{K,3,(i)} + l_{K,4}\widetilde{u}_{K,4,(i)}, \tag{3.18}$$

according to (3.3). (Hence the subscript "1" attached to "OFE" in the name of this space.) The coefficients $\left\{\widetilde{u}_{K,1,(i)}, \cdots, \widetilde{u}_{K,4,(i)}\right\}$ are the four DoF's associated with node K used in the calculation of u_i^h, and $\left\{l_{K,1}, \cdots, l_{K,4}\right\}$ are the four local enrichment basis functions associated with node K, defined in (3.4). The substitution of (3.18) allows us to rewrite (3.17) as:

$$u_i^h\big|_{\Omega^e} = \sum_{K=1}^{4} \sum_{m=1}^{4} \underbrace{\rho_K l_{K,m}}_{N_{K,m}} \widetilde{u}_{K,m,(i)},$$

and we can see that each two-index OFE basis function $N_{K,m} := \rho_K l_{K,m}$ is a polynomial of degree 2 with a small perturbation of degree 4, because ρ_K is a polynomial of degree 1 with a small perturbation of degree 3 (see Section 3.4).

The space OFE_1 in (3.17) thus uses 4 DoF's per node to calculate each component u_i^h, and so it needs a total of 12 DoF's per node to calculate the three components. Since we assumed at the beginning of Section 3.1 that the partition $\mathscr{T}_h$ has N nodes, we therefore need 12 N DoF's to completely characterize the displacement field $\mathbf{u}^h = \left(u_1^h, u_2^h, u_3^h\right)$.

Finally, we must ask the question: how do we know that the space OFE_1 in (3.17) is a subspace of $H^1(\Omega)$? The answer is affirmative, see Appendix A. To make now the OFE_1 space into a subspace of $H^1_{0,\Gamma_D}(\Omega)$, we have to force the trace of functions in OFE_1 to be zero along the Dirichlet boundary Γ_D, i.e., we have to impose the essential boundary conditions along Γ_D. This can be accomplished by setting all DoF's associated with nodes lying on Γ_D to zero [36]. For example, if the node with global index K lies on Γ_D, then in (3.18) we make $\widetilde{u}_{K,1,(i)} = \widetilde{u}_{K,2,(i)} = \widetilde{u}_{K,3,(i)} = \widetilde{u}_{K,4,(i)} = 0$, for $i = 1, 2, 3$.

3.5.2. *Treating the pressure field*

When approximating the pressure field, we make $Q^h = \mathrm{OFE}_0$, i.e., we use:

$$p^h \in \mathrm{OFE}_0 \;\Leftrightarrow\; p^h\big|_{\Omega^e} = \sum_{K=1}^{4} \rho_K P_K, \text{ for } e = 1, \cdots, E. \tag{3.19}$$

As before, each cell e is identified by the four nodes $K = 1, \cdots, 4$ (assuming a local indexing), and the ρ_K are the modulating functions in (3.14). The quantity P_K is the degree 0 polynomial assigned to node K used in the calculation of p^h, i.e.,

$$P_K = l_{K,1}\widetilde{p}_{K,1}. \tag{3.20}$$

(Hence the subscript “0” attached to “OFE” in the name of this space.) The coefficient $\widetilde{p}_{K,1}$ is the single DoF associated with node K used in the calculation of p^h, and $l_{K,1}$ is the first local enrichment basis function associated with node K, identically equal to 1, according to (3.4). The space OFE_0 in (3.19) thus uses only 1 DoF per node to calculate the pressure p^h. For our partition $\mathscr{T}_h$ with N nodes, we need N DoF’s to characterize the pressure field p^h.

As in Section 3.5.1, we ask: how do we know that the space OFE_0 in (3.19) is a subspace of $L^2(\Omega)$? Since the basis function $l_{K,1} \equiv 1$, the quantity P_K in (3.20) is just a real number. So $p^h|_{\Omega^e}$ is a linear combination of the modulating functions ρ_K, according to (3.19). But these functions are polynomials, and hence square-integrable on Ω^e, see Appendix A. Therefore p^h is square-integrable on the whole of Ω.

We can see that the expansions in (3.17) for the components of the displacement field and in (3.19) for the pressure field are similar; what changes is the type of local polynomials assigned to the nodes. We use a full degree 1 polynomial for each component of the displacement and a degree 0 polynomial for the pressure.

3.6. *Numerical integration*

The volume integral of a given scalar quantity f over the generic tetrahedral cell e in Fig. 3 can be approximated as:

$$\int_{\Omega^e} f(\mathbf{x})d\Omega \simeq V\sum_k w_k f(\mathbf{x}_k),$$

where V denotes the volume of the cell, $\mathbf{x}_k$ are the sampling points within Ω^e, and w_k is the weight associated with the k-th sampling point $\mathbf{x}_k$. In this paper, we use the 16-point rule whose weights and sampling points are tabulated in [24].

For example, if the above integrand f is the product between two scalar functions s^h and v^h in the OFE_1 space, it follows that f is a polynomial of degree 4 with a small perturbation of higher degree, since s^h and v^h are each given by a polynomial of degree 2 with a small perturbation of degree 4, see Section 3.5.1. But the 16-point rule integrates a polynomial of degree 4 exactly over a tetrahedron [24]. So, if any integration error is committed, it is committed in the integration of the perturbation only.

Likewise, the area integral of a given scalar quantity g over a generic triangular face Δ (e.g. those in the Neumann boundary Γ_N, where the traction $\mathbf{g}$ is prescribed, see (2.12)) is approximated as:

$$\int_{\Delta} g(\mathbf{x})d\Gamma \simeq A\sum_k w_k g(\mathbf{x}_k),$$

where A denotes the area of the triangular face, $\mathbf{x}_k$ are the sampling points within Δ, and w_k is the weight associated with the k-th sampling point $\mathbf{x}_k$. We use the 6-point rule whose weights and sampling points are tabulated in [12]. After we perform the numerical integrations as described above, we can rewrite the bilinear and linear forms in problem (3.16) as:

$$\begin{aligned} a(\mathbf{u}^h, \mathbf{v}^h) &= \widetilde{\mathbf{V}}^T\overline{\mathbf{A}}\widetilde{\mathbf{U}}, \\ b(\mathbf{v}^h, p^h) &= \widetilde{\mathbf{V}}^T\overline{\mathbf{B}}^T\widetilde{\mathbf{P}}, \\ F(\mathbf{v}^h) &= \widetilde{\mathbf{V}}^T\mathbf{F}, \\ b(\mathbf{u}^h, q^h) &= \widetilde{\mathbf{Q}}^T\overline{\mathbf{B}}\widetilde{\mathbf{U}}, \end{aligned} \tag{3.21}$$

where $\overline{\mathbf{A}}$ and $\overline{\mathbf{B}}$ are suitable matrices, $\mathbf{F}$ is a vector which incorporates the action of body forces and tractions, and $\widetilde{\mathbf{U}}$, $\widetilde{\mathbf{V}}$, $\widetilde{\mathbf{P}}$, and $\widetilde{\mathbf{Q}}$ are the vectors collecting the DoF’s in the expansion of $\mathbf{u}^h$, $\mathbf{v}^h$, p^h, and q^h, respectively. Substitution of (3.21) into (3.16) yields the saddle-point linear system of equations:

Find the DoF vectors $\widetilde{\mathbf{U}}$ and $\widetilde{\mathbf{P}}$ such that

$$\begin{bmatrix} \overline{\mathbf{A}} & \overline{\mathbf{B}}^T \\ \overline{\mathbf{B}} & \end{bmatrix}\begin{bmatrix} \widetilde{\mathbf{U}} \\ \widetilde{\mathbf{P}} \end{bmatrix} = \begin{bmatrix} \mathbf{F} \\ \mathbf{0} \end{bmatrix}. \tag{3.22}$$

As a last step before the solution of (3.22), we have to impose the essential boundary conditions along Γ_D. Since they are homogeneous, it suffices to remove from (3.22) all displacement DoF’s associated with the nodes lying on the Dirichlet boundary Γ_D, see Section 3.5.1.

4. NUMERICAL PROPERTIES

In this section we will verify some properties of the OFE discretization like solvability, bandwidth, and required number of DoF’s. We use the geometry of a cubic block as a model, and seek to establish comparisons with other discretization schemes.

4.1. The incompressible block

The computational domain Ω is a cubic block of side 50, i.e., $\overline{\Omega} = [0,L] \times [0,L] \times [0,L]$, where $L = 50$ (in dimensionless units). The bottom face of the cube (surface $z = 0$) is clamped, i.e., $\mathbf{u} = 0$. On the top face (surface $z = L = 50$), we consider a small square region of side 10 close to one of the corners, i.e., the region $0 \leq x \leq 10$, $0 \leq y \leq 10$, $z = 50$, indicated by red in Fig. 4, and apply a prescribed traction (pressure) given by $\mathbf{g} = [0, 0, -250]^T$. In other words, this portion of the top surface is pressed downwards. The remaining portion of the top surface, as well as the four lateral faces, are prescribed a traction $\mathbf{g} = 0$, i.e., they are free. The material the block is made of is incompressible, and we assume the values $E_Y = 210{,}000$ and $\rho = 1000$ for the Young's modulus and density, respectively. The body force is assumed to be zero, i.e., $\mathbf{b} = 0$.

Figs. 5*a*-5*c* show the components of the displacement field calculated by the $\mathbf{OFE}_1/\mathrm{OFE}_0$ pair, whereas Figs. 5*d*-5*f* show the same components calculated by the traditional $\mathbf{P}_2/P_1$ (Taylor-Hood) pair, using the mesh from Fig. 4. (From now on, we use "$\mathbf{OFE}_1\ /\mathrm{OFE}_0$" instead of "$\mathbf{OFE}_1 \times \mathrm{OFE}_0$" in order to indicate that the displacement and pressure have been approximated within the $\mathbf{OFE}_1$ and OFE_0 spaces, respectively. The same interpretation applies to "$\mathbf{P}_2/P_1$".) The results are almost indistinguishable from each other. To show the agreement between the $\mathbf{OFE}_1/\mathrm{OFE}_0$ and the $\mathbf{P}_2/P_1$ solutions, we plot the components of the displacement field along one of the edges of the cube, i.e., the line joining the corners at $[0, 0, 50]^T$ and $[50, 0, 50]^T$, whose parametric equation is given by $x(t) = 50t$, $y(t) = 0$, and $z(t) = 50$, where $0 \leq t \leq 1$. Figs. 5g and 5*h* show that the solutions are almost on top of each other.

However, for the same mesh with 1545 nodes and 7483 tetrahedral cells (shown in Fig. 4), the $\mathbf{OFE}_1/\mathrm{OFE}_0$ pair leads to a linear system with 20,085 DoF's (or unknowns), whereas the $\mathbf{P}_2/P_1$ pair leads to a system with 34,845 DoF's. So, for this particular problem, the $\mathbf{OFE}_1/\mathrm{OFE}_0$ pair produces results with the same precision as the $\mathbf{P}_2/P_1$ pair, but using just $20{,}085/34{,}845 \simeq 0.57 = 57\%$ of the number of DoF's (which is only 5% above the theoretical limit of 52%, see Section 4.4.1).

Fig. 6 shows the deformed block after we calculate the displacement field on the whole surface of the cube. We can see that the region of the solid immediately below the area where the pressure is applied is lowered/depressed and, in order to compensate for this localized loss of volume, adjacent portions of material are protruded (i.e., projected out of the volume of the original cube). This is expected, since the material is incompressible (its volume is preserved in deformations). Because the displacements are very small when compared with the side of the cube (in accordance with the infinitesimal theory of elasticity, see Section 2.1), the displacements in Fig. 6 have been multiplied by a scaling factor of 1000, i.e., the actual deformation experienced by the solid is 1000 times smaller than what is portrayed in the figures.

4.2. Solvability

As a first inquiry into the possible existence of spurious pressure modes [1,2], in this section we analyze the solvability of the linear system (3.22). We consider the same problem described in Section 4.1, and focus on the final form of the system (3.22), i.e., *after* the homogeneous boundary conditions have been imposed (zero DoF's removed from the problem). Now we use a sequence of uniform meshes with decreasing h. Each mesh is constructed by first subdividing the cubic domain $\overline{\Omega} = [0,L] \times [0,L] \times [0,L]$, where $L = 50$ (dimensionless), equally into $k \times k \times k$ little cubes; each little cube is then subdivided into six tetrahedra. In this study, we assumed a sequence of meshes for which $k = 3, 4, \cdots, 8$.

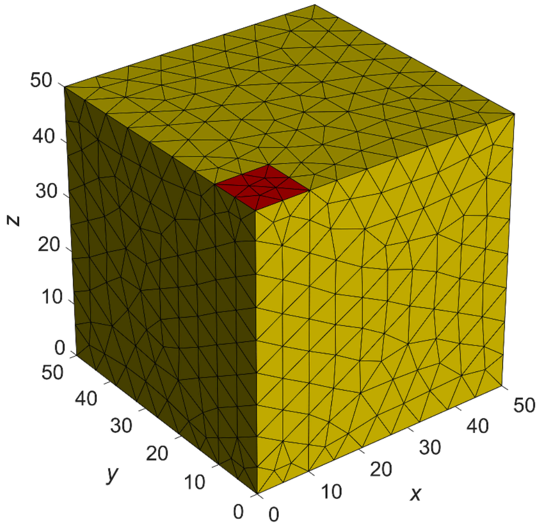

Fig. 4. The mesh used for the solution of the problem relative to the cubic block in Section 4.1. It is composed of 7483 tetrahedral cells. The nonzero traction is applied to the portion of the top face colored in red.

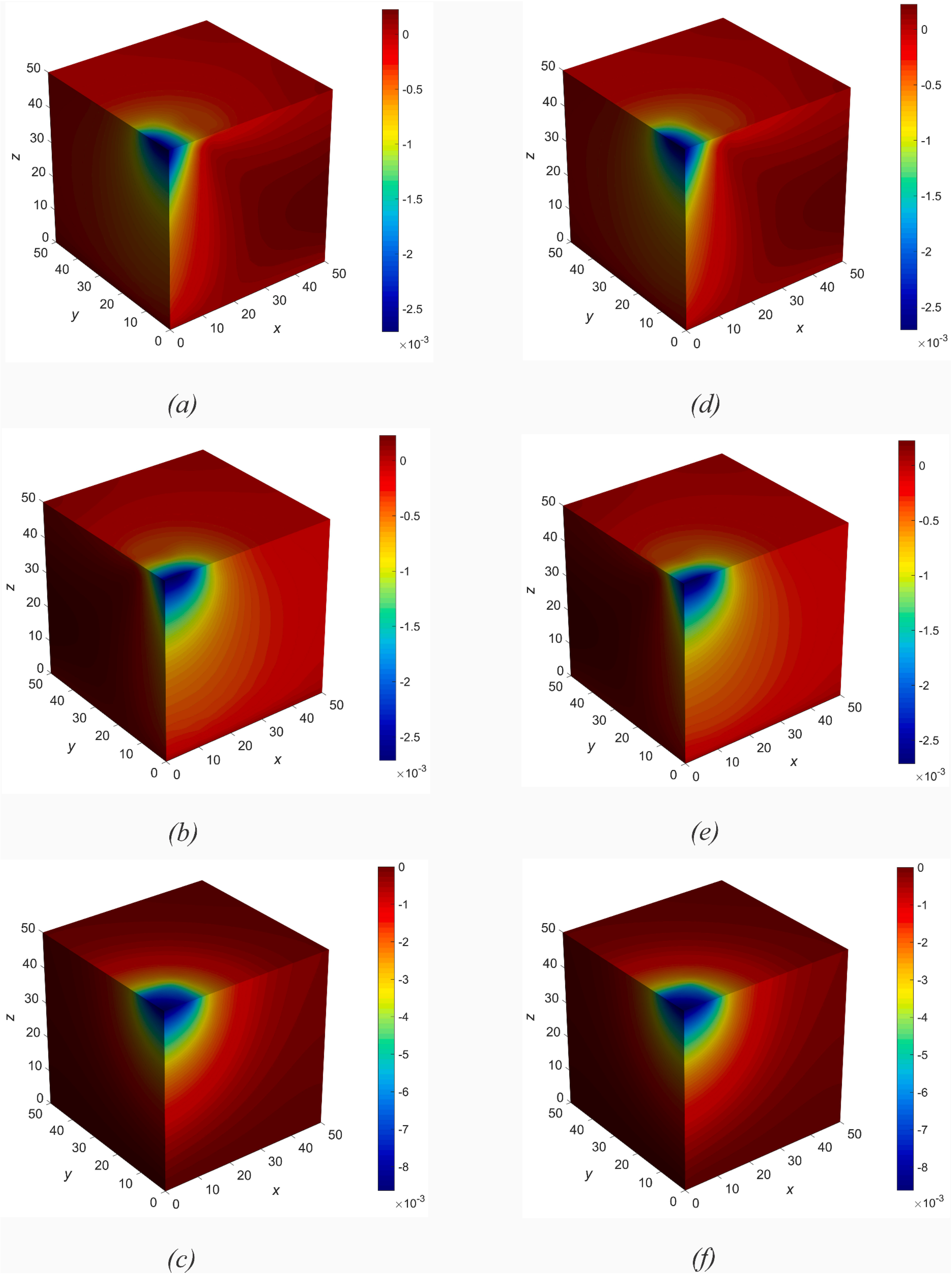

Fig. 5. The displacement field calculated over the surface of the cube. *(a)* through *(c)*: The components u_1^h, u_2^h, and u_3^h provided by the $\mathbf{OFE}_1/\mathrm{OFE}_0$ pair. *(d)* through *(f)*: The same components provided by the traditional $\mathbf{P}_2/P_1$ pair (Taylor-Hood). *(g)* The components of the displacement field calculated over the surface of the cube and along the line joining the corners at $[0,0,50]^T$ and $[50,0,50]^T$. The components are plotted as a function of the x-coordinate. *(h)* Magnifying the view around the point $x = 11$, in order to highlight the agreement between the curves provided by both pairs.

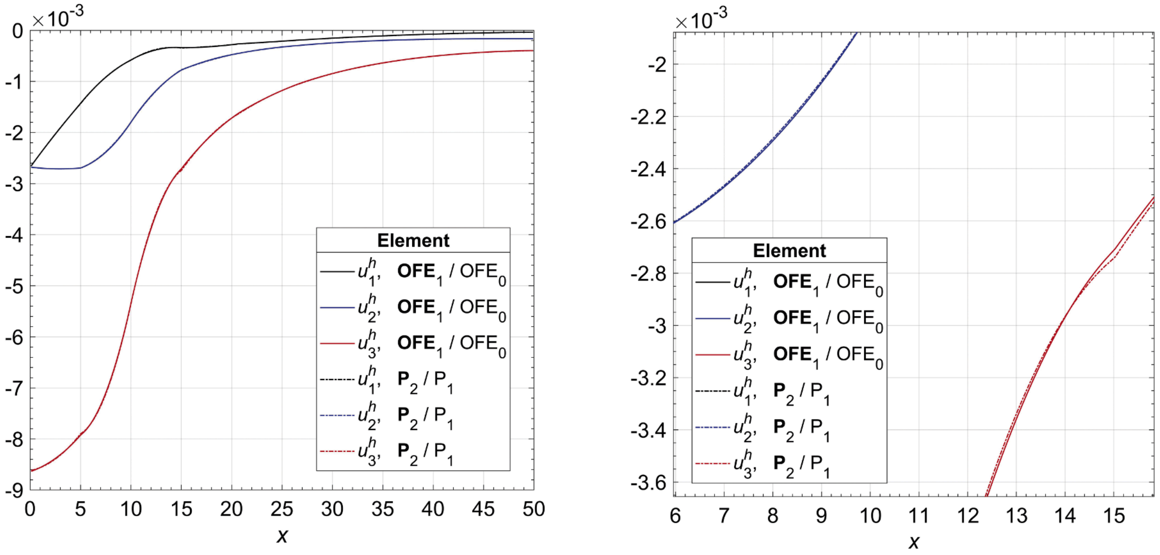

(g) (h)

Fig. 5. (*continued*).

Fig. 7 shows the mesh for $k = 5$. The subdivision of a little cube into six tetrahedra is carried out as follows: first, each little cube is sliced vertically along the diagonal of the top face, producing two symmetrical solids, see Fig. 8. These two solids are now subdivided into three tetrahedra each, as shown in Fig. 9. We now assume:

The matrix $\overline{\mathbf{A}}$ is invertible. (4.1)

If this is the case, we can multiply the first equation in (3.22) by the inverse $\overline{\mathbf{A}}^{-1}$ in order to obtain:

$$\widetilde{\mathbf{U}} + \overline{\mathbf{A}}^{-1}\overline{\mathbf{B}}^{T}\widetilde{\mathbf{P}} = \overline{\mathbf{A}}^{-1}\mathbf{F}.$$

Now we multiply this last equation by $\overline{\mathbf{B}}$ and arrive at

$$\overline{\mathbf{B}}\,\overline{\mathbf{A}}^{-1}\overline{\mathbf{B}}^{T}\widetilde{\mathbf{P}} = \overline{\mathbf{B}}\,\overline{\mathbf{A}}^{-1}\mathbf{F},$$

because $\overline{\mathbf{B}}\widetilde{\mathbf{U}} = \mathbf{0}$ (according to the second equation in (3.22)). We now define $\overline{\mathbf{C}} := \overline{\mathbf{B}}\,\overline{\mathbf{A}}^{-1}\overline{\mathbf{B}}^{T}$, so that the equation above becomes:

$$\overline{\mathbf{C}}\widetilde{\mathbf{P}} = \overline{\mathbf{B}}\overline{\mathbf{A}}^{-1}\mathbf{F}.$$

If we further assume that:

The matrix $\overline{\mathbf{C}}$ is invertible, (4.2)

then the vector with pressure DoF's $\widetilde{\mathbf{P}}$ exists and is unique (and equal to $\overline{\mathbf{C}}^{-1}\overline{\mathbf{B}}\overline{\mathbf{A}}^{-1}\mathbf{F}$). Therefore, there will not be spurious pressure modes if (4.2) holds true.

Our goal is to evaluate the truth of propositions (4.1) and (4.2). In order to determine the invertibility of matrix $\overline{\mathbf{A}}$, we rely on the fact that, if zero is not an eigenvalue of $\overline{\mathbf{A}}$, then $\overline{\mathbf{A}}$ is invertible. So it suffices to inspect its smallest eigenvalue α_h as the meshes get refined. The result is in Fig. 10, which shows the smallest eigenvalue α_h as a function of the discretization length h for three pairs: the $\mathbf{OFE}_1/\mathrm{OFE}_0$, the $\mathbf{P}_2/P_1$, and the $\mathbf{P}_1/P_0$ pairs. We recall that in the $\mathbf{P}_1/P_0$ pair, the solution $\left(\mathbf{u}^h, p^h\right)$ belongs to the $\mathbf{P}_1 \times P_0$ space, i.e., $U^h = P_1$ (the space of piecewise linear or "4-node elements"), whereas $Q^h = P_0$, i.e., the pressure is constant within each cell, which leads to a piecewise constant approximation for p^h on $\overline{\Omega}$. This pair in known to be unstable [1,2,16]. We see in Fig. 10 that the smallest eigenvalues α_h are all positive, which allows us to conclude that these three pairs yield matrices $\overline{\mathbf{A}}$ that are invertible, i.e., (4.1) is true for the pairs under consideration.

Before we examine the smallest eigenvalues of matrix $\overline{\mathbf{C}}$, we first determine the dimension of its kernel (or null space). The idea is to use the fact that $\overline{\mathbf{C}}$ is invertible if and only if $\overline{\mathbf{C}}$ has a trivial kernel (i.e., *ker* $\overline{\mathbf{C}} = \{\mathbf{0}\}$). Moreover, $\overline{\mathbf{C}}$ has a trivial kernel if and only if its dimension is 0 (i.e., *dim ker* $\overline{\mathbf{C}} = 0$); otherwise, *dim ker* $\overline{\mathbf{C}} > 0$. Fig. 11 shows the dimension of *ker* $\overline{\mathbf{C}}$ as the meshes get refined. We see that for the $\mathbf{OFE}_1/\mathrm{OFE}_0$ and $\mathbf{P}_2/P_1$ pairs, *dim ker* $\overline{\mathbf{C}} = 0$ for all h, which allows us to conclude that these two pairs yield matrices $\overline{\mathbf{C}}$ that

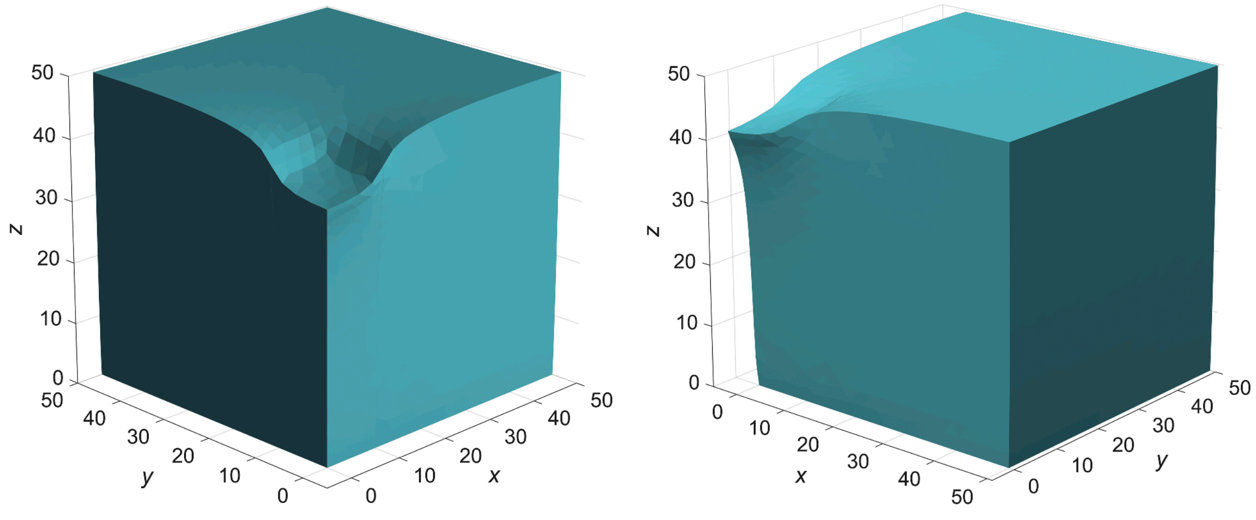

(a) *(b)*

Fig. 6. The deformed solid. A scale factor of 1000 has been applied to the displacement field in order to produce the figures. *(a)* Solution provided by the $\mathbf{OFE}_1/\mathrm{OFE}_0$ pair. *(b)* In order to gain some appreciation for the new geometry of the solid, we rotate the figure about the z-axis, in order to see the protruded portion just below the area where the pressure is applied.

are invertible. However, in what concerns the $\mathbf{P}_1/P_0$ pair, the dimension of *ker* $\overline{\mathbf{C}}$ not only is larger than zero, but increases significantly as the meshes get refined. Therefore, the $\mathbf{P}_1/P_0$ pair yields matrices $\overline{\mathbf{C}}$ that are not invertible. (This is one of the aspects of the instability of this pair alluded to in the previous paragraph.) Finally, we calculate the smallest eigenvalue γ_h of matrix $\overline{\mathbf{C}}$ as a function of h, for the $\mathbf{OFE}_1/\mathrm{OFE}_0$ and $\mathbf{P}_2/P_1$ pairs, see Fig. 12. These eigenvalues γ_h are all positive, which once more attests the invertibility of $\overline{\mathbf{C}}$. So (4.2) is true for the $\mathbf{OFE}_1/\mathrm{OFE}_0$ and $\mathbf{P}_2/P_1$ pairs, and false for the $\mathbf{P}_1/P_0$ pair.

As a conclusion, we notice the similarity between the newly-proposed $\mathbf{OFE}_1/\mathrm{OFE}_0$ pair and the traditional $\mathbf{P}_2/P_1$ (Taylor-Hood) pair, as far as solvability is concerned.

4.3. Bandwidth

Consider the linear system (3.22), rewritten below for convenience:

Find the DoF vectors $\widetilde{\mathbf{U}}$ and $\widetilde{\mathbf{P}}$ such that

$$\underbrace{\begin{bmatrix} \overline{\mathbf{A}} & \overline{\mathbf{B}}^T \\ \mathbf{B} & \end{bmatrix}}_{\overline{\mathbf{K}}} \underbrace{\begin{bmatrix} \widetilde{\mathbf{U}} \\ \widetilde{\mathbf{P}} \end{bmatrix}}_{\mathbf{w}} = \begin{bmatrix} \mathbf{F} \\ \mathbf{0} \end{bmatrix}. \tag{4.3}$$

When the DoF's are ordered within the solution vector $\mathbf{w}$, if the pressure DoF's (collected into the vector $\widetilde{\mathbf{P}}$) are listed after the displacement DoF's (collected into the vector $\widetilde{\mathbf{U}}$), we obtain the linear system above, whose matrix $\overline{\mathbf{K}}$ has the standard saddle-point form. Our goal in this section is to estimate the half-bandwidth $m_{\overline{\mathbf{K}}}$ of the sparse matrix $\overline{\mathbf{K}}$. We assume a different ordering though, with the purpose of making the DoF's packed around the main diagonal as tightly as possible. As a result, the matrix $\overline{\mathbf{K}}$ will no longer have the form in (4.3), since the pressure DoF's will be "intermingled" with the displacement DoF's, as will be shown below. In the remaining of this Section, as well as in Section 4.4, we perform the counting of DoF's in system (4.3) *before* the imposition of the homogeneous boundary conditions (i.e., before removing the zero DoF's from the problem). The half-bandwidth $m_{\overline{\mathbf{K}}}$ is defined in the following way: given any row i in matrix $\overline{\mathbf{K}}$, the entries K_{ij} are zero for $j > i + m_{\overline{\mathbf{K}}}$, see [1,2].

4.3.1. The $\mathbf{OFE}_1/OFE_0$ discretization

Let us consider a general linear elasticity problem posed on a cubic domain $\overline{\Omega} = [0, L] \times [0, L] \times [0, L]$, similar to the one solved in Section 4.1. The domain $\overline{\Omega}$ is again subdivided equally into $k \times k \times k$ little cubes, as in Section 4.2. Of course, the size of each little cube is given by $l = L/k$. The nodes are distributed using a rectangular arrangement of $(k+1) \times (k+1) \times (k+1)$ nodes, i.e., the nodes are ascribed to the vertices of the little cubes. The nodes are ordered as in Fig. 13 (which shows the global indices of some nodes), first along the x, then along the z, and finally along the y directions. Thereafter, each little cube is subdivided into six tetrahedral cells as shown in Fig. 13 (which illustrates the case for $k = 4$). The $\mathbf{OFE}_1/\mathrm{OFE}_0$ discretization uses only the nodes located at the vertices of each tetrahedral cell. It is not difficult to see that the four nodes associated with the cell highlighted in red in Fig. 13 (we can see just two

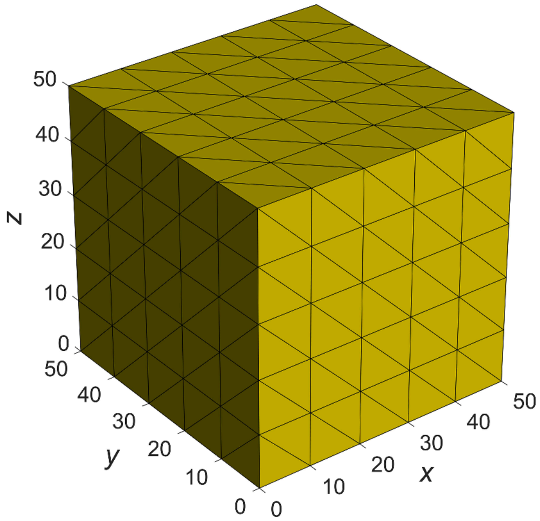

Fig. 7. One of the uniform meshes (corresponding to $k = 5$ subdivisions along each direction) used in the investigation into the solvability of the method.

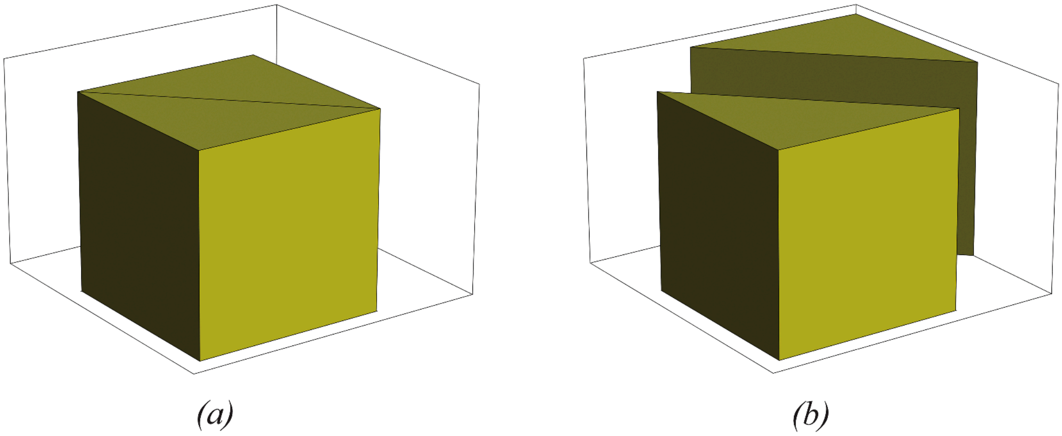

Fig. 8. *(a)* One of the little cubes in Fig. 7 (there are $5 \times 5 \times 5 = 125$ of them there), which has been divided into two parts. *(b)* They are sliced in half along the diagonal line in the top face (of course, they are not actually sliced; the explosive view is shown here for the purposes of illustrating the division process of the little cube into tetrahedral cells).

facets of it) have the global indices and coordinates given in Table 1 below.

In the discretization of the displacement field $\mathbf{u}^h = \left[u_1^h, u_2^h, u_3^h\right]^T$ and of the pressure p^h via the $\mathbf{OFE}_1/\mathrm{OFE}_0$ pair, we use the following ordering of DoF's: For any given node I, we list first the four DoF's associated with component u_1^h, followed by the next four DoF's associated with component u_2^h, then the four DoF's associated with component u_3^h, and finally the single DoF used in the expansion of p^h. As expected, this amounts to 13 DoF's per node. The DoF's in the testing functions $\mathbf{v}^h = \left[v_1^h, v_2^h, v_3^h\right]^T$ and q^h are organized likewise. The half-bandwidth can be calculated as [1,2]:

1. *Find the smallest and the largest global indices of the nodes in the cell marked in red in Fig. 13.* The node with the smallest global index is $I_{\min} = 1$, and the node with the largest global index is $I_{\max} = (k+1)^2 + 1$, see Table 1.

2. *Find the global index of the first DoF associated with node $I_{\min}$.* Since this is the first node in the mesh, it is clear that the global index of the first DoF associated with $I_{\min}$ is 1:

$$\text{First DoF } (I_{\min}) = 1.$$

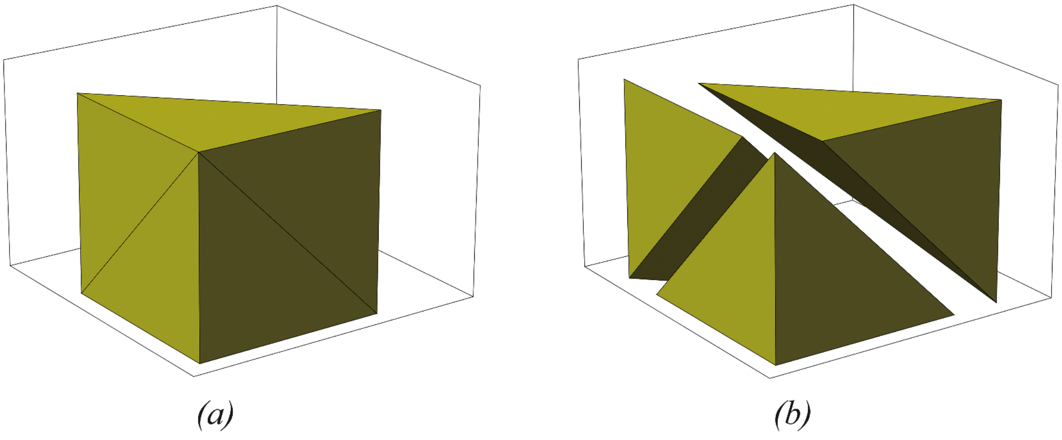

Fig. 9. *(a)* One of the solids obtained after slicing the little cube (the solid close to the reader in Fig. 8*b*). It is now going to be subdivided into three tetrahedra, along the lines shown in the figure. *(b)* Explosive view revealing the resulting three tetrahedral cells. The same process is applied to the other solid in Fig. 8*b* (the solid away from the reader). In the end, each little cube yields six tetrahedral cells.

3. *Find the global index of the last DoF associated with node* $I_{\max}$. There are $I_{\max}-1=\left[(k+1)^2+1\right]-1=(k+1)^2$ nodes listed before $I_{\max}$ in the mesh, and each one of them carries 13 DoF's, see above. Moreover, there are 13 more DoF's associated with the node in question, i.e., to $I_{\max}$. Hence, the global index of the last DoF associated with $I_{\max}$ is given by:

$$\text{Last DoF } (I_{\max}) = 13(k+1)^2+13 = 13\left[(k+1)^2+1\right].$$

4. *The half-bandwidth* $m_{\overline{\mathrm{K}}}$ *is given by the difference between the numbers calculated in steps 3 and 2*:

$$m_{\overline{\mathrm{K}}} = \left[13(k+1)^2+13\right]-1 = 13(k+1)^2+12.$$

When k (the number of cells per direction) is very large, the half-bandwidth for the $\mathbf{OFE}_1/\mathrm{OFE}_0$ pair becomes:

$$m_{\overline{\mathrm{K}}} = 13\left(k^2+2k+1\right)+12 \simeq 13k^2. \tag{4.4}$$

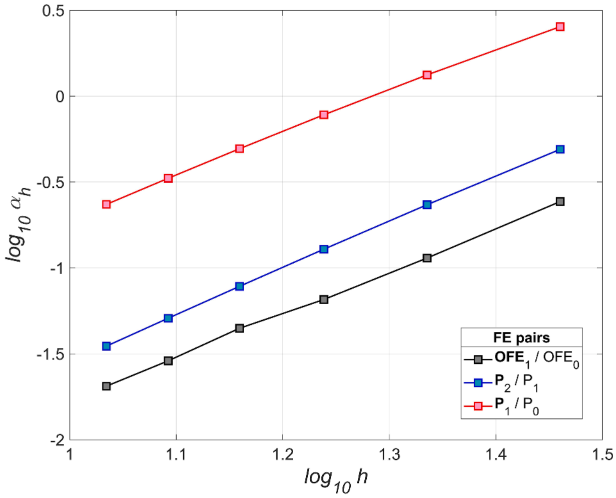

Fig. 10. The smallest eigenvalue α_h of the matrix $\overline{\mathbf{A}}$ in problem (3.22), calculated as a function of the discretization length h. The sequence of meshes is the same for each FE pair.

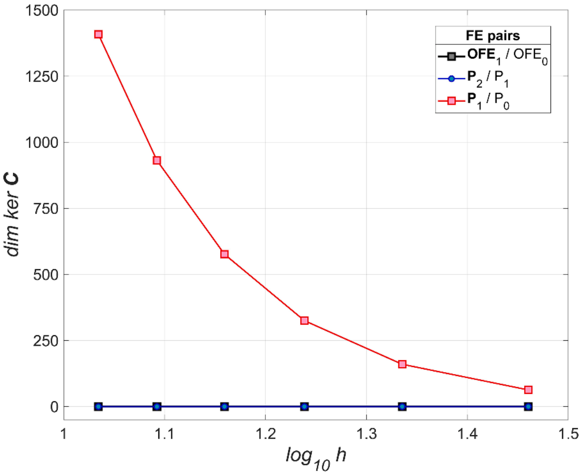

Fig. 11. The dimension of *ker* $\overline{\mathbf{C}}$ as a function of the discretization length h. The matrix $\overline{\mathbf{C}}$ has a trivial kernel when the $\mathbf{OFE}_1/\mathrm{OFE}_0$ and $\mathbf{P}_2/P_1$ pairs are used, and therefore it is invertible. On the other hand, when the $\mathbf{P}_1/P_0$ pair is used, the kernel of $\overline{\mathbf{C}}$ is not trivial; its dimension is given by the number of linearly independent vectors in a basis for *ker* $\overline{\mathbf{C}}$. In this way, the $\mathbf{P}_1/P_0$ pair leads to a matrix $\overline{\mathbf{C}}$ that is not invertible, and so there is no guarantee that the vector of pressure DoF's $\widetilde{\mathbf{P}}$ will be unique. The occurrence of spurious pressure modes is thus not ruled out (for this pair).

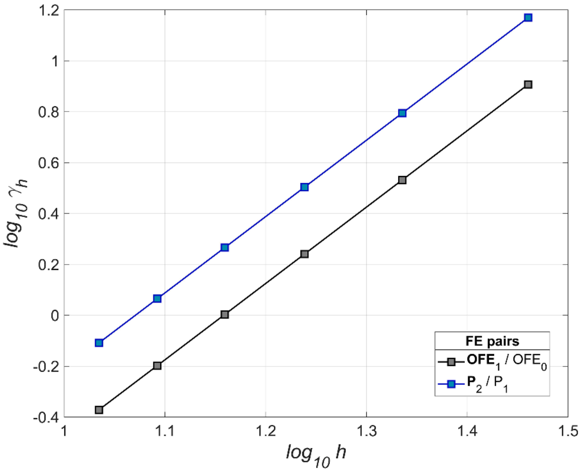

Fig. 12. The smallest eigenvalue γ_h of the matrix $\overline{\mathbf{C}}$, calculated as a function of the discretization length h.

4.3.2. *The* $\mathbf{P}_2/P_1$ *discretization (Taylor-Hood)*

The components of $\mathbf{u}^h$ (and $\mathbf{v}^h$) are now discretized by the traditional 10-node tetrahedral elements (piecewise quadratic, or $\mathbf{P}_2$ Lagrange elements), whereas p^h (and q^h) are discretized by the traditional 4-node elements (piecewise linear, or P_1 Lagrange elements) [1,2].

Since we will be comparing the bandwidths of the $\mathbf{OFE}_1/\mathrm{OFE}_0$ and $\mathbf{P}_2/P_1$ discretizations, we must use the same mesh as that in Fig. 13. The cubic domain $\overline{\Omega} = [0, L] \times [0, L] \times [0, L]$ is again subdivided equally into $k \times k \times k$ little cubes. The difference is that, for each little cube, in addition to the nodes at the vertices (there are 8 of them), we also ascribe extra nodes to the midpoints of the edges (there are 12 of them), to the center of the faces (there are 6 of them), and 1 more node to the little cube's very center. This produces a little cube with 27 associated nodes. We subdivide each 27-node little cube into 6 tetrahedral cells using the same process described in Section 4.2, see Fig. 14. It is straightforward to see that each resulting tetrahedral cell will have nodes at its 4 vertices, in addition to nodes located at the midpoints of all edges (there are 6 of them), thus resulting in a 10-node tetrahedral cell. Fig. 14 shows the resulting tetrahedral mesh.

We note that the number of tetrahedral cells along each direction in Fig. 14 is the same as in Fig. 13 (i.e., k cells), as required. We order the nodes as before (i.e., first along the x, then along the z, and finally along the y directions). The global indices and coordinates of the nodes in the highlighted cell in Fig. 14 (the same one marked in red in Fig. 13) are given in Table 2 (please recall that the size of each little cube is given by $l = L/k$, see Section 4.3.1).

In regard to the ordering of DoF's in the displacement field $\mathbf{u}^h = \left[u_1^h, u_2^h, u_3^h\right]^T$ and in the pressure p^h, we proceed as follows: For any given node I in Fig. 14, we list the (single) DoF corresponding to the component u_1^h, followed by the (single) DoF corresponding to the component u_2^h, and the (single) DoF corresponding to the component u_3^h. Moreover, if node I is located at the vertex of a cell (i.e., it is not at the midpoint of an edge), in addition to the 3 DoF's referred to above used in the expansion of $\mathbf{u}^h$, we list the extra DoF used in the expansion of p^h. So some nodes in Fig. 14 carry 3 DoF's (those at the edge midpoints), whereas the others will carry 4 DoF's (those at the cell vertices). Of course, the DoF's in the testing functions $\mathbf{v}^h = \left[v_1^h, v_2^h, v_3^h\right]^T$ and q^h are ordered likewise. The half-bandwidth is calculated as before:

1. *Find the smallest and the largest global indices of the nodes in the cell marked in red in Fig. 14*. The node with the smallest global index is $I_{\text{min}} = 1$, and the node with the largest global index is $I_{\text{max}} = 2(2k+1)^2 + 1$, see Table 2.
2. *Find the global index of the first DoF associated with node I_{min}*. Since this is the first node, it is clear that:

   $$\text{First DoF } (I_{\text{min}}) = 1.$$

3. *Find the global index of the last DoF associated with node I_{max}*. There are $I_{\text{max}} - 1 = \left[2(2k+1)^2 + 1\right] - 1 = 2(2k+1)^2$ nodes listed before I_{max} in the mesh, and each one of them carries 3 DoF's used in the expansion of $\mathbf{u}^h$, see above. Moreover, given this list of nodes before I_{max}, there are $(k+1)^2$ of them that are located at cell vertices (these are all listed between nodes 1 and 81, since none of the nodes whose indices vary from 82 to 162 is located at a cell vertex, see Fig. 14). Each one of these $(k+1)^2$ nodes has one more DoF used in the expansion of p^h. Finally, node I_{max} itself, being located at a vertex, contributes with 4 more DoF's, and hence the global index corresponding to the last DoF associated with node I_{max} is given by:

   $$\text{Last DoF } (I_{\text{max}}) = 3\left[2(2k+1)^2\right] + (k+1)^2 + 4 = 6(2k+1)^2 + (k+1)^2 + 4.$$

4. *The half-bandwidth $m_{\overline{K}}$ is given by the difference between the numbers calculated in steps 3 and 2*:

   $$m_{\overline{K}} = \left[6(2k+1)^2 + (k+1)^2 + 4\right] - 1 = 6(2k+1)^2 + (k+1)^2 + 3.$$

When k (the number of cells per direction) is very large, the half-bandwidth for the $\mathbf{P}_2/P_1$ pair becomes:

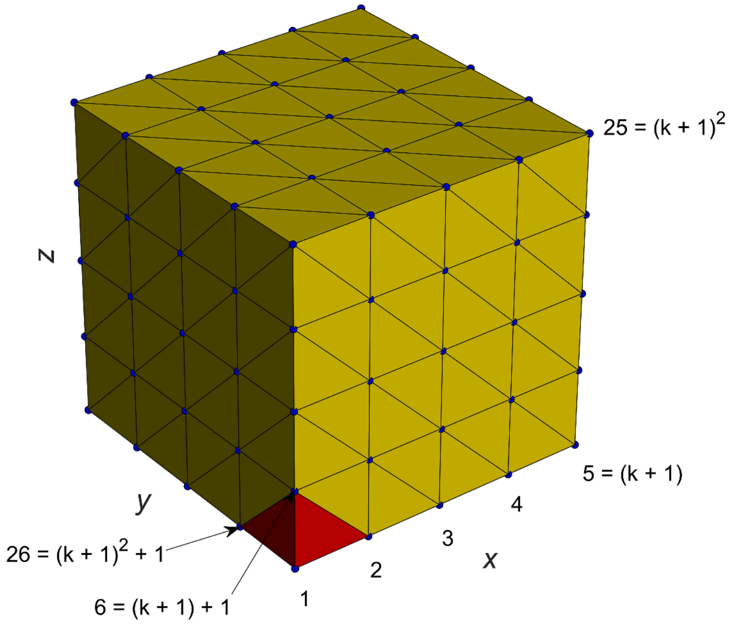

Fig. 13. A uniform mesh set up on a cubic domain Ω. The sides of the cube are subdivided into k cells; here we use $k = 4$, for the purpose of illustration. The nodes are ordered first along the x direction; then along the z direction, and finally along the y direction. Some representative global indices are indicated in the figure (we give both the general formula in terms of k and the specific values when $k = 4$). We are interested in the global indices of the 4 nodes ascribed to the vertices of the tetrahedral cell marked in red. In the $\mathbf{OFE}_1/\text{OFE}_0$ discretization, each node carries 4 DoF's per Cartesian component of $\mathbf{u}^h$ (and of $\mathbf{v}^h$), and one DoF for the expansion of p^h (and of q^h).

Table 1
Nodes and indices for the highlighted cell in Fig. 13.

Node (global indices)	Coordinates in $\mathbb{R}^3$
1	$[0, 0, 0]^T$
2	$[l, 0, 0]^T$
$6 \ = (k+1)+1$	$[0, 0, l]^T$
$26 \ = (k+1)^2+1$	$[0, l, 0]^T$

$$m_{\overline{\mathrm{K}}} = 6\left(4k^2+4k+1\right) + \left(k^2+2k+1\right) + 3 \simeq 25k^2, \tag{4.5}$$

which is approximately twice that for the $\mathbf{OFE}_1/\mathrm{OFE}_0$ pair, see (4.4). In other words, the half-bandwidth in the $\mathbf{OFE}_1$ $/\mathrm{OFE}_0$ discretization (given by $13k^2$, according to (4.4)) is (approximately) half of that in the $\mathbf{P}_2/P_1$ discretization (given by $25k^2$, according to (4.5)).

4.3.3. *Predicted computational effort*

To obtain an idea of how the $\mathbf{OFE}_1/\mathrm{OFE}_0$ and $\mathbf{P}_2/P_1$ elements will perform computationally, we next compare the number of equations n (i.e., the number of DoF's, or the number of rows in $\overline{\mathrm{K}}$) and the half-bandwidths $m_{\overline{\mathrm{K}}}$ for the general problem described in Sections 4.3.1 and 4.3.2. We assume that the same mesh is used for both elements (since as shown below about the same accuracy in solutions is then obtained). We continue to use the uniform meshes in Fig. 13 (for the $\mathbf{OFE}_1/\mathrm{OFE}_0$ pair) and in Fig. 14 (for the $\mathbf{P}_2$ $/P_1$ pair).

The required storage is proportional to $nm_{\overline{\mathrm{K}}}$, i.e., **Stor** $= \nu n m_{\overline{\mathrm{K}}}$ (where ν is a constant), and a measure of the number of operations required for the solution of the linear system (4.3) is $nm_{\overline{\mathrm{K}}}^2/2$, i.e., **NumOp** $= nm_{\overline{\mathrm{K}}}^2/2$, see [1,2]. We want to estimate how n and $m_{\overline{\mathrm{K}}}$ vary with k (the number of subdivisions, or equivalently, the number of tetrahedral cells along each direction of the cubic domain Ω). For large k, $m_{\overline{\mathrm{K}}} \simeq 13k^2$ for the $\mathbf{OFE}_1/\mathrm{OFE}_0$ and $m_{\overline{\mathrm{K}}} \simeq 25k^2$ for the $\mathbf{P}_2/P_1$ pair, according to (4.4) and (4.5), respectively. So we now have to estimate how the number of DoF's n depends on k.

In the arrangement of nodes from Fig. 13, there are $(k+1)^3$ nodes (located at the vertices of the tetrahedral cells), and the $\mathbf{OFE}_1/\mathrm{OFE}_0$ pair requires 13 DoF's per node, see Section 4.3.1. Therefore, for the $\mathbf{OFE}_1/\mathrm{OFE}_0$ pair,

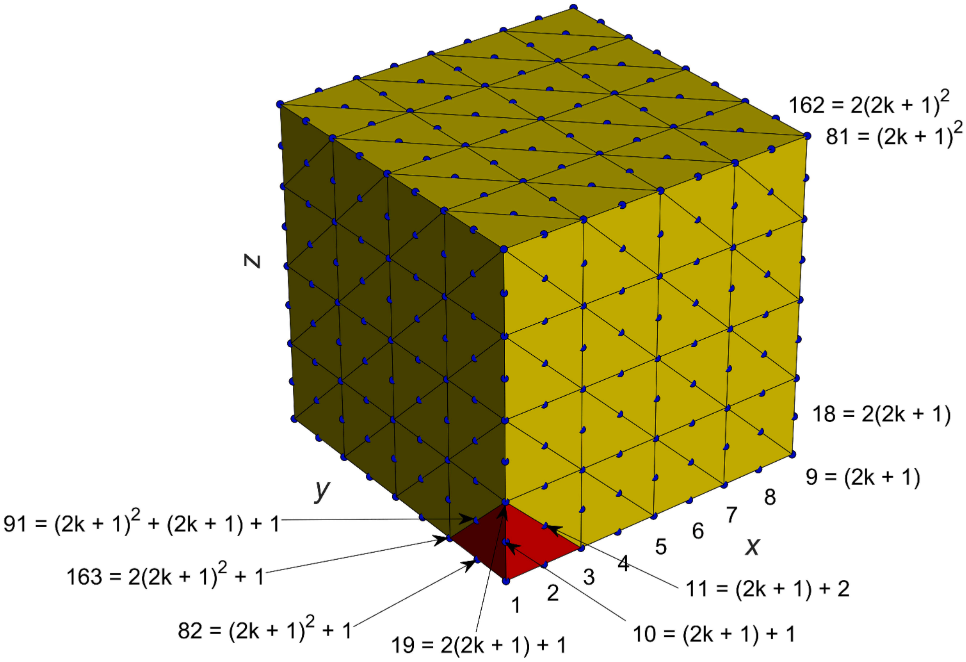

Fig. 14. The same cube as that in Fig. 13, whose sides are again subdivided into k cells. We use here $k = 4$, for the purpose of illustration. In addition to the nodes at the vertices of the tetrahedral cells, extra nodes are ascribed to the midpoints of the cell edges. Representative global indices of some nodes are indicated in the figure (we give both the general formula in terms of k and the specific values when $k = 4$). We are interested in the global indices of the 10 nodes associated with the cell marked in red (the same one as that in Fig. 13). In the $\mathbf{P}_2/P_1$ discretization, each node carries 1 DoF per Cartesian component of $\mathbf{u}^h$ (and of $\mathbf{v}^h$), and the nodes located at the cell vertices carry one extra DoF for the expansion of p^h (and of q^h).

Table 2
Nodes and indices for the highlighted cell in Fig. 14.

Node (global indices)	Coordinates in $\mathbb{R}^3$
1	$[0,0,0]^T$
2	$\left[\frac{l}{2},0,0\right]^T$
3	$[l,0,0]^T$
$10 = (2k+1)+1$	$\left[0,0,\frac{l}{2}\right]^T$
$11 = (2k+1)+2$	$\left[\frac{l}{2},0,\frac{l}{2}\right]^T$
$19 = 2(2k+1)+1$	$[0,0,l]^T$
$82 = (2k+1)^2+1$	$\left[0,\frac{l}{2},0\right]^T$
$83^* = (2k+1)^2+2$	$\left[\frac{l}{2},\frac{l}{2},0\right]^T$
$91 = (2k+1)^2+(2k+1)+1$	$\left[0,\frac{l}{2},\frac{l}{2}\right]^T$
$163 = 2(2k+1)^2+1$	$[0,l,0]^T$

*Not shown in Fig. 14.

$$n = 13(k+1)^3 \simeq 13k^3, \tag{4.6}$$

when k is large. In the arrangement of Fig. 14, there is a total of $(2k+1)^3$ nodes (located both at the vertices and at the midpoints of the edges in the tetrahedral cells). Each one of these nodes carries 3 DoF's, because in the $\mathbf{P}_2$ element, each node carries 1 DoF per Cartesian component of $\mathbf{u}^h$ (and of $\mathbf{v}^h$). Among these $(2k+1)^3$ nodes, there are $(k+1)^3$ nodes (those located at the vertices of the cells), which carry one more DoF for the expansion of p^h (and of q^h), see Section 4.3.2. Therefore, for the $\mathbf{P}_2/P_1$ pair,

$$n = 3(2k+1)^3 + (k+1)^3 \simeq 24k^3 + k^3 = 25k^3, \tag{4.7}$$

when k is large. These results show that the $\mathbf{OFE}_1/\mathrm{OFE}_0$ pair leads to a smaller bandwidth $m_{\overline{\mathbf{K}}}$ and also to a smaller number of DoF's n than the $\mathbf{P}_2/P_1$ pair, when the same mesh is used in both cases. Indeed, the ratio of the number of DoF's n calculated by both methods allows us to establish the theoretical limit:

$$\frac{n|_{\mathbf{OFE}_1/\mathrm{OFE}_0}}{n|_{\mathbf{P}_2/P_1}} \simeq \frac{13k^3}{25k^3} = \frac{13}{25} = 0.52,$$

i.e., as the problem becomes larger, we can expect the $\mathbf{OFE}_1/\mathrm{OFE}_0$ pair to use half the number of DoF's required by the $\mathbf{P}_2\,/P_1$ pair. In regard to the storage $\mathbf{Stor} = \nu n m_{\overline{\mathbf{K}}}$ [1,2], we obtain the limit:

$$\frac{\mathbf{Stor}|_{\mathbf{OFE}_1/\mathrm{OFE}_0}}{\mathbf{Stor}|_{\mathbf{P}_2/P_1}} \simeq \frac{13k^3\cdot 13k^2}{25k^3\cdot 25k^2} = \frac{169k^5}{625k^5} \simeq 0.27,$$

using (4.4) - (4.7), i.e., as the problem becomes larger, the $\mathbf{OFE}_1/\mathrm{OFE}_0$ pair requires approximately only one fourth (25%) of the storage required by the $\mathbf{P}_2/P_1$ pair. Finally, in regard to the number of operations estimated for the solution of the linear system $\mathbf{NumOp} = n m_{\overline{\mathbf{K}}}^2/2$ [1,2], we obtain the limit:

$$\frac{\mathbf{NumOp}|_{\mathbf{OFE}_1/\mathrm{OFE}_0}}{\mathbf{NumOp}|_{\mathbf{P}_2/P_1}} \simeq \frac{13k^3\cdot\left(13k^2\cdot 13k^2\right)}{25k^3\cdot\left(25k^2\cdot 25k^2\right)} = \frac{2197k^7}{15{,}625k^7} \simeq 0.14,$$

again using (4.4) - (4.7), i.e., as the problem becomes larger, the $\mathbf{OFE}_1/\mathrm{OFE}_0$ pair requires approximately only 14% of the operations required by the $\mathbf{P}_2/P_1$ pair to solve the linear system (4.3).

When we consider the results of Section 4.1 (to be complemented by others in the next sections) which demonstrate that the solutions provided by both pairs have the same accuracy when the same mesh is used (the solutions are virtually on top of each other, see Figs. 5g and 5h), we are led to conclude that the $\mathbf{OFE}_1/\mathrm{OFE}_0$ pair is able to perform as well as the $\mathbf{P}_2/P_1$ pair, but using just a fraction of the resources. This of course has a positive impact on the scalability properties of our $\mathbf{OFE}_1/\mathrm{OFE}_0$ pair, i.e., on its ability to tackle large 3D problems.

4.4. Economy of DoF's

There are at least two remarkable properties of the overlapping finite elements that make them into a promising tool in finite element analysis. The first, which has been alluded to in the Introduction and will be explored further in Section 6, is the insensitivity to mesh distortions [30,36]. The second feature, which is particularly relevant in three-dimensional incompressible analyses, is the relatively small number of DoF's required by the OFE method when compared with the traditional finite elements. In principle, this may seem counterintuitive because, in order to approximate scalar functions, the OFE method uses many DoF's per node (due to the local enrichment basis functions, see Section 3.2), whereas the traditional FEM uses a single DoF per node. We will continue the task begun in Section 4.3.3 of counting the DoF's required by the $\mathbf{OFE}_1/\mathrm{OFE}_0$ pair and compare the result with the number of DoF's required by other pairs of traditional finite elements. Of course, we will consider only some usual pairs of finite elements that satisfy the inf-sup condition (see Section 5) and that require less DoF's (i.e., the lowest-order, or 'cheapest' pairs in FEM). We once more assume that, for a given partition $\mathscr{T}_h$ of the domain $\overline{\Omega}$ into tetrahedral cells, the nodes in $\mathscr{T}_h$ are numbered from 1 to N, the cells in $\mathscr{T}_h$ are numbered from 1 to E, and the edges in $\mathscr{T}_h$ are numbered from 1 to L.

4.4.1. Uniform meshes

Let us again subdivide the cubic domain $\overline{\Omega} = [0, L] \times [0, L] \times [0, L]$ equally into $k \times k \times k$ little cubes. Each little cube is subdivided into six tetrahedra, see Figs. 7,13 and 14. The number of nodes, cells, and edges in such a mesh is given by:

$$\begin{aligned} N &= (k+1)^3, \\ E &= 6k^3, \\ L &= (2k+1)^3 - (k+1)^3. \end{aligned} \tag{4.8}$$

The total number n of DoF's required by each pair are as follows:

1. The $\mathbf{OFE}_1/\mathrm{OFE}_0$ pair:
   Displacement vector: 4 DoF's per node for each Cartesian component of the displacement, which amounts to $12N$ DoF's.
   Pressure: 1 DoF per node, which amounts to N DoF's.
   Total: $13N = 13(k+1)^3$, after (4.8).

2. The $\mathbf{P}_1^{bubble}/P_1$ pair or MINI element [1,2,16]:
   Displacement vector: 1 DoF per node for each Cartesian component of the displacement, plus 1 DoF per cell for each Cartesian component, which amounts to $3N + 3E$ DoF's.
   Pressure: 1 DoF per node, which amounts to N DoF's.
   Total: $4N + 3E = 4(k+1)^3 + 3(6k^3) = 4(k+1)^3 + 18k^3$.

3. The $\mathbf{P}_2/P_0$ pair (or 10/1 tetrahedral element) [1,2]:
   Displacement vector: 1 DoF per node for each Cartesian component of the displacement, plus 1 DoF per edge for each Cartesian component, which amounts to $3N + 3L$ DoF's.
   Pressure: 1 DoF per cell, which amounts to E DoF's.
   Total: $(3N + 3L) + E = 3(k+1)^3 + 3\left[(2k+1)^3 - (k+1)^3\right] + 6k^3 = 3(2k+1)^3 + 6k^3$.

4. The $\mathbf{P}_2/P_1$ pair (or 10/4 tetrahedral element, or Taylor-Hood element) [1,2]:
   Displacement vector: 1 DoF per node for each Cartesian component of the displacement, plus 1 DoF per edge for each Cartesian component, which amounts to $3N + 3L$ DoF's.
   Pressure: 1 DoF per node, which amounts to N DoF's.
   Total: $4N + 3L = 4(k+1)^3 + 3\left[(2k+1)^3 - (k+1)^3\right] = 3(2k+1)^3 + (k+1)^3$.

Using the data obtained above, we can now compare the total number n of DoF's required by the other pairs in relation to the $\mathbf{OFE}_1/\mathrm{OFE}_0$ pair as k becomes larger, i.e., we calculate the theoretical limits:

$$\frac{n|_{\mathbf{OFE}_1/\mathrm{OFE}_0}}{n|_{\mathbf{P}_1^{bubble}/P_1}} = \frac{13(k+1)^3}{4(k+1)^3 + 18k^3} \simeq \frac{13k^3}{22k^3} = \frac{13}{22} \simeq 0.59,$$

$$\frac{n|_{\mathbf{OFE}_1/\mathrm{OFE}_0}}{n|_{\mathbf{P}_2/P_0}} = \frac{13(k+1)^3}{3(2k+1)^3 + 6k^3} \simeq \frac{13k^3}{30k^3} = \frac{13}{30} \simeq 0.43,$$

$$\frac{n|_{\mathbf{OFE}_1/\mathrm{OFE}_0}}{n|_{\mathbf{P}_2/P_1}} = \frac{13(k+1)^3}{3(2k+1)^3 + (k+1)^3} \simeq \frac{13k^3}{25k^3} = \frac{13}{25} = 0.52.$$

These results allow us to conclude that, as the discretization gets finer (or equivalently, as the problems become larger), the $\mathbf{OFE}_1/\mathrm{OFE}_0$ pair leads to the smallest number of DoF's (and hence, to smaller systems of linear algebraic equations to be solved).

Observation: We decided not to invest any effort in the $\mathbf{OFE}_1/P_0$ pair, which uses the OFE basis functions to approximate the displacement field and constant basis functions (ascribed to each cell) to approximate the pressure, as we did in [36] for two-dimensional problems. In the scenario described above, both the $\mathbf{OFE}_1/\mathrm{OFE}_0$ and $\mathbf{OFE}_1/P_0$ pairs require $12N = 12(k+1)^3$ DoF's to approximate the displacement field, see (4.8). However, the $\mathbf{OFE}_1/\mathrm{OFE}_0$ pair requires $N = (k+1)^3 \simeq k^3$ (when k gets large) DoF's to provide a *continuous* approximation for the pressure (1 DoF per node), whereas the $\mathbf{OFE}_1/P_0$ pair would require $E = 6k^3$ DoF's to provide a *discontinuous* approximation for the pressure (1 DoF per cell). So, if we were to use the $\mathbf{OFE}_1/P_0$ pair, we would spend more resources in order to get a worse solution (since the pressure calculated by constant basis functions is piecewise-constant, i.e., it has the 'staircase' appearance, see [36]).

4.4.2. Non-uniform meshes

We now set up a sequence of six non-uniform meshes (with increasing levels of refinement) on our cubic domain $\overline{\Omega} = [0,L] \times [0,L] \times [0,L]$, in the particular case for $L = 50$, see Fig. 15. Next, we list the number of DoF's required by each finite element pair, using the items 1 through 4 from Section 4.4.1 (for example, for the $\mathbf{OFE}_1/\mathrm{OFE}_0$ pair, the number of DoF's required to approximate the displacement field, or $\mathbf{u}$-DoF's, is given by $12N$; so for mesh #1 with $N = 78$, we get 936 DoF's, and so on). Note that mesh #5 is the same one as that used in Section 4.1, see Fig. 4. We organize the data in Table 3, and Fig. 16 is a pictorial representation of the total number of DoF's required by different pairs, as the refinement level of the mesh increases. The $\mathbf{OFE}_1/\mathrm{OFE}_0$ pair is, by far, the one which requires the smallest number of DoF's. It requires even less DoF's than the MINI element. This is remarkable because, even though it uses less DoF's, the results provided by the $\mathbf{OFE}_1/\mathrm{OFE}_0$ pair – characterized by *linear* enrichment functions in the local bases, see Section 3.5.1 – have a precision comparable to that provided by the *quadratic* basis functions from the $\mathbf{P}_2/P_1$ element when the same mesh is used, see Figs. 5g and 5h. (This feature will become evident in other examples and figures from the next sections.) In Fig. 17, we plot the ratio between the total number of DoF's required by the $\mathbf{OFE}_1/\mathrm{OFE}_0$ and $\mathbf{P}_2/P_1$ pairs as the meshes get refined. It can be verified that, even for a sequence of non-uniform meshes, the ratio approaches the theoretical limit of 0.52, calculated in Section 4.4.1. (Indeed, the ratio is 0.56 for mesh #6.)

We can observe from Table 3 that, in three dimensions, as the non-uniform meshes get refined, the number of cells and the number of edges increase significantly more than the number of nodes. Hence it is bad practice to ascribe DoF's to cells and/or edges in three-

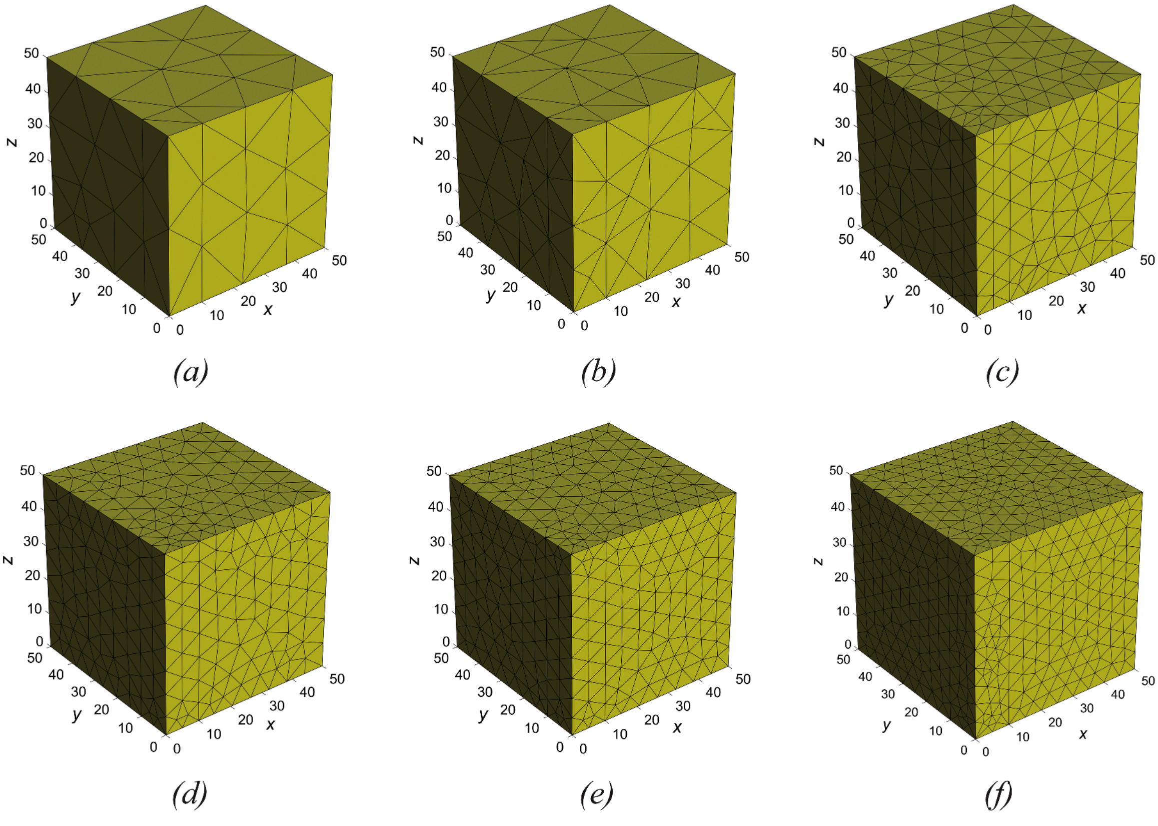

(a) (b) (c)

(d) (e) (f)

Fig. 15. A sequence of six non-uniform meshes, whose parameters (number of nodes, cells, and edges) are given in Table 3. *(a)* Mesh #1. *(b)* Mesh #2. *(c)* Mesh #3. *(d)* Mesh #4. *(e)* Mesh #5. *(f)* Mesh #6. According to Table 3, the number of cells and the number of edges increase significantly more than the number of nodes as the meshes get refined.

Table 3
Number of DoF's for different meshes.

	Nodes	Cells	Edges	Element	**u**-DoF's	*p*-DoF's	Total DoF's
Mesh #1	78	210	353	$\mathbf{OFE}_1/\mathrm{OFE}_0$	936	78	1014
				MINI	864	78	942
				$\mathbf{P}_2/P_0$	1293	210	1503
				$\mathbf{P}_2/P_1$	1293	78	1371
Mesh #2	206	798	1105	$\mathbf{OFE}_1/\mathrm{OFE}_0$	2472	206	2678
				MINI	3012	206	3218
				$\mathbf{P}_2/P_0$	3933	798	4731
				$\mathbf{P}_2/P_1$	3933	206	4139
Mesh #3	629	2671	3621	$\mathbf{OFE}_1/\mathrm{OFE}_0$	7548	629	8177
				MINI	9900	629	10,529
				$\mathbf{P}_2/P_0$	12,750	2671	15,421
				$\mathbf{P}_2/P_1$	12,750	629	13,379
Mesh #4	1069	4946	6450	$\mathbf{OFE}_1/\mathrm{OFE}_0$	12,828	1069	13,897
				MINI	18,045	1069	19,114
				$\mathbf{P}_2/P_0$	22,557	4946	27,503
				$\mathbf{P}_2/P_1$	22,557	1069	23,626
Mesh #5	1545	7483	9555	$\mathbf{OFE}_1/\mathrm{OFE}_0$	18,540	1545	20,085
				MINI	27,084	1545	28,629
				$\mathbf{P}_2/P_0$	33,300	7483	40,783
				$\mathbf{P}_2/P_1$	33,300	1545	34,845
Mesh #6	3164	16,295	20,267	$\mathbf{OFE}_1/\mathrm{OFE}_0$	37,968	3164	41,132
				MINI	58,377	3164	61,541
				$\mathbf{P}_2/P_0$	70,293	16,295	86,588
				$\mathbf{P}_2/P_1$	70,293	3164	73,457

dimensional problems. At this point we can see the advantage of the purely nodal OFE spaces which, despite using many DoF's at a single node (in order to account for the local enrichment basis functions), in the end, they still lead to a smaller number of DoF's than the other traditional FEM spaces (that use DoF's ascribed to cells and/or edges, associated with bubble functions and/or quadratic functions).

5. STABILITY

This section is concerned with the very important topic regarding the inf-sup stability of our discretization scheme. We will show that the $\mathbf{OFE}_1/\mathrm{OFE}_0$ pair satisfies the inf-sup condition, which effectively rules out the possibility of *locking* effects, see [1,2]. We continue to use the geometry of the cubic block $\overline{\Omega} = [0, L] \times [0, L] \times [0, L]$ as a model, for $L = 50$.

The Babuska-Brezzi theory of mixed formulations asserts that the *discrete* problem (3.16) is well-posed (its solution exists, is unique, and depends continuously on the data) if the two following *inf-sup conditions* are satisfied [8,15,16]: Given two finite-dimensional subspaces $\mathbf{U}^h \subset \mathbf{H}^1_{0,\Gamma_D}(\Omega)$ and $Q^h \subset L^2(\Omega)$,

$$\underset{\mathbf{v}^h \in K^h \setminus \{\mathbf{0}\}}{inf} \quad \underset{\mathbf{w}^h \in K^h \setminus \{\mathbf{0}\}}{sup} \quad \frac{a\left(\mathbf{v}^h, \mathbf{w}^h\right)}{\|\mathbf{v}^h\|_{1,\Omega} \quad \|\mathbf{w}^h\|_{1,\Omega}} =: \alpha_h > 0, \tag{5.1}$$

$$\underset{q^h \in Q^h \setminus \{\mathbf{0}\}}{inf} \quad \underset{\mathbf{v}^h \in \mathbf{U}^h \setminus \{\mathbf{0}\}}{sup} \quad \frac{b\left(\mathbf{v}^h, q^h\right)}{\|\mathbf{v}^h\|_{1,\Omega} \quad \|q^h\|_{0,\Omega}} =: \beta_h > 0, \tag{5.2}$$

where the subscript 'h' in the quantities α_h and β_h indicates that in principle they depend on the partition $\mathscr{T}_h$. The bilinear forms a and b are those in (2.11). When studying the stability of the $\mathbf{OFE}_1/\mathrm{OFE}_0$ pair, we shall make $\mathbf{U}^h := \mathbf{OFE}_1$ and $Q^h := \mathrm{OFE}_0$, whereas when studying the stability of the $\mathbf{P}_2/P_1$ pair (for comparison purposes), we make $\mathbf{U}^h := \mathbf{P}_2$ and $Q^h := P_1$.

For any function $\mathbf{v} \in \mathbf{H}^1(\Omega)$ and for any function $q \in L^2(\Omega)$, the standard norm in the space $\mathbf{H}^1(\Omega)$ is given as:

$$\| \mathbf{v}\|_{1,\Omega} := \left(\|\mathbf{v}\|^2_{0,\Omega} + \|\nabla\mathbf{v}\|^2_{0,\Omega}\right)^{1/2}, \tag{5.3}$$

whereas the scalar, vector, and matrix norms in $L^2(\Omega)$ are defined as:

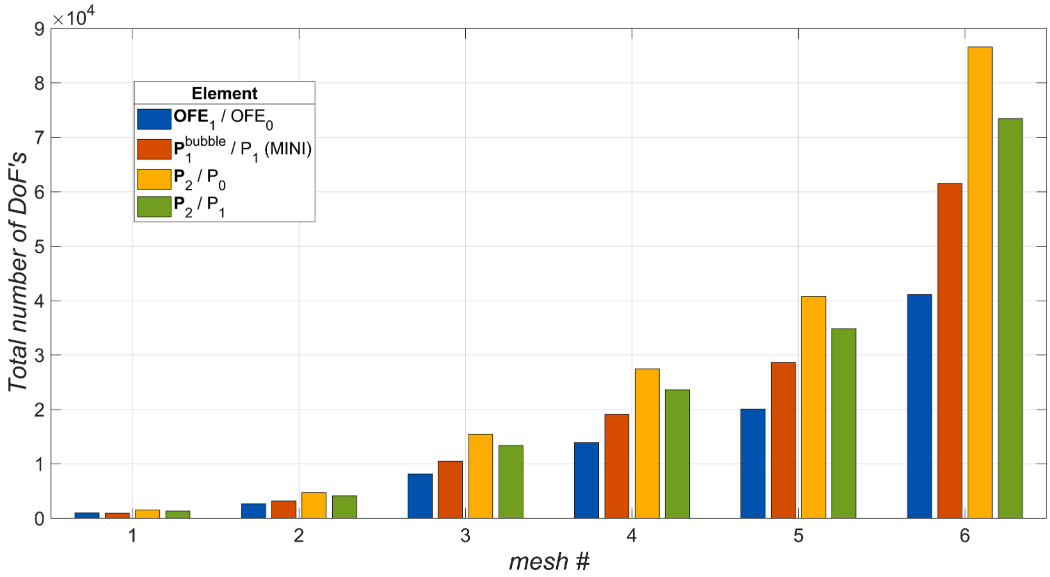

Fig. 16. The total number of DoF's required by each element, according to the last column of Table 3. Blue bars: $\mathbf{OFE}_1/\mathrm{OFE}_0$ element. Red bars: MINI element. Yellow bars: $\mathbf{P}_2/P_0$ element. Green bars: $\mathbf{P}_2/P_1$ element. The first cluster of four bars represents the values relative to mesh #1, the second cluster to mesh #2, and so on (see Fig. 15 and Table 3).

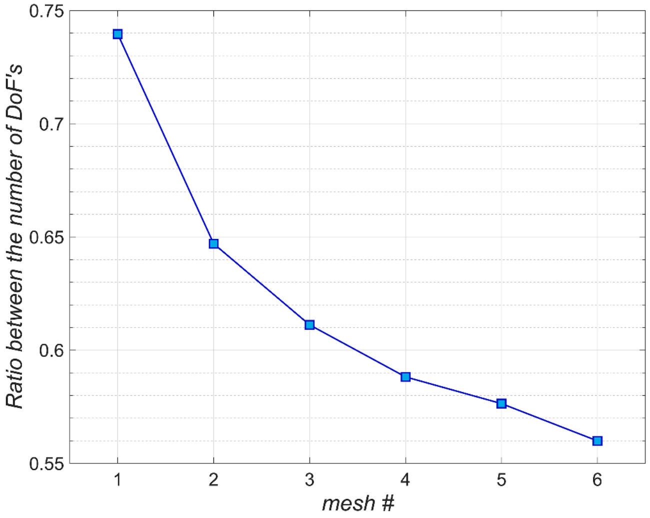

Fig. 17. The ratio between the total number of DoF's required by the $\mathbf{OFE}_1/\mathrm{OFE}_0$ and $\mathbf{P}_2/P_1$ pairs, as the meshes get refined. Even for non-uniform meshes, the ratio approaches the theoretical value of 0.52 (calculated for uniform meshes in Section 4.4.1).

$$
\begin{aligned}
||q||_{0,\Omega} &:= \left(\int_\Omega |q|^2 d\Omega\right)^{1/2}, \\
||\mathbf{v}||_{0,\Omega} &:= \left(\int_\Omega \mathbf{v}\cdot\mathbf{v} d\Omega\right)^{1/2}, \\
||\nabla\mathbf{v}||_{0,\Omega} &:= \left(\int_\Omega \nabla\mathbf{v} : \nabla\mathbf{v} d\Omega\right)^{1/2},
\end{aligned}
\tag{5.4}
$$

respectively. The subspace K^h in (5.1) is the (discrete) *kernel* of the bilinear form b, given by:

$$K^h := \left\{\mathbf{v}^h \in \mathbf{U}^h \;\middle|\; b\left(\mathbf{v}^h, q^h\right) = 0,\ \text{for any } q^h \in Q^h\right\}. \tag{5.5}$$

The inf-sup conditions (5.1) and (5.2) are difficult to prove directly. The fundamental ingredient for tackling (5.1) is Korn's inequality, stated as: there is a positive constant C (which depends on Ω and Γ_D) such that, for any $\mathbf{v} \in \mathbf{H}^1_{0,\Gamma_D}(\Omega)$,

$$\|\mathbf{v}\|_{1,\Omega} \leq C \|\bar{\bar{\epsilon}}(\mathbf{v})\|_{0,\Omega}, \tag{5.6}$$

where

$$\|\bar{\bar{\epsilon}}(\mathbf{v})\|_{0,\Omega} = \left(\int\limits_{\Omega} \bar{\bar{\epsilon}}(\mathbf{v}) : \bar{\bar{\epsilon}}(\mathbf{v}) d\Omega\right)^{1/2}, \tag{5.7}$$

see [11]. (Here the components of the tensor $\bar{\bar{\epsilon}}(\mathbf{v})$ are given by $v_{(ij)} = \left(v_{i,j} + v_{j,i}\right)/2$, in accordance with Section 2.3.) When we let $\mathbf{v}$ be an arbitrary vector in $\mathbf{H}^1_{0,\Gamma_D}(\Omega)$ and make $\mathbf{w} = \mathbf{v}$ in (2.11) we conclude that:

$$a(\mathbf{v}, \mathbf{v}) = 2\mu \int\limits_{\Omega} \bar{\bar{\epsilon}}(\mathbf{v}) : \bar{\bar{\epsilon}}(\mathbf{v}) d\Omega = 2\mu \|\bar{\bar{\epsilon}}(\mathbf{v})\|^2_{0,\Omega} \geq 2\mu C^{-2} \|\mathbf{v}\|^2_{1,\Omega},$$

after using (5.7) and (5.6). In other words, there is some positive constant α (namely, $\alpha := 2\mu C^{-2}$) such that $a(\mathbf{v}, \mathbf{v}) \geq \alpha \|\mathbf{v}\|^2_{1,\Omega}$, for any $\mathbf{v} \in \mathbf{H}^1_{0,\Gamma_D}(\Omega)$. We have thus established that the bilinear form a is *coercive* (that is, *elliptic*) on the whole of $\mathbf{H}^1_{0,\Gamma_D}(\Omega)$. Of course, since the discrete kernel K^h in (5.5) is such that $K^h \subset \mathbf{U}^h$, and since $\mathbf{U}^h \subset \mathbf{H}^1_{0,\Gamma_D}(\Omega)$ no matter if we take $\mathbf{U}^h := \mathbf{OFE}_1$ or $\mathbf{U}^h := \mathbf{P}_2$ (after incorporating the homogeneous Dirichlet conditions along Γ_D), we are able to see that K^h is ultimately a subspace of $\mathbf{H}^1_{0,\Gamma_D}(\Omega)$. Therefore, it is also the case that $a\left(\mathbf{v}^h, \mathbf{v}^h\right) \geq \alpha \|\mathbf{v}^h\|^2_{1,\Omega}$, for any $\mathbf{v}^h \in K^h$. That is, the bilinear form a is also coercive on K^h. The coercivity of a on the kernel K^h allows us to prove (5.1) [16]. (We have here the stronger scenario in which the constant α is independent of h.)

Unfortunately, the validity of (5.2) cannot be established on purely theoretical grounds as that of (5.1). However, the validity of (5.2) can be established by a numerical procedure [1,2]. Before we proceed, we would like to point out that, thanks to (5.6), we can work with the following condition instead of (5.2):

$$\underset{q^h \in Q^h\setminus\{0\}}{inf} \ \underset{\mathbf{v}^h \in \mathbf{U}^h\setminus\{\mathbf{0}\}}{sup} \ \frac{b\left(\mathbf{v}^h, q^h\right)}{\|\bar{\bar{\epsilon}}(\mathbf{v}^h)\|_{0,\Omega} \ \ \|q^h\|_{0,\Omega}} =: \gamma_h > 0. \tag{5.8}$$

(The seminorm $\mathbf{v} \rightarrow \|\bar{\bar{\epsilon}}(\mathbf{v})\|_{0,\Omega}$ becomes a norm over the space $\mathbf{H}^1_{0,\Gamma_D}(\Omega)$ [11].) After the discretization procedure is complete, we use (3.21), (5.7), and the first expression in (5.4) to rewrite the quantities above as:

$$\begin{aligned} b\left(\mathbf{v}^h, q^h\right) &= \widetilde{\mathbf{Q}}^T \overline{\mathbf{B}} \widetilde{\mathbf{V}}, \\ \|\bar{\bar{\epsilon}}\left(\mathbf{v}^h\right)\|^2_{0,\Omega} &= \widetilde{\mathbf{V}}^T \overline{\mathbf{E}} \widetilde{\mathbf{V}}, \\ \|q^h\|^2_{0,\Omega} &= \widetilde{\mathbf{Q}}^T \overline{\mathbf{Y}} \widetilde{\mathbf{Q}}, \end{aligned} \tag{5.9}$$

where $\overline{\mathbf{B}}$, $\overline{\mathbf{E}}$, and $\overline{\mathbf{Y}}$ are suitable matrices, and $\widetilde{\mathbf{V}}$ and $\widetilde{\mathbf{Q}}$ are the vectors collecting the DoF's in the expansion of $\mathbf{v}^h$ and q^h, respectively. Of course, the matrix $\overline{\mathbf{B}}$ is the same as that in (3.21). Since the elements of the space $\mathbf{U}^h \subset \mathbf{H}^1_{0,\Gamma_D}(\Omega)$ have zero trace along the Dirichlet boundary Γ_D, the displacement DoF's associated with all nodes lying on $\overline{\Gamma}_D$ are constrained to be zero, see Section 3.5.1. In practice, this amounts to removing from matrices $\overline{\mathbf{E}}$ and $\overline{\mathbf{B}}$ the rows and columns associated with these DoF's. Using (5.9), the inf-sup condition (5.8) becomes:

$$\underset{\widetilde{\mathbf{Q}} \in \mathbb{R}^M\setminus\{\mathbf{0}\}}{inf} \ \underset{\widetilde{\mathbf{V}} \in \mathbb{R}^S\setminus\{\mathbf{0}\}}{sup} \ \frac{\widetilde{\mathbf{Q}}^T \overline{\mathbf{B}} \widetilde{\mathbf{V}}}{\sqrt{\widetilde{\mathbf{V}}^T \overline{\mathbf{E}} \widetilde{\mathbf{V}}} \ \sqrt{\widetilde{\mathbf{Q}}^T \overline{\mathbf{Y}} \widetilde{\mathbf{Q}}}} =: \gamma_h > 0. \tag{5.10}$$

In the expression above, M is the dimension of the space Q^h (when $Q^h := \text{OFE}_0$, this number is equal to the number N of nodes in the computational domain, see Section 4.4.1). Of course, S is the dimension of the space $\mathbf{U}^h$ (when $\mathbf{U}^h := \mathbf{OFE}_1$, this number is given by $12N$ minus the number of DoF's constrained to be zero, see Section 4.4.1). We first verify if the kernel of $\overline{\mathbf{B}}^T$ is different from $\{\mathbf{0}\}$, i.e., if $ker\ \overline{\mathbf{B}}^T \neq \{\mathbf{0}\}$ because, if this is the case, then it is straightforward to verify that (5.10) cannot be satisfied. In the simulations performed in this paper, we always obtained $ker\ \overline{\mathbf{B}}^T = \{\mathbf{0}\}$. In this case, the inf-sup value γ_h in (5.10) is given by $\gamma_h = \sqrt{\kappa_{\min}}$, where $\kappa_{\min}$ is the smallest eigenvalue in the problem:

$$\overline{\mathbf{B}}\overline{\mathbf{E}}^{-1}\overline{\mathbf{B}}^T \widetilde{\mathbf{Q}} = \kappa \overline{\mathbf{Y}} \widetilde{\mathbf{Q}}, \tag{5.11}$$

see [1,2,8]. In order to verify condition (5.8) in the problem relative to the incompressible block, we consider a sequence of uniform meshes with decreasing h. Each mesh is constructed by first subdividing the cubic domain $\overline{\Omega}$ equally into $k \times k \times k$ little cubes; each little cube is then subdivided into six tetrahedra, as in Section 4.2. In this study, we assumed a sequence of meshes for which $k = 5,6,\cdots,11$. For each mesh, we solved the eigenproblem (5.11) and retrieved the inf-sup value γ_h as explained above. Fig. 18 shows a plot of the inf-sup values γ_h versus the discretization length h, both for the $\mathbf{OFE}_1/\mathrm{OFE}_0$ and $\mathbf{P}_2/P_1$ pairs. It can be verified that for both pairs and for all values of h under consideration, we have $\gamma_h > 0$.

Ideally, the inf-sup values γ_h should never approach zero, i.e., $\mathit{inf}\ \gamma_h > 0$, where the infimum is taken over all h, no matter how small [16]. However, such a condition is difficult to verify. In practice, we may resort to the inf-sup testing [1,2,10]: we examine the trend of the curve corresponding to the values γ_h; if no strong tendency of decreasing towards zero is observed, then it is unlikely that the values γ_h will actually reach zero. This practical test has been applied to a multitude of problems [3,36], and is able to predict, at least for the specific problem at hand, that there will be no spurious pressure modes and no locking effects (linked to the failure of satisfying (5.8), see [1,2]) as the meshes get refined. The curves in Fig. 18 show that the inf-sup values do not reach a plateau. However, for the sequence of values in this figure, a linear regression shows that $\gamma_h \simeq C_1 h^{0.416}$ for the $\mathbf{OFE}_1/\mathrm{OFE}_0$ pair, and $\gamma_h \simeq C_2 h^{0.500}$ for the $\mathbf{P}_2/P_1$ pair, where C_1 and C_2 are positive constants. Interestingly enough, the actual eigenvalues obtained for both pairs are very close to each other, as revealed by the curves. This is another positive feature of our $\mathbf{OFE}_1/\mathrm{OFE}_0$ pair, since it is a well-known fact in the literature that the Taylor-Hood $\mathbf{P}_2/P_1$ pair does satisfy the inf-sup condition (i.e., condition (5.2) is satisfied with a constant β independent of h) [1,2,16].

6. ERROR ANALYSIS

This section deals with the accuracy of the $\mathbf{OFE}_1/\mathrm{OFE}_0$ solutions. The goal is to compare the precision of the $\mathbf{OFE}_1/\mathrm{OFE}_0$ and $\mathbf{P}_2/P_1$ solutions, particularly when the meshes used in the calculations become distorted. We focus our attention on the problem whose domain Ω is described by a cylinder, with radius r given by $r = 1$ cm $= 0.01$ m and height $H = 10$ cm $= 0.1$ m. Its material properties are specified as $E_Y = 500$ kPa (Young's modulus) and $\rho = 900$ kg/m^3 (density).

We begin by creating a regular mesh over $\overline{\Omega}$ as follows: First, the interval $[0, r]$ along the radial direction is equally divided into k subintervals. Let $h := r/k$ denote the discretization length. This procedure creates the $k+1$ values $r_1 = 0, r_2 = h, r_3 = 2h, \ldots r_{k+1} = kh = r$. Second, reasoning on the plane xy, we place a node at the origin (0,0). Next, for $i = 2,\cdots,k+1$, we consider the circle whose radius is r_i and then place N_i nodes equally distributed along its perimeter, where $N_i := \lceil 2\pi r_i/h \rceil$ and $\lceil\ \cdot\ \rceil$ is the ceiling function (which rounds a number up to the next integer). Finally, we replicate this two-dimensional distribution of nodes equally M times along the z direction, where $M := \lceil H/h \rceil$. The nodal cloud thus obtained is used as a basis for the meshing algorithm, which creates a mesh of tetrahedral cells out of these nodes. Fig. 19 shows an example for $k = 3$ subdivisions.

In order to introduce mesh distortions, after the mesh in Fig. 19 is created, we first define a distortion angle θ_{dist}, and proceed as follows, inspired by an idea taken from the analysis of two-dimensional problems in [41]: For each set of N_i nodes placed along the perimeter of the circle with radius r_i, where $i = 2,\cdots,k+1$, we rotate these N_i nodes along the perimeter of the circle by an angle given by $(-1)^i\theta_{\mathrm{dist}}$. This creates a 'twisting' effect that produces really bad-shaped cells when the distortion angle θ_{dist} is large enough. This pattern of distortion is replicated along the z-axis, from the $z = 0$ plane to the $z = H$ plane. Figs. 20*a* and 20*b* show the cells on the top surface of the cylinder ($z = H$) when $\theta_{\mathrm{dist}} = 0$ and when $\theta_{\mathrm{dist}} = \pi/12$ rad $= 15°$, respectively. In both of these figures, we used $k = 4$ subdivisions. After the 'twisting' of the cells, we obtain a mesh as that in Fig. 19, but clearly contaminated by a large number of low-quality tetrahedral cells, as shown in Fig. 20*c*, which is a magnified view of the top surface of the cylinder in Fig. 19 (after the

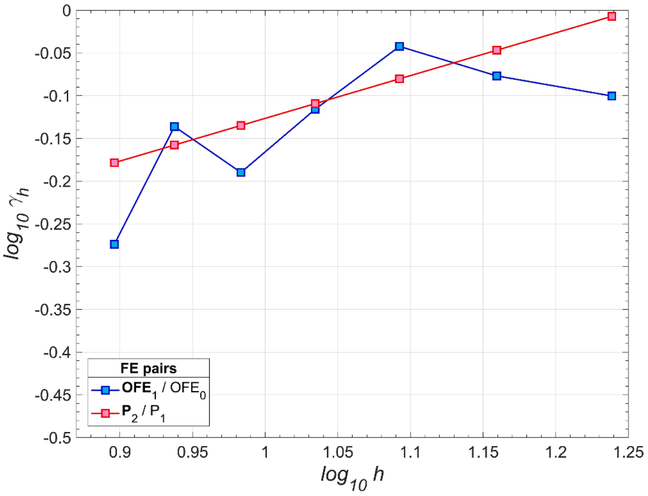

Fig. 18. The inf-sup values γ_h in (5.8) as the meshes get refined. Results for both the $\mathbf{OFE}_1/\mathrm{OFE}_0$ and $\mathbf{P}_2/P_1$ pairs.

distortion has been applied).

6.1. Bending under volumetric forces

The first problem we study is characterized by homogeneous Dirichlet boundary conditions $\mathbf{u} = \mathbf{0}$ on the bottom surface ($z = \mathbf{0}$), and by homogeneous Neumann conditions (zero traction) $\mathbf{g} = \mathbf{0}$ on the lateral and on the top surface ($z = H$) of the cylinder. We assume a body (volumetric) force $\mathbf{b} = [100{,}0{,}0]^T$ m/s^2. Fig. 21*a* shows the undeformed body (before application of the force), and Fig. 21*b* shows the deformed body, in which the displacement field has been calculated using the $\mathbf{OFE}_1/\mathrm{OFE}_0$ pair, on a mesh with $k = 4$ subdivisions and $\theta_{\mathrm{dist}} = 0$. (This mesh has $12{,}480$ cells.) In order to evaluate the influence of mesh distortions on the $\mathbf{OFE}_1/\mathrm{OFE}_0$ solutions, we calculate the x-component of the displacement field u_1^h along the vertical axis of the cylinder, first using the mesh with $\theta_{\mathrm{dist}} = 0$ and then the mesh with $\theta_{\mathrm{dist}} = \pi/12 = 15^\circ$. (Both of these meshes use $k = 4$ subdivisions, and both of course have the same number of cells.) The results, shown in Figs. 22*a* and 22*b*, are compared with a reference solution (computed by the $\mathbf{P}_2/P_1$ pair, on a very refined and undistorted mesh, with almost $300{,}000$ DoF's), and we can observe that a distorted mesh (such as that in Fig. 20*c*) has exerted virtually no influence on the $\mathbf{OFE}_1/\mathrm{OFE}_0$ solutions.

We repeated the calculations using the $\mathbf{P}_2/P_1$ pair on the same meshes as those described above (i.e., with $k = 4$ subdivisions), and arrived at a similar result: The solutions agree very well with the reference, and there is no visible effect of the distorted mesh on the solutions, see Figs. 22*a* and 22*b* However, in order to produce these solutions, the $\mathbf{OFE}_1/\mathrm{OFE}_0$ pair used 35,178 DoF's, whereas the $\mathbf{P}_2/P_1$ pair used $59{,}811$ DoF's (the ratio $35{,}178/59{,}811 \simeq 0.59$ is close to the theoretical limit of 0.52, see Section 4.4.1).

We have thus been able to verify that in this example, when the same meshes are considered, the $\mathbf{OFE}_1/\mathrm{OFE}_0$ pair produces solutions as accurate as those of the $\mathbf{P}_2/P_1$ pair, and with the same degree of insensitivity to mesh distortions, but using less DoF's. The next section will explore this topic further.

6.2. Cylinder under a shear stress

We consider the same geometry and material properties from the previous section, but the body force is now assumed to be zero, i.e., $\mathbf{b} = \mathbf{0}$. In regards to the boundary conditions, homogeneous Dirichlet conditions $\mathbf{u} = \mathbf{0}$ are imposed on the bottom surface ($z = 0$), and homogeneous Neumann conditions $\mathbf{g} = \mathbf{0}$ (zero traction) are imposed on the lateral surface of the cylinder. On the top surface ($z = H$) we impose the condition $\mathbf{g} = [0{,}2000,0]^T$ N/m^2, see (2.3). The traction is thus parallel to the top surface (shearing stress).

Consider a sequence of four meshes, each one characterized by a number of k subdivisions along the radial direction, where $k = 1, \cdots, 4$. The discretization length is defined as $h := r/k$, and the meshes are constructed in accordance with a distortion angle θ_{dist}, see Section 6. We consider a set of four distortion angles, i.e., $\theta_{\mathrm{dist}} \in \{0,\pi/24,\pi/18,\pi/12\} = \{0,7.5^\circ,10^\circ,15^\circ\}$. For each angle θ_{dist} and each h, we compute the discrete solution $(\mathbf{u}^h, p^h)$ using either the $\mathbf{OFE}_1/\mathrm{OFE}_0$ or the $\mathbf{P}_2/P_1$ pair, and calculate the L^2 norms of the errors as:

$$e_{\mathbf{u}}(h) := \frac{\|\mathbf{u}^h - \mathbf{u}_{\mathrm{ref}}\|_{0,\Omega}}{\|\mathbf{u}_{\mathrm{ref}}\|_{0,\Omega}}, \text{ and } e_p(h) := \frac{\|p^h - p_{\mathrm{ref}}\|_{0,\Omega}}{\|p_{\mathrm{ref}}\|_{0,\Omega}}, \tag{6.1}$$

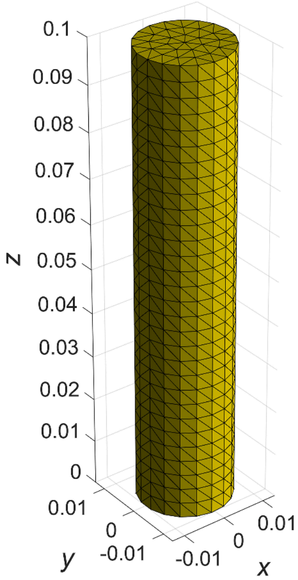

Fig. 19. An undistorted mesh of tetrahedral cells set up over the cylindrical domain $\overline{\Omega}$. Dimension units in meters (m). The distance along the radial direction has been divided into $k = 3$ subintervals, which produces 3 concentric rings.

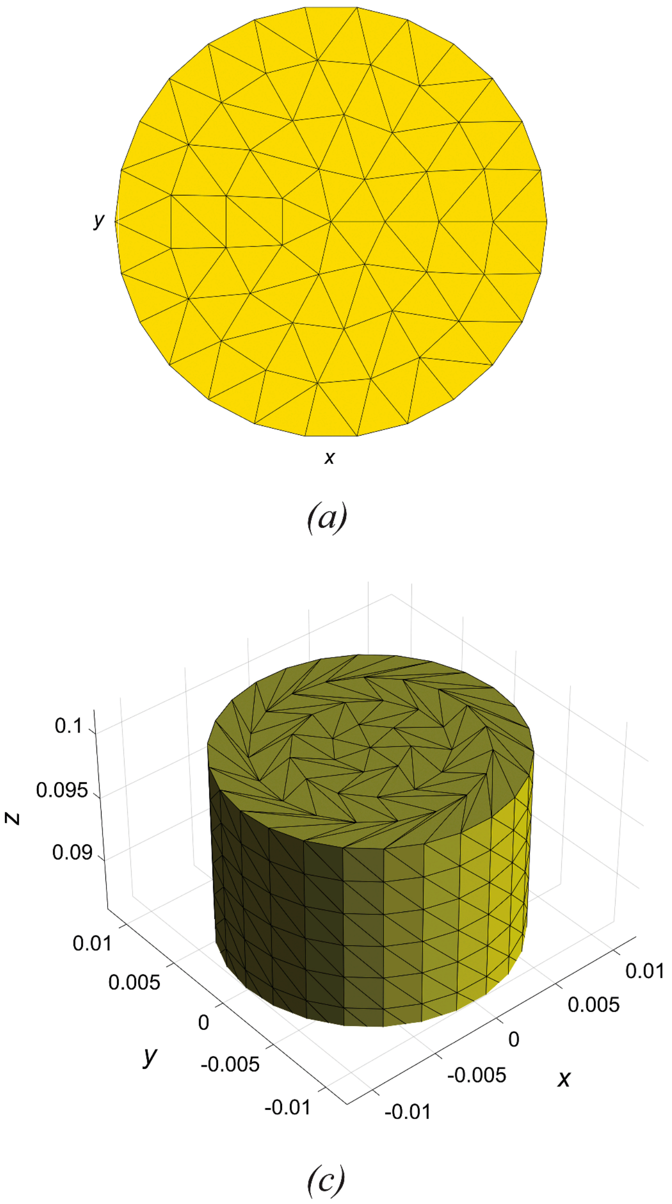

Fig. 20. *(a)* Aerial view of the top surface of the cylinder in Fig. 19. A regular arrangement of cells, obtained when there is no distortion, i.e., when $\theta_{\text{dist}} = 0$. *(b)* The same as before, but considering a distortion angle of $\theta_{\text{dist}} = \pi/12 = 15^\circ$. *(c)* After the 'twisting', we obtain a three-dimensional mesh as that in Fig. 19, but with distorted cells. This figure shows the portion of the domain $\overline{\Omega}$ near the top surface of the cylinder. Dimension units in meters (m).

see (5.4). Of course, $(\mathbf{u}_{\text{ref}}, p_{\text{ref}})$ is the reference solution, calculated on a very refined and undistorted mesh using the $\mathbf{P}_2\,/P_1$ pair (again leading to almost 300,000 DoF's).

Fig. 23*a* shows the deformed body, in which the displacement field has been calculated using the $\mathbf{OFE}_1/\text{OFE}_0$ pair on a mesh with $k = 4$ subdivisions and $\theta_{\text{dist}} = 0$. Figs. 23*b* and 23*c* show the y-component of the displacement field u_2^h along the cylinder axis calculated by both the $\mathbf{OFE}_1/\text{OFE}_0$ and the $\mathbf{P}_2/P_1$ pairs, using this same mesh. (As stated in Section 6.1, this mesh has 12,480 cells.) We observe that the $\mathbf{OFE}_1/\text{OFE}_0$ and the $\mathbf{P}_2/P_1$ solutions are again virtually on top of each other, as in Figs. 22*a* and 22*b*. The number of DoF's required by each pair is the same as in Section 6.1.

Fig. 24*a* shows the displacement error $e_{\mathbf{u}}(h)$ for each distortion angle θ_{dist}. We see that the errors for the $\mathbf{OFE}_1/\text{OFE}_0$ and $\mathbf{P}_2/P_1$ solutions are, for all practical purposes, the same. Fig. 24*a* highlights the immunity to mesh distortions: the solutions keep converging irrespective of the value for θ_{dist}. This is true for both the $\mathbf{OFE}_1/\text{OFE}_0$ and $\mathbf{P}_2/P_1$ solutions. A linear regression applied to these curves allow them to be expressed as $e_{\mathbf{u}}(h) \simeq Ch^{0.7302}$, where C is a suitable constant. The conclusion is that the $\mathbf{OFE}_1/\text{OFE}_0$ and $\mathbf{P}_2\,/P_1$ pairs

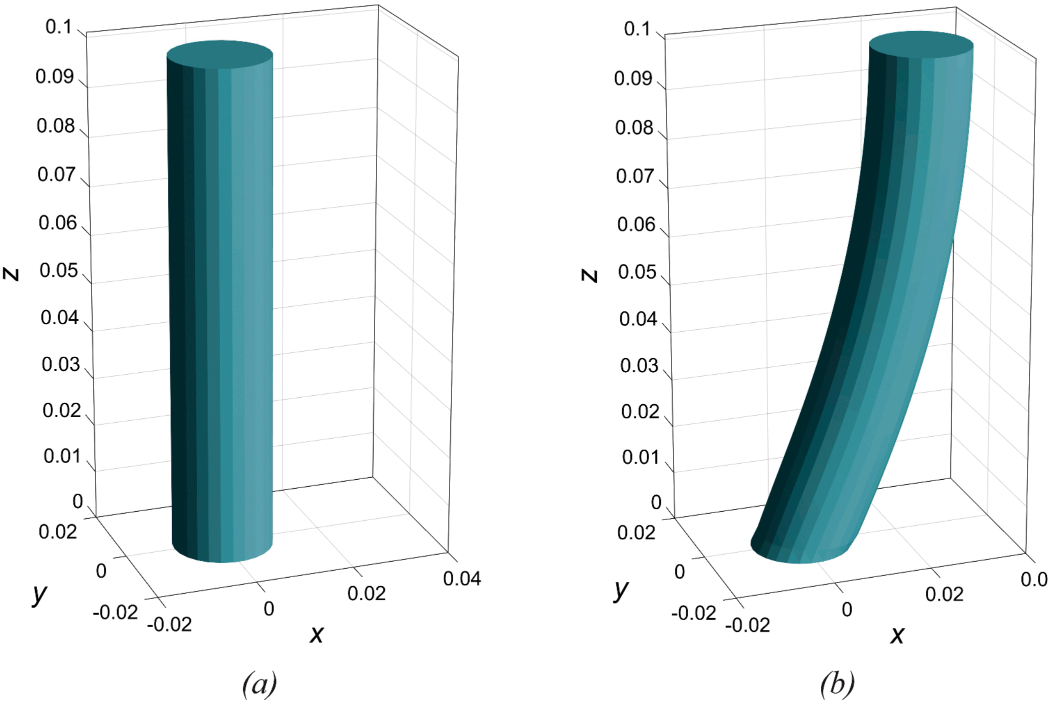

Fig. 21. *(a)* The undeformed cylinder. *(b)* The bending (or deformation) of the cylinder under the action of body forces acting along the positive x-direction. As expected, the cylinder experiences a deformation along this direction. The displacement field is calculated using the $\mathbf{OFE}_1/\mathrm{OFE}_0$ pair on a mesh with $k = 4$ subdivisions and $\theta_{\text{dist}} = 0$, and it is represented here with a scale factor of 25, i.e., the real displacement is 25 times smaller than what is shown. Dimension units in meters (m).

produce accurate displacement solutions; indeed, they both have the same accuracy (as evidenced by the fact that the error curves are literally on top of each other, see Fig. 24*b*), and both present a reasonable insensitivity to mesh distortions.

As for the error in pressure $e_p(h)$, we show in Fig. 24*c* that the error for the $\mathbf{OFE}_1/\mathrm{OFE}_0$ solution is slightly larger than the error for the $\mathbf{P}_2/P_1$ solution, and that convergence is kept up to moderate mesh distortions. However, for very distorted meshes (i.e., when $\theta_{\text{dist}} = \pi/12$), the pressure solutions provided by both pairs stop converging.

These facts reveal that, as far as the overlapping elements are concerned, using degree 1 polynomials in the local bases yields an almost total insensitivity to mesh distortions (see Fig. 24*a*, which shows the error for the displacement field, approximated within the $\mathbf{OFE}_1$ space), whereas the use of degree zero polynomials (approximation within the OFE_0 space) yields only a reasonable insensitivity to mesh distortions.

6.2.1. *Efficiency measure I: number of DoF's*

Since the $\mathbf{OFE}_1/\mathrm{OFE}_0$ and $\mathbf{P}_2/P_1$ displacement solutions have the same accuracy, one can raise the question of which method is to be used. Let it be the error curves $e_{\mathbf{u}}$ when $\theta_{\text{dist}} = 0$, i.e., the black curves in Figs. 24*a* and 24*b* (the continuous trace corresponding to the $\mathbf{OFE}_1/\mathrm{OFE}_0$ and the dashed trace corresponding to the $\mathbf{P}_2/P_1$ solution). For the sequence of four meshes, instead of plotting the error $e_{\mathbf{u}}$ as a function of h, we shall plot it as a function of the number n of DoF's instead. The result is in Fig. 25.

We observe that for the same accuracy, the $\mathbf{P}_2/P_1$ pair requires more DoF's than the $\mathbf{OFE}_1/\mathrm{OFE}_0$ pair. For each mesh, characterized by a number k of subdivisions along the radial direction (see Section 6), Table 4 shows the number n of DoF's required by the $\mathbf{OFE}_1/\mathrm{OFE}_0$ and $\mathbf{P}_2/P_1$ discretizations. The explanation for this fact was given earlier in Sections 4.4.1 and 4.4.2: as the three-dimensional meshes are refined, the number of edges becomes much larger than the number of nodes, which causes the number of DoF's required by the $\mathbf{P}_2$ space to eventually surpass the number required by the $\mathbf{OFE}_1$ space. Therefore, the $\mathbf{OFE}_1/\mathrm{OFE}_0$ pair is to be recommended, since it basically reproduces the performance of the $\mathbf{P}_2/P_1$ pair, but with less DoF's.

6.2.2. *Efficiency measure II: solution time*

Let us consider again the error curves $e_{\mathbf{u}}$ when $\theta_{\text{dist}} = 0$. For each mesh, characterized by the number k of subdivisions along the radial direction (see Section 6), Table 5 shows the time required by the $\mathbf{OFE}_1/\mathrm{OFE}_0$ and $\mathbf{P}_2/P_1$ discretizations to fill in the global finite element matrix $\overline{\mathbf{K}}$ in (4.3). In each case, the corresponding time is normalized with respect to the time taken to fill in the matrix $\overline{\mathbf{K}}$ using the $\mathbf{P}_2/P_1$ discretization when $k = 1$. For the sequence of four meshes, we now plot the error $e_{\mathbf{u}}$ as a function of this normalized time. The result is shown in Fig. 26. (We note that in writing the programs, we have not used the most efficient coding procedures available, i.e., the codes have not been optimized to yield the smallest possible times in each case. Therefore, these figures should be seen as

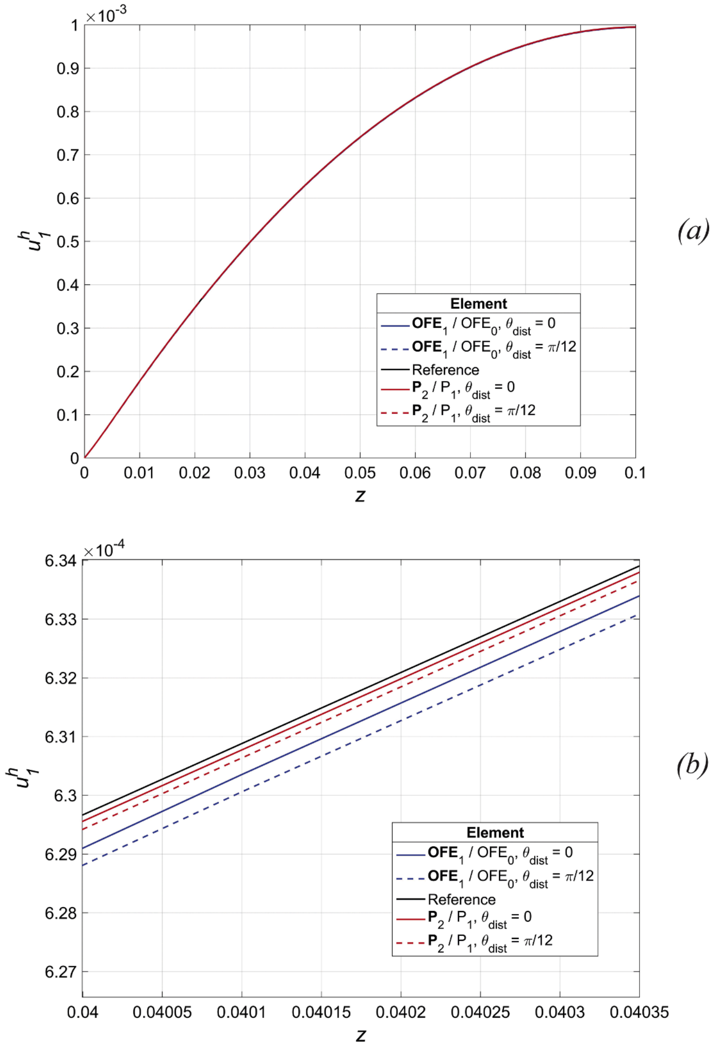

Fig. 22. *(a)* The x-component of the displacement field u_1^h calculated along the axis of the cylinder (line characterized by $x = 0$, $y = 0$, and $0 \leq z \leq H$). We used the $\mathbf{OFE}_1/\mathrm{OFE}_0$ and the $\mathbf{P}_2/P_1$ pairs, with and without mesh distortion. The curves are literally on top of each other, i.e., there is in principle no difference between the results. The mesh distortion showed no influence on the $\mathbf{OFE}_1/\mathrm{OFE}_0$ and $\mathbf{P}_2/P_1$ solutions. *(b)* The solutions are so on top of each other that we need to magnify the view in order to capture the minute differences. Here we see the fine structure of the curves in *(a)*, after significantly magnifying the view around the point $z = 0.04$. Dimension and displacement units in meters (m).

providing a general idea only.)

We apply a linear regression to the curves in Fig. 26, and we find that the relation between the error $e_{\mathbf{u}}$ and the time t is given by $e_{\mathbf{u}}(t) \simeq E_1 t^{-0.2532}$ for the $\mathbf{OFE}_1/\mathrm{OFE}_0$ pair, and $e_{\mathbf{u}}(t) \simeq E_2 t^{-0.2576}$ for the $\mathbf{P}_2/P_1$ pair, where E_1 and E_2 are constants. The two curves are essentially parallel (they have the same slope), which shows that for both methods, the time required to fill in the FE matrix increases in the same proportion. Fig. 26 reveals the obvious fact that, for smaller errors, a greater time is needed to fill in the FE matrix (because it is larger). Moreover, we verify that for the same error, the time required by the $\mathbf{OFE}_1/\mathrm{OFE}_0$ solution to fill in the matrix is greater than that required by the $\mathbf{P}_2/P_1$. This is expected, and the explanation is that in the process of filling in the matrix $\overline{\mathbf{K}}$, we must loop through all cells in the partition $\mathscr{T}_h$.

We saw earlier in Section 3.5.1 that when the displacement field $\mathbf{u}^h$ is discretized using the $\mathbf{OFE}_1$ element, each node requires 4 DoF's per Cartesian component, which leads to a total of 12 DoF's per node. This means that within each tetrahedral cell (determined by 4 nodes), the displacement field $\mathbf{u}^h$ can be calculated using a total of 48 basis functions (together with their corresponding DoF's). The testing function $\mathbf{v}^h$ also requires 48 basis functions (and 48 DoF's); the result is that the local stiffness matrix relative to a given cell has size equal to 48×48. The entries of this local matrix will be mapped later to the global finite element submatrix $\overline{\mathbf{A}}$ in (4.3), as it happens in ordinary finite element programming [1,2]. The same observations apply to the submatrix $\overline{\mathbf{B}}$ in (4.3).

Considering the $\mathbf{P}_2$ element, the displacement field $\mathbf{u}^h$ within a given tetrahedral cell (now determined by 10 nodes; 4 at the vertices

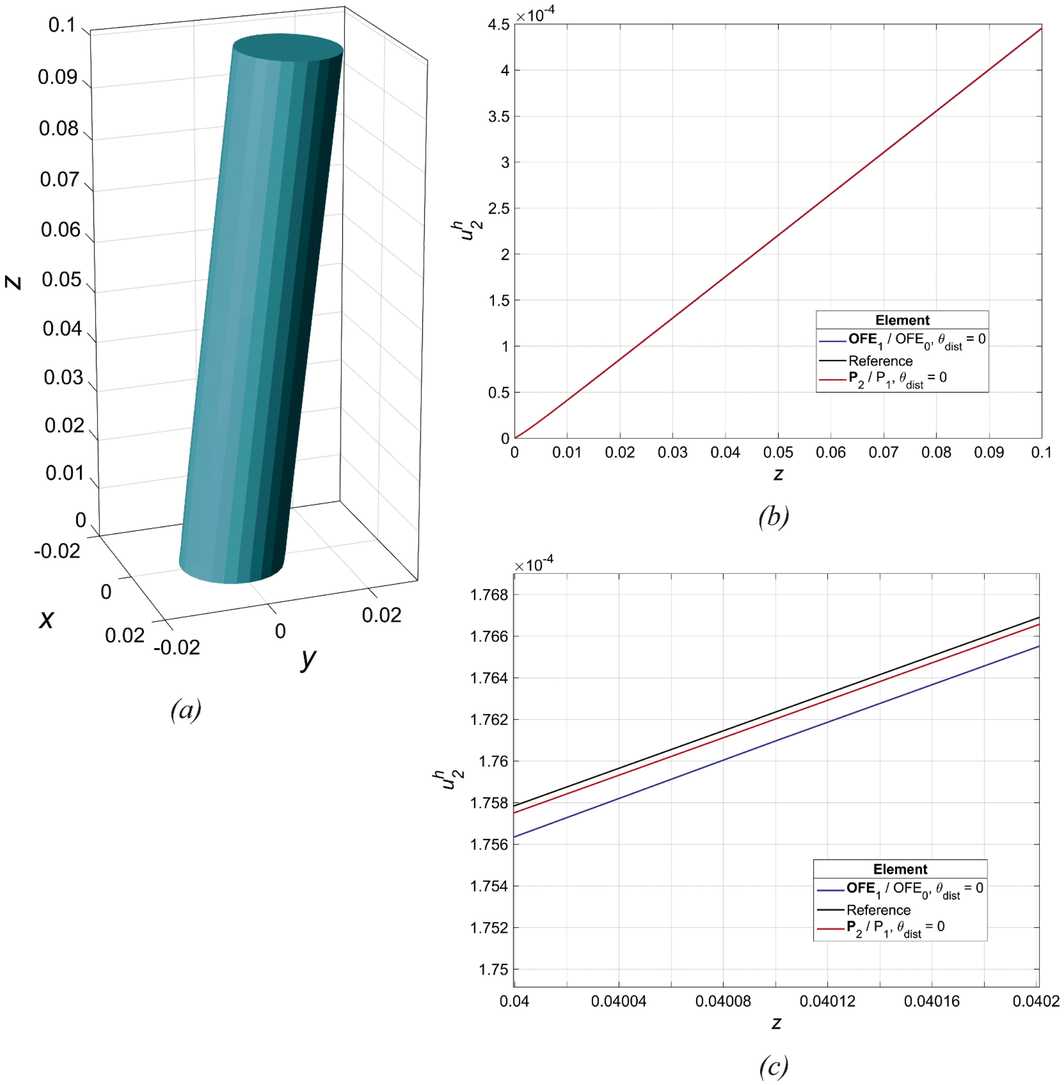

Fig. 23. *(a)* The deformed cylinder under the action of a shear stress acting on its top surface, and directed along the positive y-direction. The undeformed cylinder (reference configuration) is shown in Fig. 21*a*. The displacement field has been calculated using the $\mathbf{OFE}_1/\mathrm{OFE}_0$ pair, on a mesh with $k = 4$ subdivisions and $\theta_{\text{dist}} = 0$. A scale factor of 25 has been used in the illustration of the deformed cylinder. *(b)* The y-component of the displacement field u_2^h calculated along the axis of the cylinder (line characterized by $x = 0, y = 0$, and $0 \leq z \leq H$). We used the $\mathbf{OFE}_1/\mathrm{OFE}_0$ and the $\mathbf{P}_2/P_1$ pairs, with $\theta_{\text{dist}} = 0$. *(c)* The fine structure of the curves in *(b)*, after significantly magnifying the view around the point $z = 0.04$. Dimension and displacement units in meters (m).

and the other 6 at the midpoints of the edges, see Fig. 3) can be calculated using a total of 30 basis functions (together with their corresponding DoF's), since each node requires 1 DoF per Cartesian component, which leads to a total of 3 DoF's per node. The testing function $\mathbf{v}^h$ is calculated likewise, and so the local stiffness matrix relative to a given cell (to be mapped later to the global submatrix $\overline{\mathbf{A}}$ in (4.3)) has size equal to 30×30. This is the reason why the $\mathbf{OFE}_1/\mathrm{OFE}_0$ pair takes more time than the $\mathbf{P}_2/P_1$ pair, when the same mesh is used by both: the local matrices associated with the first are larger than those associated with the latter.

The overall conclusion is this: For the same error, the global finite element matrices $\overline{\mathbf{K}}$ in the $\mathbf{OFE}_1/\mathrm{OFE}_0$ discretization are smaller (because they use less DoF's, see Fig. 25) and have tighter bandwidths than those in the $\mathbf{P}_2/P_1$ discretization (see Sections 4.3.1 and 4.3.2). However, they take a little more time to be filled in (see Fig. 26).

7. An additional example: the ring problem

In this section we shall examine the problem whose domain Ω is illustrated in Fig. 27. The (undeformed) solid is given by the region between two concentric cylinders of radii 0.1 m and 0.2 m (i.e., a ring). The height of both cylinders is 0.1 m. Finally, we remove one fourth of the ring, in order to obtain the geometry in Fig. 27. The cylinders are such that their axes are oriented along the x-direction, whereas their

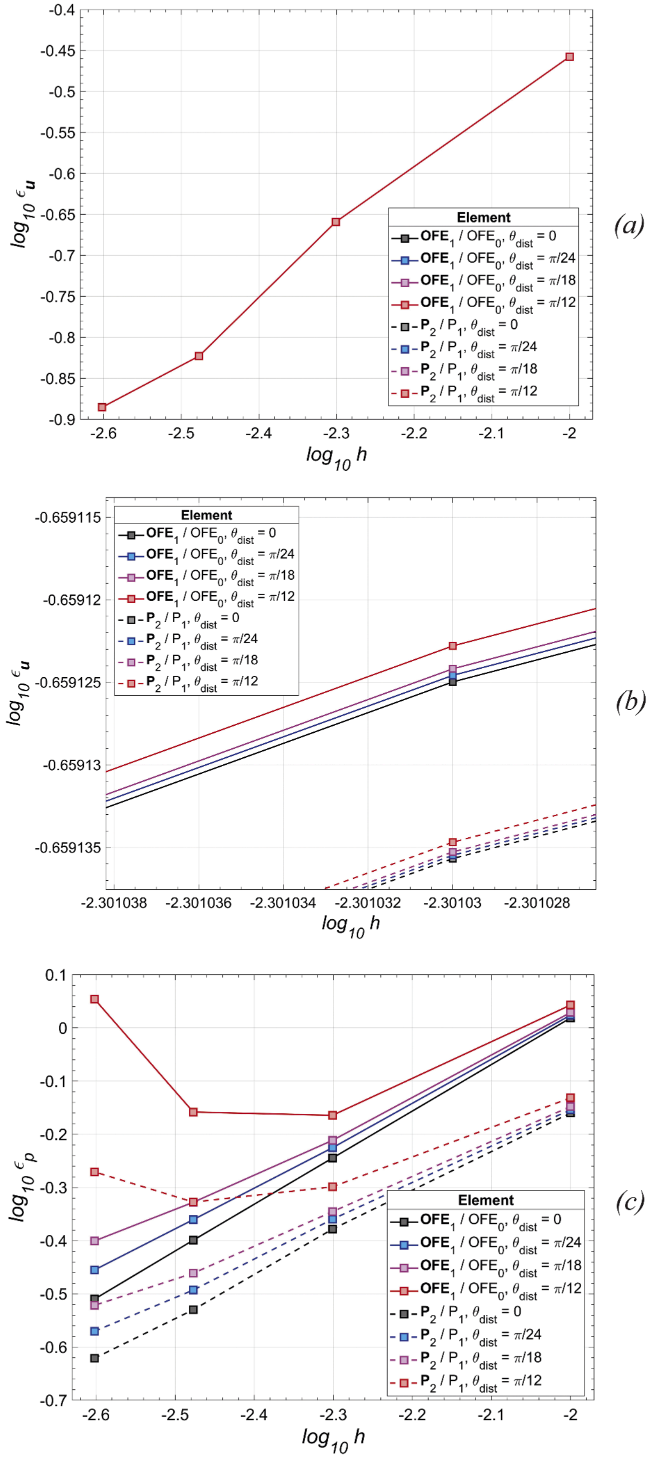

Fig. 24. *(a)* The curves for the displacement error $e_{\mathbf{u}}$ as a function of the discretization length h. Convergence is kept, even when the meshes become distorted. Such a behavior occurs for both the $\mathbf{OFE}_1/\mathrm{OFE}_0$ and $\mathbf{P}_2/P_1$ solutions. *(b)* The error curves for the $\mathbf{OFE}_1/\mathrm{OFE}_0$ and $\mathbf{P}_2\,/P_1$ solutions are almost on top of each other; here we see the fine structure of the error curves after magnifying the view around the point $\log_{10}h\ =-2.3$. *(c)* The curves for the pressure error e_p as a function of the discretization length h.

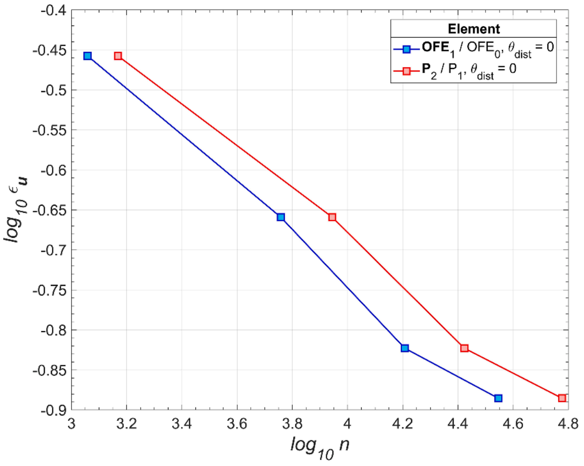

Fig. 25. The curves for the displacement error $e_{\mathbf{u}}$ as a function of the total number of DoF's n.

Table 4
Number of DoF's required by each pair.

Subdivisions	$\mathbf{OFE}_1/\mathrm{OFE}_0$	$\mathbf{P}_2/P_1$
$k=1$	1144	1474
$k=2$	5733	8805
$k=3$	16,120	26,494
$k=4$	35,178	59,811

Table 5
Normalized time t required by each pair to fill in the global finite element matrix.

Subdivisions	$\mathbf{OFE}_1/\mathrm{OFE}_0$	$\mathbf{P}_2/P_1$
$k=1$	3.9775	1.0000
$k=2$	27.5998	6.4504
$k=3$	92.9084	21.5323
$k=4$	216.4587	51.0995

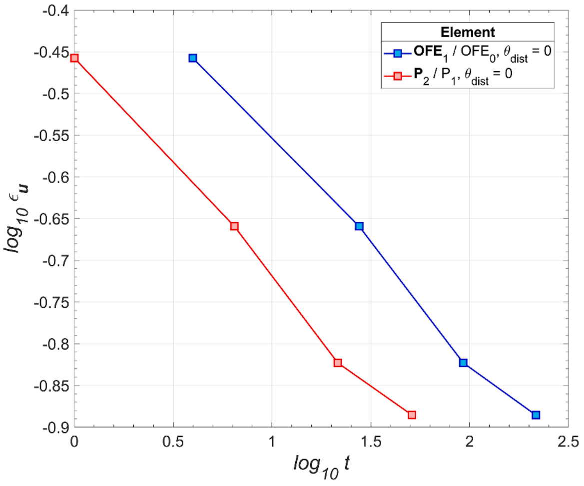

Fig. 26. The curves for the displacement error $e_{\mathbf{u}}$ as a function of the (normalized) time t required to fill in the finite element matrix.

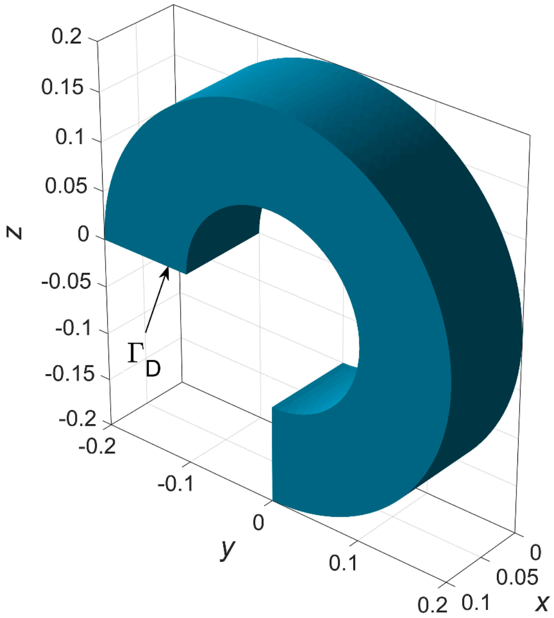

Fig. 27. The computational domain Ω, corresponding to a ring (with one fourth of it missing). The ring is ‘supported’ by the plane Γ_D, on which we impose homogeneous Dirichlet conditions. The ring will be deformed under the action of its own weight, caused by the gravity field acting throughout its bulk. Dimension units in meters (m).

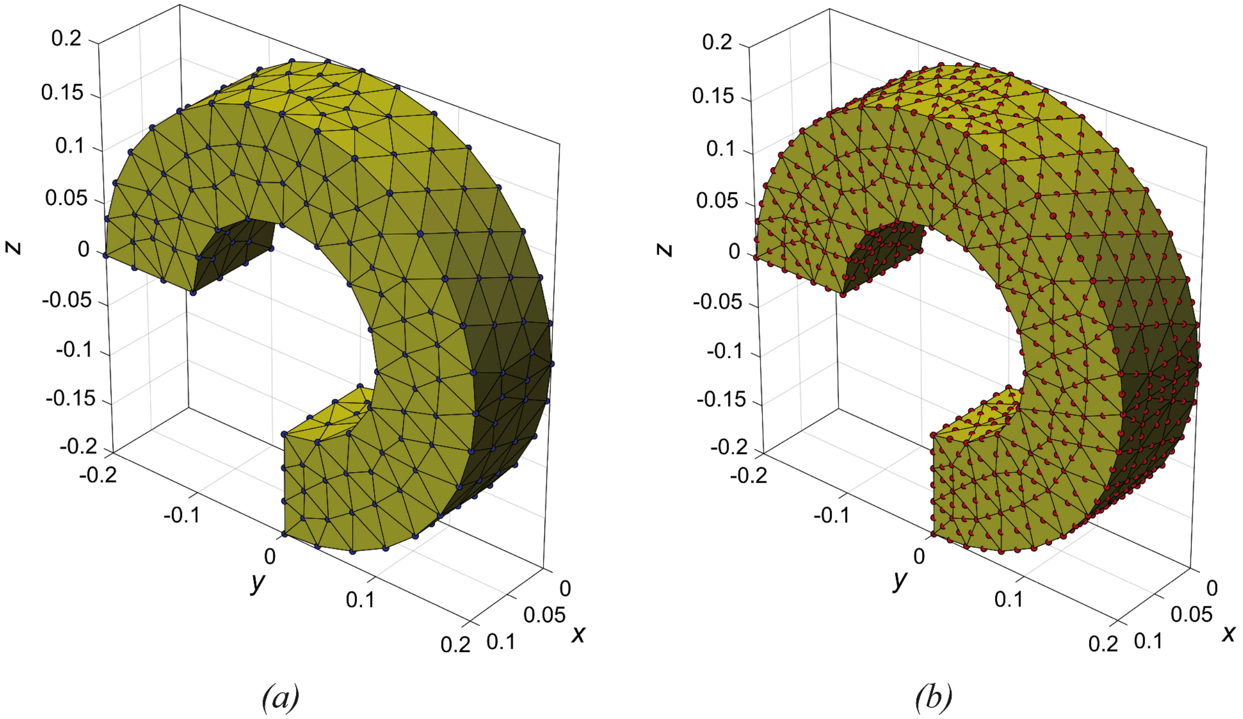

(a) *(b)*

Fig. 28. A coarse mesh of 1693 cells set up over the domain $\overline{\Omega}$. The nodes in *(a)* are used in the approximation of the displacement field $\mathbf{u}^h$ in the $\mathbf{OFE}_1$ space, whereas the nodes in *(b)* are used for approximations of $\mathbf{u}^h$ in the $\mathbf{P}_2$ space. There are many more nodes in *(b)* because extra nodes at the midpoints of the edges are necessary.

cross-sections lie on the *yz*-plane. The material properties of the ring are given by $E_Y = 1000$ kPa (Young's modulus) and $\rho = 800\ \mathrm{kg/m^3}$ (density), and the body (volumetric) forces are equal to the gravity field, i.e., $\mathbf{b} = [0, 0, -10]^T\ \mathrm{m/s^2}$. We assume homogeneous Dirichlet boundary conditions $\mathbf{u} = \mathbf{0}$ on the plane surface $\Gamma_D \subset \partial\Omega$ given by $0 < x < 0.1$, $-0.2 < y < -0.1$, and $z = 0$ (indicated by an arrow in Fig. 27), and homogeneous Neumann conditions (zero traction) $\mathbf{g} = \mathbf{0}$ on the remaining parts of the boundary $\partial\Omega$.

The goal is again to compare the precision of the $\mathbf{OFE}_1/\mathrm{OFE}_0$ and $\mathbf{P}_2/P_1$ solutions, *when the same mesh is used for both*. Fig. 28 shows a typical (coarse) mesh of tetrahedral cells set up over the domain $\overline{\Omega}$, with the nodes used in each case. We can thus have a visual indication that the $\mathbf{P}_2/P_1$ pair requires many more nodes than the $\mathbf{OFE}_1/\mathrm{OFE}_0$ pair. Indeed, for the particular mesh of 1693 cells shown in these figures, there are 454 nodes in Fig. 28*a* and 2891 nodes in Fig. 28*b*

Figs. 29*a* - 29*f* show the front and rear views of the undeformed and deformed solids, the latter calculated by the $\mathbf{OFE}_1/\mathrm{OFE}_0$ and $\mathbf{P}_2/P_1$ pairs on a mesh with 35,141 cells, see Fig. 30. Because in linear elasticity the displacements are very small (see Section 2.1), we use a scale factor of 100, i.e., the real displacement is 100 times smaller than what is shown in the figures. In Figs. 31*a* - 31*c*, we show the lateral view of the undeformed and deformed configurations of the body, in the *yz*-plane at $x = 0.1$ m. The deformation along the negative *z*-direction (the direction of the volumetric force $\mathbf{b}$) is now obvious. In Figs. 32*a* and 32*b*, we calculate the *z*-component of the displacement field u_3^h (or u_z^h) and the pressure p^h along the inner and outer arcs of the ring, i.e., from point A all the way to point B, and from point C all the way to point D in Fig. 31*a*, but considering $x = 0.05$ m (i.e., we slice the ring right in the middle, perpendicularly to its axis). Since these curves lie on the *yz*-plane, they can be parametrized by a polar angle ϕ, defined as $\phi := \tan^{-1}(z/y)$ with respect to

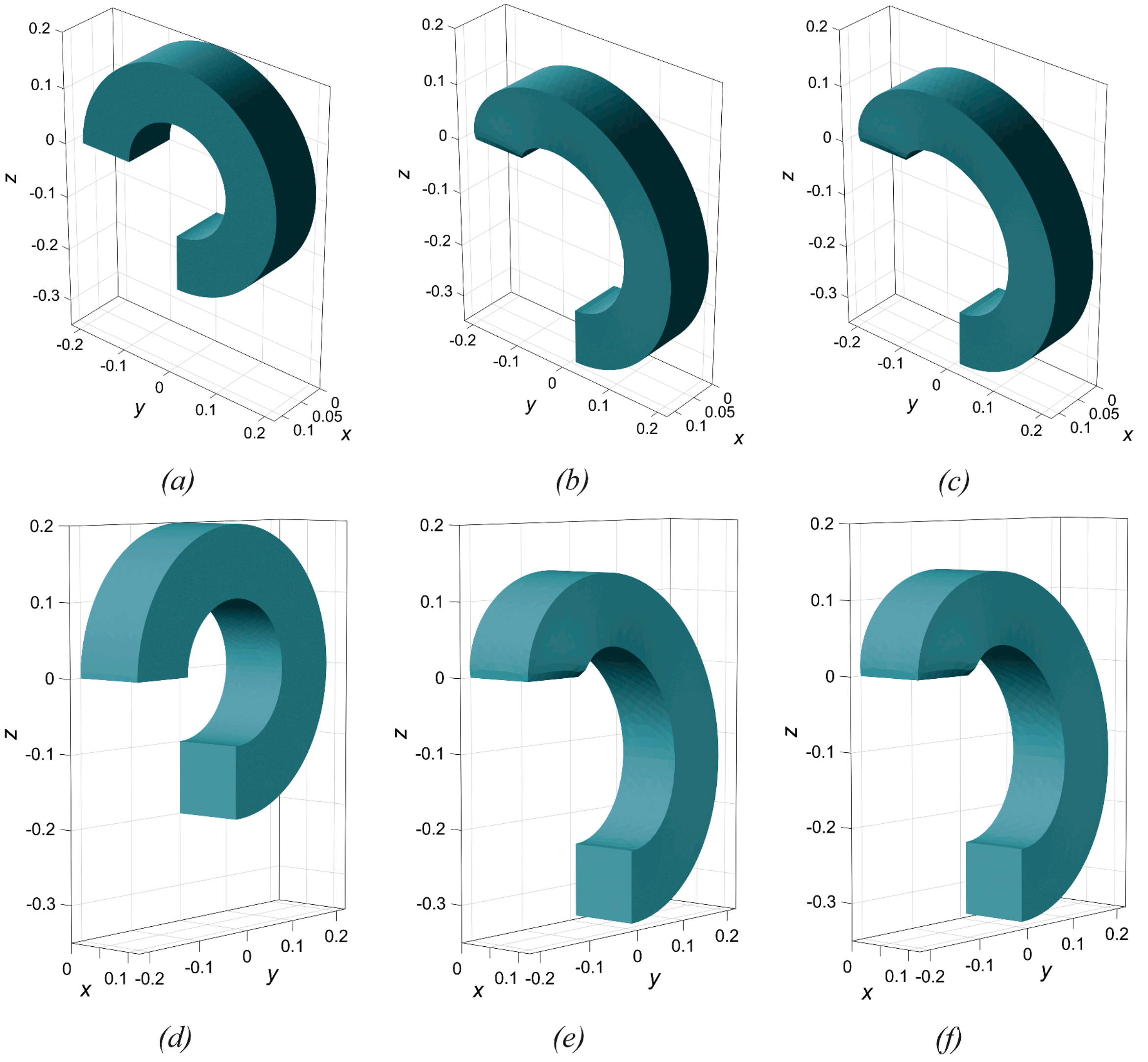

Fig. 29. Front view: *(a)* The undeformed body. *(b)* The deformed body, calculated by the $\mathbf{OFE}_1/\mathrm{OFE}_0$ pair. *(c)* The deformed body, calculated by the $\mathbf{P}_2/P_1$ pair. In *(b)* and *(c)*, we use a scale factor of 100. Rear view: *(d)* The undeformed body. *(e)* The deformed body, calculated by the $\mathbf{OFE}_1/\mathrm{OFE}_0$ pair. *(f)* The deformed body, calculated by the $\mathbf{P}_2/P_1$ pair. In *(e)* and *(f)*, we use a scale factor of 100. Dimension units in meters (m).

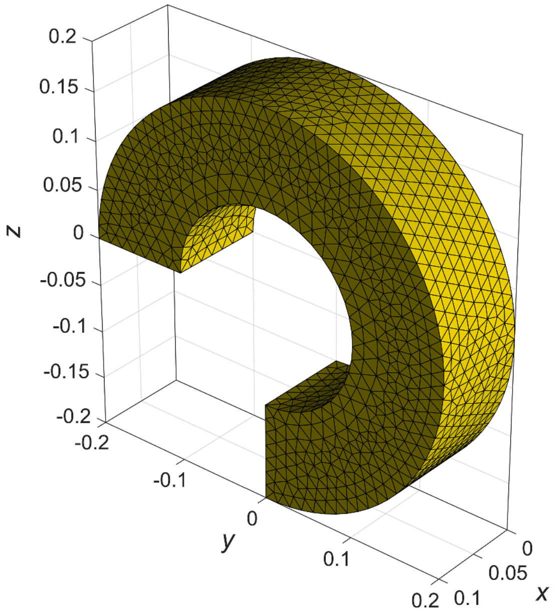

Fig. 30. The actual mesh of 35,141 tetrahedral cells used in the calculation of the displacements in Fig. 29.

the origin of the yz-plane, so that the coordinates of the curves are given by:

$$\begin{aligned} x_{\text{inner}}(\phi) &= 0.05, \\ y_{\text{inner}}(\phi) &= 0.1\cos\phi, \\ z_{\text{inner}}(\phi) &= 0.1\sin\phi, \end{aligned} \tag{7.1}$$

for the inner arc AB, and

$$\begin{aligned} x_{\text{outer}}(\phi) &= 0.05, \\ y_{\text{outer}}(\phi) &= 0.2\cos\phi, \\ z_{\text{outer}}(\phi) &= 0.2\sin\phi, \end{aligned} \tag{7.2}$$

for the outer arc CD, see Fig. 31*a*. The polar angle is such that $-90^\circ \leq \phi \leq 180^\circ$. For example, when $\phi = 180^\circ$, Eqs. (7.1) yield $y_{\text{inner}} = -0.1$ and $z_{\text{inner}} = 0$, which is just point A in Fig. 31*a*, and when $\phi = -90^\circ$, we get $y_{\text{inner}} = 0$ and $z_{\text{inner}} = -0.1$, which is

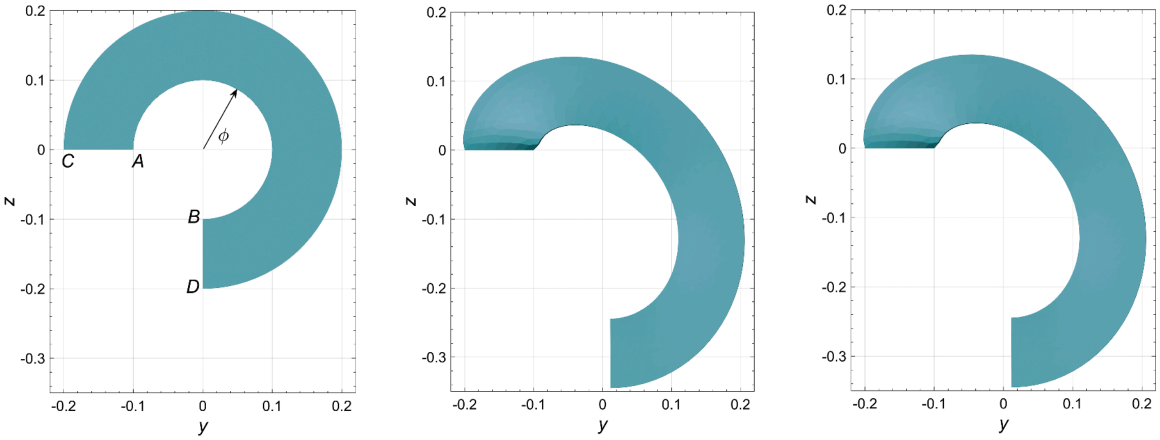

(a) *(b)* *(c)*

Fig. 31. Lateral view: *(a)* The undeformed body. *(b)* The deformed body, calculated by the $\mathbf{OFE}_1/\text{OFE}_0$ pair. *(c)* The deformed body, calculated by the $\mathbf{P}_2/P_1$ pair. In *(b)* and *(c)*, we use a scale factor of 100. Dimension units in meters (m).

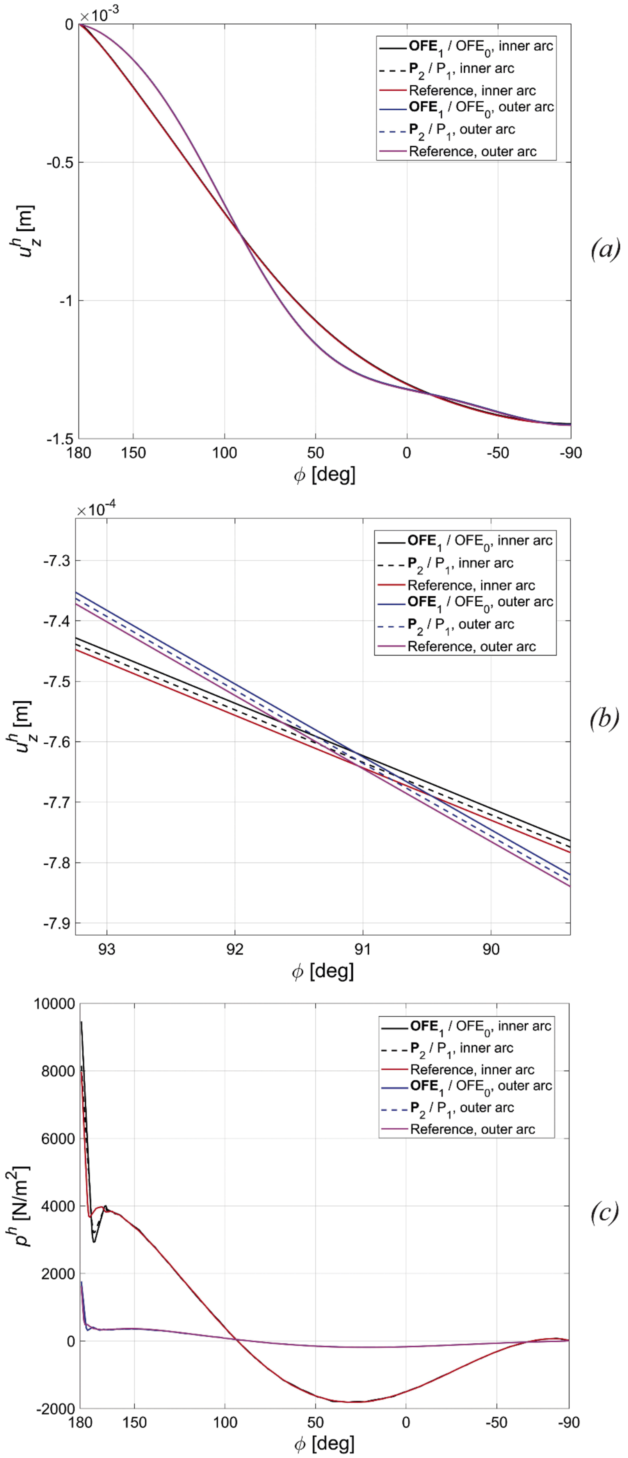

Fig. 32. *(a)* The z-component of the displacement field u_3^h calculated along the arcs *AB* (inner arc) and *CD* (outer arc) in Fig. 31*a*. *(b)* The fine structure of the displacement curves in *(a),* after magnifying the view around the angle $\phi = 91^\circ$. *(c)* The pressure p^h. In the calculation of these quantities, we used the $\mathbf{OFE}_1/\mathrm{OFE}_0$ and $\mathbf{P}_2/P_1$ pairs on the mesh with 35,141 cells from Fig. 30.

precisely point B in Fig. 31*a*. The outer arc can be described likewise.

The quantities u_3^h (or u_z^h) and p^h are calculated by the $\mathbf{OFE}_1/\mathrm{OFE}_0$ and $\mathbf{P}_2/P_1$ pairs on the mesh of 35,141 cells from Fig. 30. They are compared with a reference solution calculated by the $\mathbf{P}_2/P_1$ pair on a very refined mesh. (The reference solution uses a mesh with 150, 169 cells, leading to more than 650, 000 DoF's.) Again, we observe the same phenomenon: the curves for the displacement u_3^h in Fig. 32*a* are so on top of each other that they are indistinguishable to the naked eye: a zoom is necessary in order to reveal the fine structure of the curves, see Fig. 32*b*. The agreement between the pressure solutions is also evident: apart from a small discrepancy in the neighborhood of $\phi = 180^\circ$, the curves are also on top of each other, see Fig. 32*c*. Once more the $\mathbf{OFE}_1/\mathrm{OFE}_0$ and $\mathbf{P}_2/P_1$ pairs, when employed in the same mesh of Fig. 30, produced essentially the same solution, but the $\mathbf{OFE}_1/\mathrm{OFE}_0$ pair required 89,284 DoF's, whereas the $\mathbf{P}_2/P_1$ pair required 159,034 DoF's (i.e., more than one hundred and fifty thousand DoF's). Indeed, the ratio $89,284\ /159{,}034 \simeq 0.56$ approaches the theoretical limit of 0.52, see Section 4.4.1.

This example gives us a reasonable idea of the scalability properties of the $\mathbf{OFE}_1/\mathrm{OFE}_0$ pair, and how they can be put to good use when solving even larger three-dimensional incompressible problems. These results once more corroborate our conclusion that, at least in three-dimensional meshes with a large number of tetrahedral cells, it is advisable to use our $\mathbf{OFE}_1/\mathrm{OFE}_0$ element instead of the Taylor-Hood element $\mathbf{P}_2/P_1$, since both produce virtually identical results when used on the same mesh. However, the first requires far less DoF's than the latter.

8. Concluding remarks

In this work we explored the properties of a novel element conceived for three-dimensional analyses of incompressible linear elastic media. The element is based on the overlapping finite element paradigm, and uses different orders of approximation in the calculation of the displacement and pressure fields.

Among the positive features of our element, we notice that its basis functions are entirely polynomial, which leads to relatively few points required by the numerical integration of the weak forms. In addition to a fast numerical integration, the element also passes the inf-sup stability test, which rules out the possibility of spurious pressure solutions and of locking. The element also shows insensitivity to mesh distortions because the displacement solutions remain unchanged when the cells become distorted – which was the primary aim to achieve [4,5]. One of the remarkable properties of the new element is its ability to yield solutions with the same precision as the classical Taylor-Hood element, but using just a fraction of the DoF's. The resulting sparse matrices, in addition to being smaller, also have a tighter bandwidth, which can significantly alleviate the cost of solving the corresponding linear systems of equations arising from the discretization of very large problems [1,2].

In regard to future developments, we believe that the element presented in this work can also be used in other analyses where the incompressibility condition needs to be fulfilled such as in the solution of problems in three-dimensional fluid dynamics and magnetohydrodynamics [23], and also in the solution of electromagnetic problems characterized by a divergence-free condition on the fields [33].

CRediT authorship contribution statement

Williams L. Nicomedes: Writing – review & editing, Writing – original draft, Visualization, Validation, Software, Resources, Methodology, Investigation, Formal analysis, Conceptualization. **Klaus-Jürgen Bathe:** Writing – review & editing, Supervision, Methodology, Investigation, Formal analysis, Conceptualization.

Declaration of competing interest

The authors declare that they have no known competing financial interests or personal relationships that could have appeared to influence the work reported in this paper.

Appendix A

We show now that the space OFE_1 introduced in Section 3.5.1 is indeed a subspace of $H^1(\Omega)$. The answer is based on the following theorem [37]:

Theorem 1: Let v be a scalar function defined on the domain Ω. Then v belongs to $H^1(\Omega)$ if and only if:

1. $v|_{\Omega^e} \in H^1(\Omega^e)$ for each cell $e = 1, \cdots, E$ in the partition $\mathscr{T}_h$;
2. For each common face $F = \overline{\Omega}^m \cap \overline{\Omega}^n$ (the intersection between the closures of cells m and n), where $m, n = 1, \cdots, E$, the trace of $v|_{\Omega^m}$ and of $v|_{\Omega^n}$ on F is the same.

We must show that our u_i^h in (3.17) satisfies the two hypotheses of this theorem. (We recall that u_i^h is one of the three components of the displacement field, i.e., $i = 1,2,3$). So let e be an arbitrary cell in the partition $\mathscr{T}_h$, identified by its four nodes $K = 1, \cdots, 4$, see Fig. 3. According to (3.14), the modulating functions ρ_K are formed from a combination of 4-node hat functions (degree 1 polynomials in x, y, and z within Ω^e) together with products of hat functions and 10-node quadratic basis functions (these expressed as degree 2 polynomials). In the end, ρ_K can be expressed as a degree 3 polynomial (or as a degree 1 polynomial with a small perturbation of degree 3, see Section 3.5.1). Since $U_{K,(i)}$ in (3.18) is a full degree 1 polynomial, we conclude that each term $\rho_K U_{K,(i)}$ in (3.17) is a degree 4 polynomial in x, y, and z (or a degree 2 polynomial with a small perturbation of degree 4, see Section 3.5.1), and so is our component u_i^h calculated within Ω^e, or $u_i^h|_{\Omega^e}$. Since $u_i^h|_{\Omega^e}$ is a polynomial defined on Ω^e, it can be continuously extended to $\overline{\Omega}^e$ (a compact set), and so it follows that $u_i^h|_{\Omega^e}$ is square-integrable on Ω^e, i.e., it belongs to $L^2(\Omega^e)$. The derivatives (with respect to x, y, and z) of $u_i^h|_{\Omega^e}$ are again polynomials defined on Ω^e, and so belong to $L^2(\Omega^e)$ by the same reasoning. Therefore, we conclude that $u_i^h|_{\Omega^e} \in H^1(\Omega^e)$.

To verify hypothesis 2, we refer to Fig. A1*a*, which shows two arbitrary cells m and n in our partition $\mathscr{T}_h$. Cell m is identified by the four nodes 1, 2, 3, and 4, whereas cell n is identified by the four nodes 1, 3, 4, and 5. The cells are arranged in such a way that they share a common triangular face $F = \overline{\Omega}^m \cap \overline{\Omega}^n$, identified by the three vertices 1, 3, and 4. Within cell Ω^m, u_i^h is expanded as in (3.17), i.e.,

$$u_i^h|_{\Omega^m} = \sum_{K=1}^{4} \rho_K U_{K,(i)}, \tag{A.1}$$

where the modulating functions $\rho_1, \cdots, \rho_4$ are given by expressions as in (3.14). Indeed, using the 'mid-edge' virtual nodes $\overline{5}$, $\overline{6}$, $\cdots$, $\overline{10}$ in Fig. A1*b*, the modulating functions within cell Ω^m can be written as:

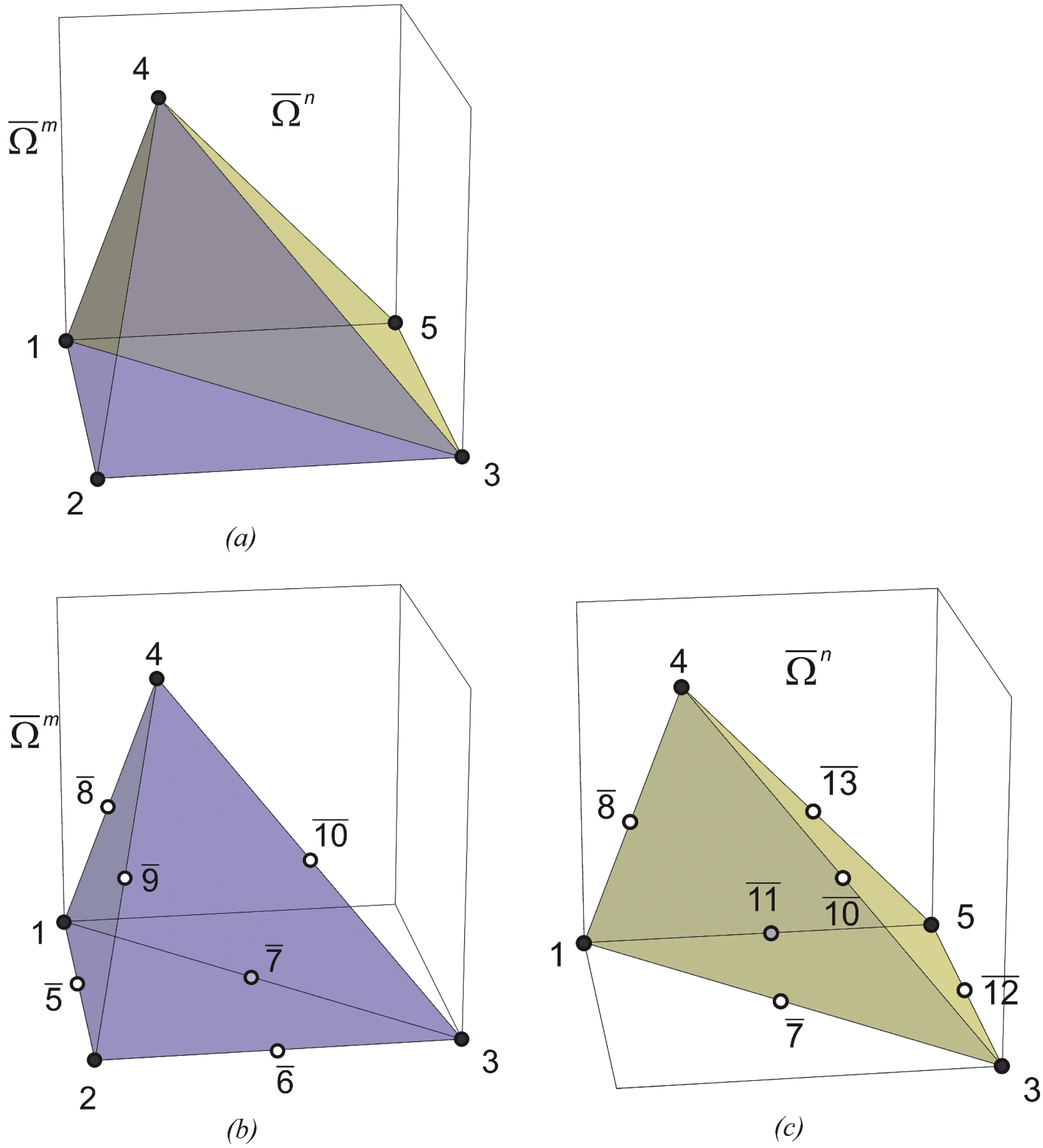

(a)

(b)

(c)

Fig. A1. *(a)* The cells $\overline{\Omega}^m$ and $\overline{\Omega}^n$, which share a common face F (the triangle spanned by the three nodes 1, 3, and 4). *(b)* Cell $\overline{\Omega}^m$ and its ten nodes. *(c)* Cell $\overline{\Omega}^n$ and its ten nodes. In *(b)* and *(c)*, the "virtual nodes" are written with an overbar. There are no DoF's ascribed to these nodes.

$$
\begin{aligned}
\rho_1 &= h_1 + \beta(h_2 - h_1)\widehat{h}_{\overline{5}} + \beta(h_3 - h_1)\widehat{h}_{\overline{7}} + \beta(h_4 - h_1)\widehat{h}_{\overline{8}},\\
\rho_2 &= h_2 + \beta(h_1 - h_2)\widehat{h}_{\overline{5}} + \beta(h_3 - h_2)\widehat{h}_{\overline{6}} + \beta(h_4 - h_2)\widehat{h}_{\overline{9}},\\
\rho_3 &= h_3 + \beta(h_2 - h_3)\widehat{h}_{\overline{6}} + \beta(h_1 - h_3)\widehat{h}_{\overline{7}} + \beta(h_4 - h_3)\widehat{h}_{\overline{10}},\\
\rho_4 &= h_4 + \beta(h_1 - h_4)\widehat{h}_{\overline{8}} + \beta(h_2 - h_4)\widehat{h}_{\overline{9}} + \beta(h_3 - h_4)\widehat{h}_{\overline{10}}.
\end{aligned}
\tag{A.2}
$$

On the other hand, we write the expansion within cell Ω^n using the vertices 1, 3, 4, and 5 in Fig. A1*c* as:

$$
u_i^h\big|_{\Omega^n} = \sum_{K\in\{1,3,4,5\}} \rho_K U_{K,(i)},
\tag{A.3}
$$

where the modulating functions now use the ‘mid-edge’ virtual nodes $\overline{7}, \overline{8}$, $\overline{10}$, $\overline{11}$, $\overline{12}$, and $\overline{13}$:

$$
\begin{aligned}
\rho_1 &= h_1 + \beta(h_3 - h_1)\widehat{h}_{\overline{7}} + \beta(h_4 - h_1)\widehat{h}_{\overline{8}} + \beta(h_5 - h_1)\widehat{h}_{\overline{11}},\\
\rho_3 &= h_3 + \beta(h_1 - h_3)\widehat{h}_{\overline{7}} + \beta(h_4 - h_3)\widehat{h}_{\overline{10}} + \beta(h_5 - h_3)\widehat{h}_{\overline{12}},\\
\rho_4 &= h_4 + \beta(h_1 - h_4)\widehat{h}_{\overline{8}} + \beta(h_3 - h_4)\widehat{h}_{\overline{10}} + \beta(h_5 - h_4)\widehat{h}_{\overline{13}},\\
\rho_5 &= h_5 + \beta(h_1 - h_5)\widehat{h}_{\overline{11}} + \beta(h_3 - h_5)\widehat{h}_{\overline{12}} + \beta(h_4 - h_5)\widehat{h}_{\overline{13}}.
\end{aligned}
\tag{A.4}
$$

Let $\mathbf{x}$ be an arbitrary point on the face F. It is clear from Fig. A1*b* that the functions h_2, $\widehat{h}_{\overline{5}}$, $\widehat{h}_{\overline{6}}$, and $\widehat{h}_{\overline{9}}$ are zero over the face F, and so the modulating functions in (A.2), when extended to the boundary of cell Ω^m become, when calculated at $\mathbf{x}$:

$$
\begin{aligned}
\rho_1 &= h_1 + \beta(h_3 - h_1)\widehat{h}_{\overline{7}} + \beta(h_4 - h_1)\widehat{h}_{\overline{8}},\\
\rho_2 &= 0,\\
\rho_3 &= h_3 + \beta(h_1 - h_3)\widehat{h}_{\overline{7}} + \beta(h_4 - h_3)\widehat{h}_{\overline{10}},\\
\rho_4 &= h_4 + \beta(h_1 - h_4)\widehat{h}_{\overline{8}} + \beta(h_3 - h_4)\widehat{h}_{\overline{10}},
\end{aligned}
\tag{A.5}
$$

i.e., the modulating function corresponding to the vertex opposite to face F is equal to zero, or $\rho_2 = 0$. Moreover, the remaining modulating functions ρ_1, ρ_3, and ρ_4 depend only on the nodes that lie on face F, i.e., on h_1, h_3, h_4 and $\widehat{h}_{\overline{7}}$, $\widehat{h}_{\overline{8}}$, $\widehat{h}_{\overline{10}}$.

Figure A1*c* shows that the functions h_5, $\widehat{h}_{\overline{11}}$, $\widehat{h}_{\overline{12}}$, and $\widehat{h}_{\overline{13}}$ are zero over the face F, and so the modulating functions in (A.4), when extended to the boundary of cell Ω^n become, when calculated at $\mathbf{x}$:

$$
\begin{aligned}
\rho_1 &= h_1 + \beta(h_3 - h_1)\widehat{h}_{\overline{7}} + \beta(h_4 - h_1)\widehat{h}_{\overline{8}},\\
\rho_3 &= h_3 + \beta(h_1 - h_3)\widehat{h}_{\overline{7}} + \beta(h_4 - h_3)\widehat{h}_{\overline{10}},\\
\rho_4 &= h_4 + \beta(h_1 - h_4)\widehat{h}_{\overline{8}} + \beta(h_3 - h_4)\widehat{h}_{\overline{10}},\\
\rho_5 &= 0.
\end{aligned}
\tag{A.6}
$$

We observe the same pattern again: the modulating function corresponding to the vertex opposite to face F is equal to zero, or $\rho_5 = 0$, and the remaining modulating functions ρ_1, ρ_3, and ρ_4 depend only on the nodes that lie on face F, i.e., on h_1, h_3, h_4 and $\widehat{h}_{\overline{7}}$, $\widehat{h}_{\overline{8}}$, $\widehat{h}_{\overline{10}}$.

When we use (A.5) on (A.1) and (A.6) on (A.3), we discover that $u_i^h|_{\Omega^m}$ and $u_i^h|_{\Omega^n}$ have the same value when evaluated at our point $\mathbf{x}$. Since $\mathbf{x}$ is arbitrary, we conclude that the traces of these functions are equal to each other on the face F.

Data availability

Data will be made available on request.

References

[1] K.J. Bathe, Finite Element Procedures, Prentice Hall, 1996.
[2] K.J. Bathe, Finite Element Procedures, 2nd ed., Amazon.com, 2014; and Higher Education Press, China, 2016.
[3] K.J. Bathe, The inf-sup condition and its evaluation for mixed finite element methods”, Comp. Struct. 79 (2001) 243–252.
[4] K.J. Bathe, The finite element method with ‘overlapping finite elements, in: Proceedings of the Sixth International Conference on Structural Engineering, Mechanics and Computation – SEMC 2016, Cape Town, South Africa, 2016 (A. Zingoni, ed.).
[5] K.J. Bathe, The AMORE paradigm for finite element analysis, Adv. Eng. Softw. 130 (2019) 1–13.
[6] K.J. Bathe, Finite Element Procedures – En Plus, Springer Nature, 2025 in press.
[7] K.J. Bathe, L. Zhang, The finite element method with overlapping elements – A new paradigm for CAD driven simulations, Comp. Struct. 182 (2017) 526–539.
[8] F. Brezzi, M. Fortin, Mixed and Hybrid Finite Elements. Springer Series in Computational Mathematics, Springer, 1991.

[9] Y. Chai, K.J. Bathe, Transient wave propagation in inhomogeneous media with enriched overlapping triangular elements, Comp. Struct. 237 (2020) 106273.
[10] D. Chapelle, K.J. Bathe, The inf-sup test, Comp. Struct. 47 (1993) 537–545.
[11] P. Ciarlet, Linear and Nonlinear Functional Analysis with Applications, Soc. Indust. Appl. Math. (SIAM) (2013).
[12] G.R. Cowper, Gaussian quadrature formulas for triangles, Int. J. Numer. Methods Eng. 7 (1973) 405–408.
[13] S. De, K.J. Bathe, The Method of Finite Spheres, Comput. Mech. 25 (2000) 329–345.
[14] S. De, K.J. Bathe, The method of finite spheres with improved numerical integration, Comp. Struct. 79 (2001) 2183–2196, a.
[15] S. De, K.J. Bathe, Displacement/pressure mixed interpolation in the method of finite spheres, Int. J. Numer. Methods Eng. 51 (2001) 275–292, b.
[16] A. Ern and J. L. Guermond, Finite elements II – Galerkin approximation, elliptic and mixed PDEs, Springer Texts in Applied Mathematics, Springer, 2021.
[17] S. Ham, B. Lai, K.J. Bathe, The method of finite spheres for wave propagation problems, Comp. Struct. 142 (2014) 1–14.
[18] J. Huang, K.J. Bathe, Quadrilateral overlapping elements and their use in the AMORE paradigm, Comp. Struct. 222 (2019) 25–35.
[19] J. Huang, K.J. Bathe, Overlapping finite element meshes in AMORE, Adv. Eng. Softw. 144 (2020) 102791.
[20] J. Huang, K.J. Bathe, On the convergence of overlapping elements and overlapping meshes, Comp. Struct. 244 (2021) 106429.
[21] T.J.R. Hughes, The Finite Element Method: Linear Static and Dynamic Finite Element Analysis, Dover Publications, 2000.
[22] F. Irgens, Continuum Mechanics, Springer, 2008.
[23] D. Jin, P.D. Ledger, A.J. Gil, hp-Finite element solution of coupled stationary magnetohydrodynamics problems including magnetostrictive effects, Comp. Struct. 164 (2016) 161–180.
[24] Y. Jinyun, Symmetric Gaussian quadrature formulae for tetrahedronal regions, Comput. Methods Appl. Mech. Eng. 43 (1984) 349–353.
[25] K.T. Kim, K.J. Bathe, Transient implicit wave propagation dynamics with the method of finite spheres, Comp. Struct. 173 (2016) 50–60.
[26] K.T. Kim, L. Zhang, K.J. Bathe, Transient implicit wave propagation dynamics with overlapping finite elements, Comp. Struct. 199 (2018) 18–33.
[27] Y. Ko, P.S. Lee, K.J. Bathe, A new 4-node MITC element for analysis of two-dimensional solids and its formulation in a shell element, Comp. Struct. 192 (2017) 34–49.
[28] W.M. Lai, D. Rubin, E. Krempl, Introduction to Continuum Mechanics, 4th Edition, Butterworth-Heinemann (Elsevier), 2010.
[29] B. Lai, K.J. Bathe, The method of finite spheres in three-dimensional linear static analysis, Comp. Struct. 173 (2016) 161–173.
[30] S. Lee, K.J. Bathe, An enhancement of overlapping finite elements, Comp. Struct. 260 (2022) 106704 a.
[31] S. Lee, K.J. Bathe, Additional overlapping finite elements – The pyramid and prism elements, Comp. Struct. 268 (2022) 106813 b.
[32] S. Lee, K.J. Bathe, Solution of the generalized eigenvalue problem using overlapping finite elements, Adv. Eng. Softw. 173 (2022) 103241 c.
[33] W.L. Nicomedes, K.J. Bathe, F.J.S. Moreira, R.C. Mesquita, Meshfree analysis of electromagnetic wave scattering from conducting targets: Formulation and computations, Comp. Struct. 184 (2017) 36–52.
[34] W.L. Nicomedes, K.J. Bathe, F.J.S. Moreira, R.C. Mesquita, The method of finite spheres in acoustic wave propagation through nonhomogeneous media: inf-sup stability conditions, Vietnam J. Mech. 42 (2020) 209–237. VAST.
[35] W.L. Nicomedes, K.J. Bathe, F.J.S. Moreira, R.C. Mesquita, Acoustic scattering in nonhomogeneous media and the problem of discontinuous gradients: Analysis and inf-sup stability in the method of finite spheres, Int. J. Numer. Methods Eng. 122 (2021) 3141–3170.
[36] W.L. Nicomedes, K.J. Bathe, F.J.S. Moreira, R.C. Mesquita, Overlapping finite elements for the Navier-Stokes equations, Comp. Struct. 299 (2024) 107343.
[37] A. Quarteroni, A. Valli, Numerical approximation of partial differential equations. Springer Series in Computational Mathematics, Springer, 2008.
[38] B. Sauren, S. Klarmann, L. Kobbelt, S. Klinkel, A mixed polygonal finite element formulation for nearly-incompressible finite elasticity, Comput. Methods Appl. Mech. Eng. 403 (2023) 115656.
[39] P. Wriggers, M.L. De Bellis, B. Hudobivnik, A Taylor-Hood type virtual element formulations for large incompressible strains, Comput. Methods Appl. Mech. Eng. 385 (2021) 114021.
[40] L. Zhang, K.J. Bathe, Overlapping finite elements for a new paradigm of solution, Comp. Struct. 187 (2017) 64–76.
[41] L. Zhang, K.T. Kim, K.J. Bathe, The new paradigm of finite element solutions with overlapping elements in CAD – Computational efficiency of the procedure, Comp. Struct. 199 (2018) 1–17.